Broadband Thin Film Absorber Based on Plasmonic Nanoparticles

Zur Erlangung des akademischen Grades eines
DOKTORS DER NATURWISSENSCHAFTEN
(Dr. rer. nat)

von der KIT-Fakultät für Physik
des Karlsruher Instituts für Technologie (KIT)

angenommene Dissertation

von

M.Sc. Nanda Perdana

am Institut für Theoretische Festkörperphysik

Tag der mündlichen Prüfung:	01.12.2023
Referent:	Prof. Dr. Carsten Rockstuhl
Korreferent:	Prof. Dr. Franz Faupel

Thesis Abstract

Harvesting solar energy presents a formidable challenge, primarily rooted in the need to efficiently capture light across a broad spectrum range. Addressing this challenge, we describe the concept of designing a broadband perfect absorber in the form of a thin-film system with plasmonic nanoparticles as its foundational basis. To understand how the light can be absorbed by the absorber and how to optimize the absorber, we begin by looking into the fundamentals of electromagnetic wave scattering inside matter and a dedicated multiscale modeling technique, which is the computational methodology employed throughout this thesis. This multiscale modeling technique allows us to bridge the optical responses from photonic structures with critical features at multiple length scales.

Continuing to the next chapter, we study a thin-film absorber made from the scattering responses of an Au_{144} gold molecules. Here, in the purpose to outline details of the multiscale modeling process in depth, we determine the optical properties of the individual gold molecule by using time-dependent density functional theory. It turns out that, this kind of thin-film absorber absorbs the light in the entire visible light region quite well. As a further aspect, we employ bulk copper nanoparticles as the basis for the nanoparticle layer within the absorber. We inspect on computational grounds the effect of the nanoparticles filling factor and the thin-film thicknesses on the absorber performance.

Remarkably, our findings reveal that the thin-film absorber with copper nanoparticles is capable of absorbing 90% of light energy across a broad spectrum ranging from ultraviolet to near-infrared wavelengths. To validate the accuracy of our simulations, we translate these optimized absorber layouts into fabrications together with experimental partners from the University of Kiel. The experimental results align remarkably closely with our simulations, confirming the capability of our designed broadband perfect absorber. This research not only contributes to advancing solar harvesting technology but also underscores the potential of multiscale modeling techniques in tackling complex challenges at the intersection of materials science and renewable energy.

Contents

List of Figures

List of Tables

Publications List

P.1 M. M. Müller, N. Perdana, C. Rockstuhl, and C. Holzer, *The Journal of Chemical Physics* **156**, (2022).

P.2 N. Perdana, C. Holzer, and C. Rockstuhl, *ACS Omega* **7**, 19337 (2022).

P.3 N. Perdana, J. Drewes, F. Pohl, A. Vahl, T. Strunskus, M. Elbahri, C. Rockstuhl, and F. Faupel, *Micro and Nano Engineering* **16**, 100154 (2022).

P.4 J. Drewes, N. Perdana, K. Rogall, T. Hartig, M. Elis, U. Schürmann, F. Pohl, M. Abdelaziz, T. Strunskus, L. Kienle, M. Elbahri, F. Faupel, C. Rockstuhl, and A. Vahl, *Particle and Particle System Characteristics*, 2300102 (2023).

Conference Contributions

1. Nanda Perdana, Christof Holzer, and Carsten Rockstuhl, "Multi-scale Optical Modelling of Broadband Perfect Absorbers Based on Gold Clusters", *13th International Symposium on Modern Optics and Its Applications*, (online, August 2021)
2. Nanda Perdana, Kevin Rogall, Jonas Drewes, Alexander Vahl, Thomas Strunskus, Moheb Abdelaziz, Franz Faupel, and Carsten Rockstuhl, "Broadband perfect absorbers based on copper nanoparticles thin films", *CLEO/Europe-EQEC 2023*, (München, June 2023)
3. Nanda Perdana, Kevin Rogall, Jonas Drewes, Alexander Vahl, Thomas Strunskus, Moheb Abdelaziz, Franz Faupel, and Carsten Rockstuhl, "Broadband perfect absorbers based on copper nanoparticles thin films", *14th International Symposium on Modern Optics and Its Applications*, (Jakarta, August 2023)

1. Introduction

Light is everywhere. Each day, we bask in the sunlight as we step outside during the day, and when night falls, artificial lighting illuminates our surroundings, facilitating our activities. Thinking deeper, light is a fascinating phenomenon that captivates our understanding and imagination. Its dual nature as both a wave and a particle challenges the very foundations of physics, as demonstrated by the famous double-slit experiment [1]. From the eye-catching colors of a rainbow after rain to the laser display in a show, the ability to paint the world with vibrant hues and reveal hidden truths through spectroscopy is truly attractive to people. Furthermore, its incredible speed traveling at almost three hundred million meters per second, to be exact 299.792.458 meters per second in a vacuum, makes it the universal speed limit, defying our intuition. Light also plays a crucial role in our daily lives, from the warmth of sunlight to the marvels of optical communication [2, 3] and medical imaging technologies [4, 5]. The light strange, yet interesting behavior continues to inspire scientists that there are a lot of things yet to be discovered.

Interestingly, delving deeper into the study of light involves the exciting realm of optical metamaterials [6, 7, 8, 9]. Optical metamaterials are synthetic materials designed for controlling light at the nanoscale, spanning the spectrum from ultraviolet to visible light and even into the infrared range. What sets optical metamaterials apart is their ability to harness properties absent in the natural world. For instance, the concept of epsilon-near-zero materials, characterized by their permittivity hovering close to zero [10], and time-varying materials, where their optical properties change with time [11, 12, 13]. To unlock these exotic attributes, metamaterials are often structured on a sub-wavelength scale, ensuring that these exotic properties can be induced and harnessed for the benefit of science and technology alike.

One interesting topic to study is the light propagation and scattering in metamaterials. It is a phenomenon that unveils how electromagnetic waves interact with the meta-atoms within the metamaterial. When light enters a medium, such as air, water, or glass, the light interacts with the meta-atoms and is subject to a process called scattering. This scattering phenomenon is responsible for the refraction and diffraction of lights in various directions, giving rise to the beautiful phenomena we observe in our everyday lives, such as the blue sky, colorful sunsets, rainbows, and the beautiful underwater world. Different mediums and particles scatter light in distinctive ways, leading to unique optical responses. For instance, the shorter wavelengths of blue and violet light scatter more than longer wavelengths like red and orange, causing the sky to appear blue during the day, explained through Rayleigh scattering, when the sunlight interacts with particles or structures that are much smaller in size than the wavelength of the sunlight, the air molecules in the atmosphere, in this case, [14]. We can understand these aforementioned phenomena by exploring Maxwell's equations, which serve as the fundamental framework for understanding the behavior of electromagnetic waves. To unravel the complex interaction between light and matter, we must carefully solve these equations to unveil the patterns of electric and magnetic fields that emerge as a response to the presence of light. The Maxwell equations can be solved through analytical and computational means, which is further explained in this thesis.

We employ a powerful approach that categorizes itself as multiscale modeling technique. This technique serves as a bridge between various length scales, allowing us to seamlessly transition from the nanoscale to the macroscale. By acquiring the scattering response from small-sized particles, we can explore the scattering responses from larger objects and systems. An illustrative example of this methodology is the investigation of optical properties in cavities and metasurfaces constructed from chiral molecules [15, 16]. These studies are made feasible through the application of time-dependent density functional theory (TD-DFT), which enables us to capture the scattering responses at the molecular level. For instance, we can quantify how strong plasmonic excitations are sustained in hollow spherical gold nanoparticles [17]. Leveraging the insights gained through TD-DFT, we can then apply the multiscale modeling technique to real-world devices, thereby expanding our ability to manipulate and engineer optical properties across a range of scales.

Further to the application of the multiscale modeling technique, we want to take a look at the current state of the world regarding the energy crisis. The emergence of sustainable energy marks a significant shift in humanity's approach to powering our world. Historically dependent on finite fossil fuels, which have detrimental environmental impacts including air pollution and contribution to global warming, society began to recognize the need for more environmentally-friendly energy sources. Sustainable energy, deriving power from renewable resources such as wind, solar, hydro, and geothermal, promises not only a reduced carbon footprint but also a solution to the depletion of traditional fuels [18]. As the realities of climate change became more and more evident, and as technological advancements made renewable energy sources more viable and cost-effective, a global push towards sustainability began. A particularly intriguing topic in the realm of sustainable energy is the solar thermal collector (STC) [19, 20]. An STC is a device that collects solar radiation and converts it directly into heat. This collected energy is versatile and can be directed towards a multitude of heating applications, spanning from water [21] and space heating [22] to various industrial processes [23]. Moreover, using principles akin to turbines in large-scale geothermal plants, this captured heat can also be transformed into electricity [24]. This multi-functionality showcases the STC's capability to generate multiple forms of energy using a single device. There is a rich diversity within STCs, with various types including conventional black chrome absorbers [25], STCs that uses mixture of materials [26, 27, 28], grating STCs [29, 30], a photonic crystal STC [31], and those that incorporate nanoparticles [32, 33]. So that, this motivates us to focus on studying nanoparticle-based STCs combined with a multilayer system that acts as perfect broadband absorbers.

1.1 Thesis outline

In this thesis, our primary objective is to explore the potential of metallic nanoparticles as the foundation for a multilayer thin film system designed to function as a perfect broadband absorber. To start this thesis, it is important to know the fundamentals of the theories and computational methods that will be used to study the absorber. That's why we have focused Chapter 2 on explaining the basic ideas that will support our study.

Our study commences with a brief introduction to a nanoparticle packing algorithm known as the force-biased algorithm. This algorithm is helpful in densely arranging a cluster of spherical nanoparticles within a cubic unit cell. This specific arrangement of nanoparticles allows us to investigate the optical interactions that occur when numerous spherical nanoparticles are positioned nearby. To delve further into the optical phenomena, we delve into the heart of electromagnetic theory, the Maxwell equations, and the methods used to solve them. Among these methods, we examine the Mie theory, which permits us to expand both incident and scattered fields as linear combinations of vector spherical wave function with its appropriately determined Mie incident and scattered expansion coefficients.

Since we want to understand the electromagnetic wave in matter, especially in metals. We have to continue by explaining the optical properties of the metals. We start by elaborating Drude model. This model provides a basic understanding of electric permittivity in metals. Then we enhance the Drude permittivity by incorporating a size effect term, particularly when dealing with small-sized nanoparticles. After that, we consider that the metal is illuminated with electromagnetic waves with specific frequency so that a strong electric field outside near the surface of the metal is induced. This is caused by localized surface plasmon resonance. Later, we want to understand when two different spheres in plasmon resonance interact with each other. This will be explained through plasmon hybridization theory. This is important to our analysis of why a cluster of nanoparticles can trap the light, which is following our goal to design an absorber based on these nanoparticles.

The computational methods used in this thesis can be summarized under the notion of multiscale modeling techniques, a way to bridge the light scattering effects at the microscopic scale to a full-fledged macroscopic device. To shed light on the method, consider an isolated metallic nanoparticle. By studying its scattering response, one can analyze further and determine the optical characteristics of a macroscopic device made from a dense collection of such nanoparticles. After considering the isolated metallic nanoparticle, nanoparticles are systematically packed within a cubical unit cell, forming a dense cluster through the application of the force-biased algorithm. Therefore, in the following that is explained first, the T-matrix method steps in, determining the scattering response from the cluster. Progressing further, we can create a layer where these nanoparticle clusters are replicated periodically and infinitely extended in two dimensions, allowing for the determination of reflection and transmission coefficients from these slabs containing the metallic nanoparticles. For enabling the absorption optimization of the thin film, the s-parameter retrieval method is used to link effective material parameters such as permittivity to the film. The technique ends with determining the reflection and transmission coefficients from a stack of thin films by using the transfer-matrix method efficiently. Figure 1.1 points out the overall concept of the multiscale modeling method.

After we elaborate the theoretical background, we continue on Chapter 3, in which explains the application to the nanoparticles-based thin film broadband absorber. We explain the physics about how the combination between thin film system and

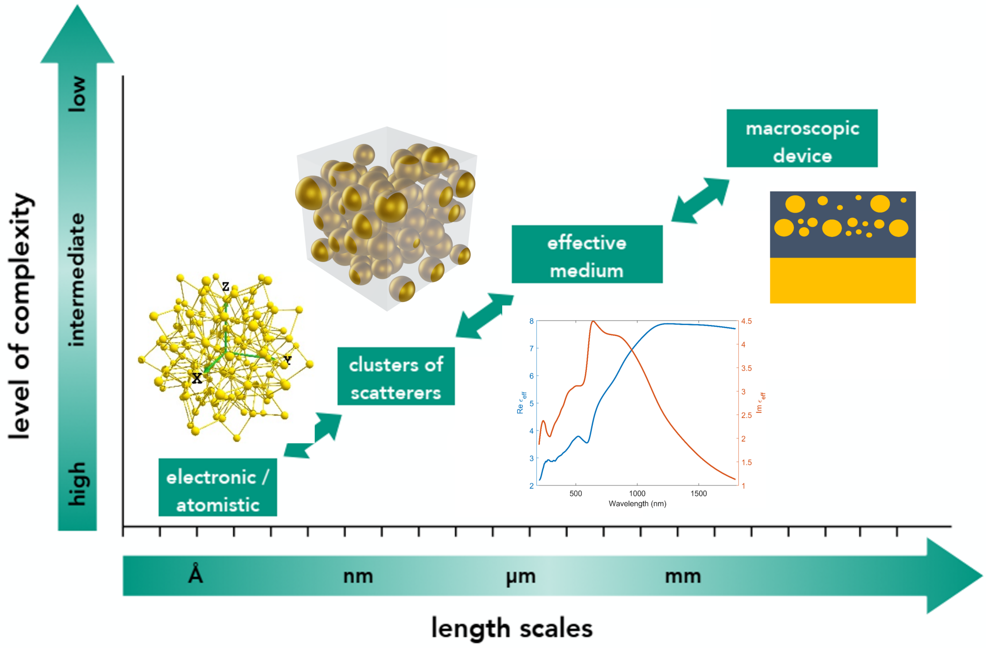

Figure 1.1: An illustration explaining multiscale modeling method.

a cluster of metallic nanoparticles can enhance light absorption, corresponding to optical properties of metal theories in Chapter 2. Then, we continue the thesis by considering two types of plasmonic nanoparticles that can be applied to a layer in the thin-film system: Au_{144} gold molecules and bulk copper nanoparticles.

We conclude the thesis by summarizing our discussion and offering a brief outlook on the possibility of further improving the thin-film absorber.

2. Theoretical Background

We start this chapter by explaining some of the theory and computational methods that are used in this thesis. The chapter is divided into two sections. The first section explains about the optical properties of metal and particle plasmon in general. We will use these theories as a basis to explain the physical response that arises around this thesis. The second section refers to the computational method that is used in this thesis in form of multiscale modeling technique.

2.1 Force-biased algorithm for tight-packing of spheres

People try to model real-life problems with computational effort, such as bin-packing problems [34]. In this problem, fixed number of bulk objects are filled in inside a bin, but they have to be placed in some way to have the best quantity as possible without overfilling and manipulating the capacity of the bin. Therefore, many packing algorithms are studied to solve the bin-packing problems. Packing algorithms are composed to generate the best configuration of a number of objects within a defined space, considering their unique shapes and sizes. Most of these algorithms force the objects to not overlapped and touching to each other. This is important for processes where the spatial organization of objects or particles directly impacts material properties. For instance, maximizing the density of nanoparticles in a drug delivery system can influence the therapeutic index, or achieving uniform distribution on a photovoltaic device can enhance light absorption efficiency.

One of such algorithms is the force-biased algorithm [35, 36]. Instead of using purely geometrical constraints, the algorithm incorporates the concept of simulated forces to optimize the packing configuration by maximizing the density of nanoparticles as possible in a fixed packing region. For now on, we will call the density of nanoparticles as filling fraction (FF). In a force-biased algorithm, particles or objects exert repulsive forces on each other when they overlap and attractive forces when they are close to a desired configuration. By following the gradient of these forces, particles can move to a configuration where the overall system's potential energy is minimized. This happens in an iterative process.

Consider N distributed spheres with diameter d_i in a container of volume V_{con}. In this thesis, the container is specified as a cube with a given side length. The spheres are modeled with a core-shell structure, the core is defined as the inner sphere and the core-shell-system as the outer sphere. The outer spheres have outer diameter $d_i^{\text{out}} = d_i d^{\text{out}}$ and the inner spheres have inner diameter $d_i^{\text{in}} = d_i d^{\text{in}}$. The inner diameter factor d^{in} dictates the diameter of the actual sphere of the system. The d_{out} is determined as an input parameter defined at the start of the calculation to be as large as possible by the user. Also, the centers of the spheres, $\mathbf{r}_i$, are randomized at the first calculation, so it has a very high chance that the spheres will overlap in this case.

At each iteration, when there is a pair of overlapping spheres i and j, there are two procedures in the algorithm:

- The spheres are repelled and changing positions to make sure that overlapping spheres are pushed away from each other. The positions are updated in each iteration according to the repulsion force $\mathbf{F}_{ij}$

  $$\mathbf{r}_i \to \mathbf{r}_i + \frac{1}{2d_i} \sum_{j \neq i} \mathbf{F}_{ij}, \tag{2.1}$$

  where the repulsion force is

  $$\mathbf{F}_{ij} = \sigma \Lambda_{ij} P_{ij} \frac{\mathbf{r}_j - \mathbf{r}_i}{||\mathbf{r}_j - \mathbf{r}_i||}. \tag{2.2}$$

  σ is the scaling factor. Λ_{ij} is 1 when the sphere $[i, j]$ overlap and 0 otherwise. P_{ij} is the potential function defined as

  $$P_{ij} = d_i^{\text{out}} d_j^{\text{out}} \left[\frac{||\mathbf{r}_j - \mathbf{r}_i||}{\frac{1}{4}\left(d_i^{\text{out}} + d_j^{\text{out}}\right)^2} - 1 \right]. \tag{2.3}$$

- The spheres are gradually shrinking by reducing d^{out} by utilizing Eq. (2.4),

  $$d^{\text{out}} \to d^{\text{out}} - \left(\frac{1}{2}\right)^{\delta} \frac{d_{\text{st}}^{\text{out}}}{4\tau}, \tag{2.4}$$

  where

  $$\delta = \log \left(\frac{\frac{\pi}{6} \sum_{i=1}^{N} \left(d_{i,\text{st}}^{\text{out}}\right)^3}{V_{\text{con}}} - \frac{\frac{\pi}{6} \sum_{i=1}^{N} \left(d_i^{\text{out}}\right)^3}{V_{\text{con}}} \right),$$

  τ is the contraction rate, and $d_{\text{st}}^{\text{out}}$ is d_{out} that is defined at the start of the iteration.

As iteration runs, the d^{out} would decrease so that d^{out} would be in an optimal value in which the spheres have a very close gap within each other. When the iteration converge, the final outer spheres will have a smaller or equal diameter than the inner spheres, due to the shrinking procedure, which means $d^{\text{in}} > \mathrm{d}^{\text{out}}$, the spheres are not overlapped and touching. The calculation can be stopped at the middle of the iteration for granting smaller filling fraction. The final filling fraction can be calculated by defining the ratio between the final volume of the inner spheres and the volume of the container χ stated in Eq. (2.5),

$$FF = \frac{\text{volume of the inner spheres}}{\text{volume of the container}} = \frac{\frac{\pi}{6} \sum_{i=1}^{N} \left(d_i^{\text{in}}\right)^3}{V_{\text{con}}} = \frac{\frac{\pi}{6} d^{\text{in}} \sum_{i=1}^{N} \left(d_i\right)^3}{V_{\text{con}}}. \tag{2.5}$$

In the next step, we continue from the hard-sphere packing algorithm and would like to describe how light will interact with these spheres. Fundamentally, the

Maxwell equations describe the electromagnetic response completely. Then, we will proceed to the T-matrix formulation to identify the scattering response it causes.

2.2 Maxwell equations

Given that a particle positioned within a background media. The particle can interact with another particle and the electromagnetic sources, like electromagnetic waves and electric currents. We can study the behavior of electromagnetic waves inside the particle in such a situation by solving Maxwell equations. The Maxwell equations are a set of equations spanning from Eq. (2.6) to Eq. (2.9) [37]. Not only do these equations shed light on the dynamics between arbitrarily shaped particles and electromagnetic waves, but they also account for the presence of total charge density ρ and total electric current density $\mathbf{J}$, respectively. The total charges inside the material include free charge and bound charge. Beyond that, these equations are fundamental in the broader realm of electromagnetism. They underpin our understanding of several related topics, such as the propagation of electromagnetic waves in different media, the principles governing electronic circuits, and the intricate behaviors of charges and currents when immersed in electromagnetic fields. As we progress, harnessing the insights from these equations will be instrumental in predicting and analyzing the responses of the nanospheres when exposed to electromagnetic waves. The four Maxwell's equations are:

$$\nabla \cdot \mathbf{D}(\mathbf{r}, t) = \rho_f(\mathbf{r}, t), \tag{2.6}$$

$$\nabla \cdot \mathbf{B}(\mathbf{r}, t) = 0, \tag{2.7}$$

$$\nabla \times \mathbf{E}(\mathbf{r}, t) = -\frac{\partial \mathbf{B}(\mathbf{r}, t)}{\partial t}, \tag{2.8}$$

$$\nabla \times \mathbf{H}(\mathbf{r}, t) = \mathbf{J}_f(\mathbf{r}, t) + \frac{\partial \mathbf{D}(\mathbf{r}, t)}{\partial t}. \tag{2.9}$$

The Maxwell equations introduce the electromagnetic fields, which are the electric displacement $\mathbf{D}(\mathbf{r}, t)$, the magnetic flux density $\mathbf{B}(\mathbf{r}, t)$, the electric field $\mathbf{E}(\mathbf{r}, t)$, and the magnetic field $\mathbf{H}$. These fields can be called as $\mathbf{D}(\mathbf{r}, t)$-field, $\mathbf{B}$-field, $\mathbf{E}$-field, and $\mathbf{H}$-field. We will explain the differences between these four electromagnetic fields in few further paragraphs after we explain the constitutive relation. Equation (2.6) explain the principle that the divergence of the electric displacement $\mathbf{D}$ is proportional to the charge density ρ, signifying the role of electric charges in affecting the spatial variation of the electric displacement field. Proceeding further, we observe that the magnetic field behaves divergentless, having only a rotational component, as illustrated by Eq. (2.7). One of the important things from these equations is the manifestation of Faraday's law, which asserts that a time-varying magnetic field can induce an electric field, as evident from Eq. (2.8). Transitioning to Eq. (2.9), we find out that the presence of an external free electric current $\mathbf{J}_f$ in pair with a time-dependent electric displacement $\mathbf{D}$ acts as a source for the generation of a magnetic field. This equation accentuates the interdependency and intricate relationship between electric and magnetic response.

In the scope of this thesis, we have purposely considering the material that is dispersive. This means that the characteristics of these materials, such as their permittivity and permeability, will vary based on the frequency of the incident electromagnetic wave. This frequency-dependent behavior of materials can significantly influence wave propagation and interaction response. Dispersion necessitates a deeper understanding of how different frequency components interact with the material. One efficient way to delve into this is by employing the Fourier transform. By using the Fourier transform, we can transition from analyzing signals and responses in the time domain to studying them in the frequency domain. This mathematical tool allows us to decompose a time-domain function into a sum of sinusoids of different frequencies, allowing us to reveal the spectrum of frequency components present in the original function. In the context of our study, this means we can evaluate how each individual frequency component of an incident wave interacts with the material, offering a comprehensive view of its dispersive properties. Mathematically, given a function $f(t)$ defined over a continuous range of time t, its Fourier transform $F(\omega)$ is defined as:

$$F(\omega) = \int_{-\infty}^{\infty} f(t)e^{i\omega t}\, dt \tag{2.10}$$

This transformation allows us to define the electromagnetic fields at Eq. (2.6)-(2.9) in frequency domain. By assuming that the solution of the Maxwell equations have electromagnetic fields that is time-harmonic, $\mathbf{A}(\mathbf{r},t) = \mathbf{A}(\mathbf{r})e^{-i\omega t}$, so that the time derivative $(\frac{\partial}{\partial t})$ at the Maxwell equation can be stated as $-i\omega$ and applying convolution operation to the Fourier transform, we can derive the Maxwell equation in frequency domain as

$$\nabla \cdot \mathbf{D}(\mathbf{r},\omega) = \rho_f(\mathbf{r},\omega), \tag{2.11}$$

$$\nabla \cdot \mathbf{B}(\mathbf{r},\omega) = 0, \tag{2.12}$$

$$\nabla \times \mathbf{E}(\mathbf{r},\omega) = i\omega\mathbf{B}(\mathbf{r},\omega) \tag{2.13}$$

$$\nabla \times \mathbf{H}(\mathbf{r},\omega) = \mathbf{J}_f(\mathbf{r},\omega) - i\omega\mathbf{E}(\mathbf{r},\omega). \tag{2.14}$$

However, the Maxwell equations are not enough for understanding and finding the electric field and the magnetic field. There has to be a link from the **D**-field to the **E**-field and **H**-field to the **B**-field. We take an example to the electric field case. When there is an external electric field interact with the dielectric particle, the polarization field **P** is induced since bound charges interact with the electric field having oscillationary feature. The **D**-field is the electric field without the contribution from the polarization field. So that, the contribution of **E**-field is only from the free charge inside the particle, Same also when we consider that there is an external magnetic field, magnetization happens if the particle material is magnetic, and the **H**-field is the contribution from the free current inside and the magnetization field **M**. Looking forward, we assume all of the material used in this thesis is isotropic, linear, local, non-magnetic, and homogeneous in time, so that we have the constitutive relation,

$$\mathbf{D}(\mathbf{r},\omega) = \epsilon_0\mathbf{E}(\mathbf{r},\omega) + \mathbf{P}(\mathbf{r},\omega) = \epsilon_0\epsilon_r(\omega)\mathbf{E}(\mathbf{r},\omega), \tag{2.15}$$

$$\mathbf{B}(\mathbf{r},\omega) = \mu_0\mathbf{H}(\mathbf{r},\omega) - \mathbf{M}(\mathbf{r},\omega) = \mu_r\mu_0\mathbf{H}(\mathbf{r},\omega), \tag{2.16}$$

where we introduce the relative permittivity $\epsilon_r(\mathbf{r},\omega)$ and relative permeabillity $\mu_r(\mathbf{r},\omega)$. The vacuum electric permittivity ϵ_0 and magnetic permeability μ_0 are known constants. Further, we take the **E**-field and **B**-field, indicating the total field that emerge from a scattering event.

To predict the behavior of electromagnetic fields, the Maxwell equations Eq. (2.11)-(2.14) with Eq. (2.15)-(2.16) need to be solved for a given spatial distribution of the material. Even though analytical solutions exist for basic settings, the Maxwell equations are still notably hard to solve.

Note that in this thesis, we assume that there is no external charges and currents as the sources, so that $\rho_f = 0$ and $\mathbf{J}_f = 0$. Also, we assume that the material is homogeneous in space. When Eq. (2.13) is multiplied by a curl ($\nabla\times$) on both sides of the equation, substituting the constitutive relation in Eq. (2.15), an applying vector triple product identity, we can get the electric Helmholtz equation,

$$\nabla^2\mathbf{E}(\mathbf{r},\omega) + k^2(\omega)\mathbf{E}(\mathbf{r},\omega) = 0, \tag{2.17}$$

where k is the wavenumber that can be related to the dispersion relation,

$$k(\omega) = \frac{\omega}{c}\sqrt{\epsilon_r(\omega)} = \omega\sqrt{\epsilon_0\epsilon_r(\omega)\mu_0} \tag{2.18}$$

The magnetic Helmholtz equation can be derived using the same path used to derive 2.17 by beginning with Eq. (2.14) instead of Eq. (2.13). The magnetic Helmholtz equation is

$$\nabla^2\mathbf{B}(\mathbf{r},\omega) + k^2(\omega)\mathbf{B}(\mathbf{r},\omega) = 0. \tag{2.19}$$

Therefore, we can solve the Maxwell equation to find the electric field and the magnetic field by working out on Helmholtz equation in Eq. (2.18) and Eq. (2.19) analytically.

Anyhow, tackling the Maxwell equation can be a formidable challenge due to its intricate nature and the specific interface conditions or geometries one might encounter. Analytically addressing it often involves the application of mathematical techniques like separation of variable method, which seeks to break down the problem into simpler, more manageable parts. Similarly, eigenfunction expansions can be employed, where solutions are expressed as a series in terms of eigenfunctions, thereby enabling us to decompose the complex equation into a set of simpler ones. However, analytical solutions aren't always feasible, especially for more complicated geometries, like non-spherical particles, or non-uniform media. This is where numerical methods come into play when solving the Maxwell equations beside starting by Helmholtz equation. Among these, the finite-difference time-domain (FDTD) method are one of popular method to use [38]. FDTD divides the computational domain into a grid and computes the fields at discrete time steps, making it particularly useful for problems where time-evolution of the field is of interest. On the other hand, the finite element method (FEM) involves dividing the problem domain into smaller, simpler parts called "elements" [39]. By approximating the solution over each of these elements and then assembling them together, FEM can handle complex geometries and materials with varying properties.

2.3 Optical properties of metal

In this section, we explain the basic approach to describe the optical properties of a metal, especially expressing the electric permittivity of a noble metal by a Drude model [40]. Since we study small-sized metallic nanoparticles further in the thesis, a correction to the electric permittivity should be added to make the calculation more accurate when dealing with these nanosized objects. Then, we continue to explore that strong near-field can be induced just outside of a metallic small-sized sphere when we illuminate it by an electromagnetic wave with specific frequency. This resonant response is a localized surface plasmon polariton, which is a reonantly excited charge density oscillation coupled to an electro-magnetic field [41]. Finally, we consider systems consisting of two closely spaced metallic nanoparticles. In these systems, a much stronger near-field emerges inside the gap of the dimer. The details of this situation of two coupled nanoparticles can be explained with modeled with plasmon hybridization theory [42].

2.3.1 Drude model and the size effect

Consider a metal. Inside the metal, there are many free electrons with mass m_e and charge e. They move freely and can collide with each other with damping constant γ_e. There is an external source in form of an external time-harmonic electric field $\mathbf{E}_{\text{ext}} = \mathbf{E}_0 e^{-i\omega t}$ that interact with the electrons. We can study the motion of the electrons by solving the equation of motion,

$$\frac{\partial^2 \mathbf{r}}{\partial t^2} + \frac{\gamma_e}{m_e}\frac{\partial \mathbf{r}}{\partial t} = e\mathbf{E}_0 e^{-i\omega t}. \tag{2.20}$$

We assume also that the solution of this equation is time-harmonic as well so that we can use the ansatz $\mathbf{r}(t) = \mathbf{r}_0 e^{-i\omega t}$. Substituting the ansatz with its time derivatives into Eq. (2.20), we get the solution to Eq. (2.20), which is

$$\mathbf{r}_0 = \frac{e}{m_e}\frac{\mathbf{E_0}}{-\omega^2 - i\gamma\omega}. \tag{2.21}$$

The external electric field oscillates and interacts with the electrons within a metal, driving the electrons to oscillate as well. Given that the metal has an electron density n within a volume V, we can get the polarization density $\mathbf{P}$ by relating to the material properties in form of electric susceptibility χ,

$$\mathbf{P} = \frac{\mathbf{p}}{V} = ne\mathbf{r}_0 = \frac{ne^2}{m_e}\frac{\mathbf{E_0}}{\omega^2 - i\gamma\omega} = \epsilon_0 \chi \mathbf{E}_0. \tag{2.22}$$

The electric susceptibility measures of how much a material becomes polarized in response to an applied electric field. However, the susceptibility only represents the induced part of the response when there is matter in the system and not just vacuum. Therefore, we have to describe the material properties in form permittivity ϵ, since the permittivity holds information about the overall response from the material. Assuming that the metal is linear and isotropic, we can relate the susceptibility to the permittivity by Eq. (2.23),

$$\epsilon = \epsilon_0(1 + \chi) \tag{2.23}$$

Substituting Eq. (2.22) into Eq. (2.23) leads to the Drude permittivity,

$$\epsilon(\omega) = \epsilon_0 \left(1 - \frac{ne^2}{m_e \epsilon_0}\frac{\mathbf{1}}{\omega^2 + i\gamma\omega}\right) = \epsilon_0 \left(1 - \frac{\omega_{\mathbf{p}}^{\mathbf{2}}}{\omega^2 + i\gamma\omega}\right), \tag{2.24}$$

where ω_p is the plasma frequency. At frequencies below the plasma frequency, electromagnetic radiation cannot propagate through the metal and is reflected. Above this frequency, the medium becomes transparent to the radiation, allowing it to pass through. In a metal, the abundance of free electrons gives them a characteristically high plasma frequency. As a result, metals are generally reflective to visible light, which falls below their plasma frequency. Yet, for frequencies much higher than the plasma frequency, such as X-rays, metals can become more transparent, losing their metallic properties.

The Drude model is particularly good at capturing the permittivity characteristics of noble metals like gold and silver. However, when applied to other metals, such as aluminum, the Drude model faces challenges. Specifically, the imaginary part of the electric permittivity for aluminum, when observed experimentally [43], demonstrates an increase of magnitude at higher frequencies. This behavior contrasts with that of noble metals, where the imaginary component decays in a manner that is in harmony with the Drude model's predictions. Note that the Drude model does not consider electronic and atomic structures of materials. It means that the discrepancy in case of aluminum permittivity can be explained through other models.

When the dimension of the metallic structure is getting finite and gets even comparable to the mean-free path of the electrons, the free electron inside the metal will have higher change to collide to each other electron and the boundary of the metal. This suggests to modify the damping constant of the electron by adding to bulk damping coefficient a size dependent factor [44]. This can be expressed as

$$\gamma = \gamma_{\text{bulk}} + \frac{A v_{\text{F}}}{r}. \tag{2.25}$$

A is a constant that relates to the shape of the metal and its value is usually close to one, v_{F} is the velocity of electrons in form of Fermi velocity, and r is the radius of the particle assumed to be a sphere. We can apply the size effect into the experimental permittivity, Johnson and Christy permittivity data [45] for instance, by applying Eq. 2.25 to Eq. 2.24 and add in the experimental permittivity ϵ_{exp}, resulting in

$$\epsilon(\omega) = \epsilon_{\text{exp}}(\omega) + \frac{\omega_p^2}{\omega^2 + i\gamma_{\text{bulk}}\omega} - \frac{\omega_p^2}{\omega^2 + i\gamma\omega}. \tag{2.26}$$

The third term Eq. 2.26 is the size-corrected term and consists of parameters that are intrinsic to the noble metals. Note that the bulk damping coefficient can be determined experimentally by finding the relaxation constant $\tau = 1/\gamma_{\text{bulk}}$ of the metal. These parameters are listed in Table 2.1.

2.3.2 Localized surface plasmon resonance and plasmon hybridization

Consider an external time-harmonic electric field with magnitude E_0 that is applied to a metallic sphere with radius R and electric permittivity ϵ_{sph} in a background with electric permittivity ϵ_{bg}. Analytically, one can determine the electric field both outside and inside the sphere, particularly under the quasistatic approximation [40]. This means that the size of the sphere has to be much smaller than the wavelength of the external field for making sure the fields change slowly.

Table 2.1: Plasma frequency, relaxation constant, and Fermi velocity of copper, silver, and gold

	Cu	Ag	Au
$\omega_p(10^{15}\mathrm{s}^{-1})$	13.4	14.0	13.8
$\tau(10^{-15}\mathrm{s})$	6.9	31	9.3
$v_\mathrm{F}(10^8\mathrm{cm/s})$	1.57	1.39	1.39

The electric field can be found through the electric potential $V(r,\theta)$ by solving the Laplace equation in spherical coordinates,

$$\nabla^2 V(r,\theta) = 0 \quad \rightarrow \quad \frac{1}{r}\frac{\partial^2}{\partial r^2}\left[rV(r,\theta)\right] + \frac{1}{r^2 \sin\theta}\frac{\partial}{\partial\theta}\left[\sin\theta\frac{\partial V(r,\theta)}{\partial\theta}\right] = 0, \tag{2.27}$$

considering no free charge in the metal as a source and no dependency of the potential on azimuthal angle ϕ. Here, we consider that the electric field has polarization along $\hat{z}$ We can solve 2.27 by using separation of variable technique. After a thorough derivation, we can get the electric potential inside the sphere

$$V_\mathrm{inside}(r,\theta) = -\left(\frac{3\epsilon_\mathrm{bg}}{\epsilon_\mathrm{sph}+2\epsilon_\mathrm{bg}}\right)E_0 r\cos\theta, \tag{2.28}$$

and outside the sphere

$$V_\mathrm{outside}(r,\theta) = \left(\frac{\epsilon_\mathrm{sph}-\epsilon_\mathrm{bg}}{\epsilon_\mathrm{sph}+2\epsilon_\mathrm{bg}}\right)\frac{R^3}{r^2}E_0 r\cos\theta - E_0 r\cos\theta. \tag{2.29}$$

As explained before, an electric dipole can be induced due to the presence of electric field oscillation inside the metal. The induced dipole moment $\mathbf{p}$ can be derived from the potential outside the sphere in Eq. (2.29) by using equation below,

$$V(\mathbf{r}) = \frac{1}{4\pi\epsilon_\mathrm{bg}}\frac{\mathbf{p}\cdot\hat{\mathbf{r}}}{r^2},$$

leading to

$$\mathbf{p} = 4\pi\epsilon_\mathrm{bg}\left(\frac{\epsilon_\mathrm{sph}-\epsilon_\mathrm{bg}}{\epsilon_\mathrm{sph}+2\epsilon_\mathrm{bg}}\right)R^2 E_0\hat{\mathbf{z}}. \tag{2.30}$$

We may get interested in the field outside the sphere, so the electric field can be obtained through Eq. 2.29 and taking the derivative of the scalar potential,

$$\mathbf{E}_\mathrm{outside} = -\nabla V_\mathrm{outside} = -\left(\left(\frac{3R^3}{r^3}\right)\left(\frac{\epsilon_\mathrm{sph}-\epsilon_\mathrm{bg}}{\epsilon_\mathrm{sph}+2\epsilon_\mathrm{bg}}\right)+1\right)\hat{\mathbf{z}}. \tag{2.31}$$

From the Drude permittivity presented in Eq. (2.24), it is evident that the real part of the permittivity becomes negative when the plasma frequency exceeds the operating frequency. Assuming that $\epsilon_\mathrm{bg} > 0$, the denominator in Eq. (2.31) becomes negligible, approaching zero. Consequently, the induced dipole moment mentioned in Eq. (2.30) must be resonantly enhanced. This pronounced effect arises at specific frequencies due to the dispersive nature of the permittivity. This resonant response is usually linked to the excitation of a localized surface plasmon resonance (LSPR) for metals, but indeed also other effects can cause the permittivity of a material to take small and negative values. The LSPR is a unique optical effect observed when the external electromagnetic wave, with a specific frequency, drives the oscillation of free electrons within a metal. This collective oscillation of electrons leads to resonance predominantly at the surface or interface between a nanoscale metallic particle and a dielectric background. This response results in the enhancement of the electromagnetic field in the immediate vicinity of the particle, producing a very strong near-field outside of it.

$$\epsilon_{\mathrm{sph}} = -2\epsilon_{\mathrm{bg}}, \tag{2.32}$$

known as the Fröhlich condition. The conditions required to ensure this resonance occurrence include a negative real part of the metal's permittivity, matching the magnitude (but opposite in sign) to the dielectric constant of the surrounding medium, the particle's size and shape, and the incident light's frequency. To find the resonance frequency of a LSPR, we substitute the Fröhlich condition in Eq. (2.32) to the Drude permittivity in Eq. (2.24) and setting the denominator of Eq. (2.24) as the LSPR frequency (ω_{LSPR}). The LSPR frequency is represented as

$$\omega_{\mathrm{LSPR}} \equiv \frac{\omega_{\mathrm{p}}}{\sqrt{1 + 2\frac{\epsilon_{\mathrm{bg}}}{\epsilon_0}}}. \tag{2.33}$$

Finally, one interesting effect occurs when two resonant spheres are placed close to each other. The spheres can interact to each other, strengthening the induced near-field due to LSPR. A noteable theory that explains this interaction is the plasmon hybridization theory [42]. We know that the LSPR of a sphere induces a dipole field. The plasmonic interaction between these dipoles gives rise to hybridization in which creating a combined modes, known as bonding and antibonding modes. The bonding mode arise when the dipoles are in-phase and the antibonding mode emerges when the dipoles are out-of-phase, explained visually in Fig. 2.1. When hybridization occurs, two distinct resonance peaks emerge, representing the bonding and antibonding modes. The higher frequency peak that corresponds to the bonding mode, while the lower frequency relates to the antibonding mode. Capitalizing on the intense near-field that develops in the gap between the spheres offers numerous applications. The strong near-field can act as a source for generating nonlinear optical effects. Additionally, it can enhance the sensitivity of biosensors, allowing for more precise and rapid detection of various biomolecules [46, 47]. Furthermore, in the realm of renewable energy, the strong near-field can be harnessed for solar energy applications, specifically aiding in trapping sunlight more efficiently [48, 49, 50].

2.4 Mie theory to T-matrix of a single particle formalism

The Helmholtz equations, which are generally fundamental in wave physics and acoustics, describe how wave fields evolve in space. When these equations are applied to a spatially localized particle, Mie theory emerges a powerful tool to determine the interactions between incident and scattered waves for a particle smaller than wavelength of the incident wave [51]. At its core, Mie theory proposes a systematic

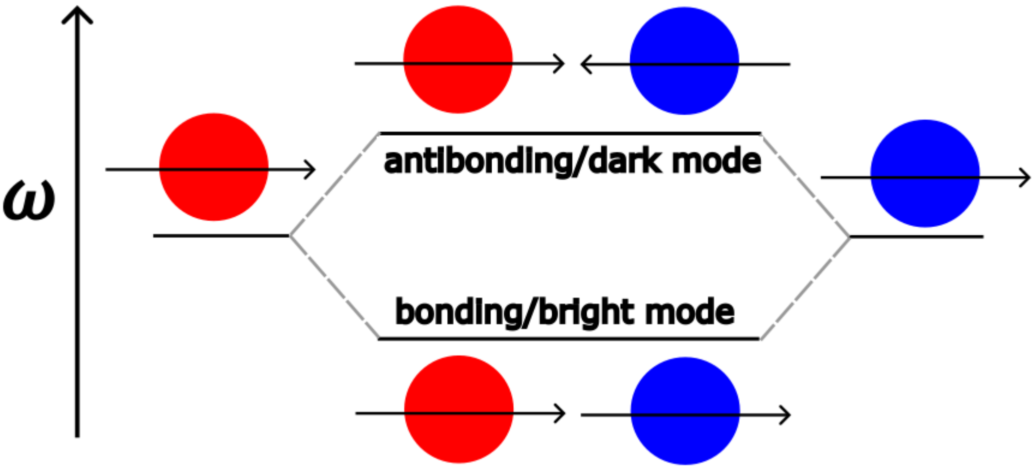

Figure 2.1: Illustration of the plasmon hybridization. Two different spheres characterized in red and blue color interact each other with their dipole phase sketched in arrow.

way to expand both the incident and scattered fields of a localized particle in the frequency domain into vector spherical wave functions (VSWFs). Originally developed by Gustav Mie to describe the interaction of light with a sphere [52], we can use that approach also as a framework to describe the interaction of light with arbitrarily shaped objects. We only require them to be localized in space.

To harness the power of Mie theory, one must first understand the intricacies of VSWFs. VSWFs are derived from the scalar spherical harmonics function, and they take the form of a multiplication between an oscillatory exponential term, an associated Legendre function P_n^m, and spherical Bessel function $z_n^{(i)}$. The associated Legendre function is a direct consequence of the solution to the Helmholtz equation from a sphere within the spherical coordinate system and the spherical Bessel function represents what kind of wave solution it is depending on its type, i.e outgoing and incoming wave. There are two primary type of VSWFs: those with electric parity defined in Eq. (2.34) and magnetic parity defined in Eq. (2.35),

$$\mathbf{M}_{n,m}^{(i)}(\mathbf{r},\omega) = \nabla \times \Big(\mathbf{r} \cdot e^{im\phi} \cdot P_n^m(\cos\theta) \cdot z_n^{(i)}(k\mathbf{r})\Big)\,, \tag{2.34}$$

$$\mathbf{N}_{n,m}^{(i)}(\mathbf{r},\omega) = \frac{c}{\omega\sqrt{\epsilon_{\mathrm{bg}}}}\nabla \times \nabla \times \Big(\mathbf{r} \cdot e^{im\phi} \cdot P_n^m(\cos\theta) \cdot z_n^{(i)}(k\mathbf{r})\Big)\,, \tag{2.35}$$

The electric VSWFs represent the electric field's response in spherical coordinate, also work same with the magnetic ones. They give insight into how the fields interact and scatter around and within the particle. These two types of VSWFs are indispensable in the context of Mie theory. They enable the decomposition of complex electromagnetic fields into more manageable components, therefore facilitating a detailed analysis of scattering response.

The VSWFs are stated with their respective multipolar order n, angular momentum order along a specific axis m, and superscript i. The index n corresponds to the multipolar term, $n = 1$ to the dipolar term, $n = 2$ to the quadrupolar term, and etc. Meanwhile, the superscript i is chosen depending on the type of the radial spherical function $z_n^{(i)}(k\mathbf{r})$ that is used. The functions are spherical Bessel function $(i = 1)$, spherical Neumann function $(i = 2)$, spherical Hankel function of the first kind $(i = 3)$, and spherical Hankel function of the second kind $(i = 4)$. We are interested on finding the incident field and scattered field of a spherical particle, thus we only use the spherical Bessel function for finding the incoming field (choosing that expansion, the fields stay finite at the origin) and the spherical Hankel function of the first kind for determining the scattered field (in that expansion, an outgoing wave condition is satisfied). ϵ_{bg} is the relative permittivity of the sphere background. The VSWFs are orthogonal, so that we can linearly expand the electric field $\mathbf{E}$ at a specific frequency ω in VSWFs as its basis function. The incident field is defined in Eq. (2.36) and the scattered field in Eq. (2.37),

$$\mathbf{E}_{\text{inc}}(\mathbf{r},\omega) = \sum_{n=1}^{\infty} \sum_{m=-n}^{n} a_{0,n,m}\mathbf{N}_{n,m}^{(1)}(\mathbf{r},\omega) + a_{1,n,m}\mathbf{M}_{n,m}^{(1)}(\mathbf{r},\omega), \tag{2.36}$$

$$\mathbf{E}_{\text{sca}}(\mathbf{r},\omega) = \sum_{n=1}^{\infty} \sum_{m=-n}^{n} p_{0,n,m}\mathbf{N}_{n,m}^{(3)}(\mathbf{r},\omega) + p_{1,n,m}\mathbf{M}_{n,m}^{(3)}(\mathbf{r},\omega), \tag{2.37}$$

The expansion comes with their respective expansion coefficients $a_{\alpha,n,m}$ for the incident field and $p_{\alpha,n,m}$ for the scattered field. Notice that we introduce the α to the expansion coefficients, which points to the two parities of multipole, electric multipole $(\alpha = 0)$ and magnetic multipole $(\alpha = 1)$.

The incident expansion coefficients $a_{\alpha,n,m}$ and the scattered expansion coefficients $p_{\alpha,n,m}$ can be related by a matrix equation, known as the T-matrix $\underline{\underline{\mathbf{T}}}$, stated in Eq. (2.38),

$$\begin{pmatrix} p_{\alpha,1,m} \\ p_{\alpha,2,m} \\ \cdots \\ p_{\alpha,n,m} \end{pmatrix} = \underline{\underline{\mathbf{T}}} \begin{pmatrix} a_{\alpha,1,m} \\ a_{\alpha,2,m} \\ \cdots \\ a_{\alpha,n,m} \end{pmatrix}. \tag{2.38}$$

The T-matrix, represented as $\underline{\underline{\mathbf{T}}}$, is a fundamental aspect in our study of scattering by a system of nanoparticles. Its uniqueness signifies that it captures the entire essence of a nanoparticle system's electromagnetic interaction. The power of the T-matrix lies in its ability to act as a comprehensive descriptor of the system, eliminating the need for individualized representations of each nanoparticle. When an incident field interacts with a system of nanoparticles, the T-matrix becomes an instrumental tool in predicting the scattered field. Given that the incident field and the T-matrix of the system are known, someone can determine how the system will scatter this field, revealing the interactions at play at a microscopic level.

But the capabilities of the T-matrix do not end there. By diving deeper into its mathematical structure, one can derive even more physical insights about the system. For instance, optical cross-sections [51, 53], which are vital parameters in understanding how light interacts with particles, can be extracted directly from the T-matrix. We know that the light is absorbed and scattered when interacting with the particle, or get "extinct" in total. The optical cross-sections are the extinction cross-section, absorption cross-section, and the scattering cross-section, in which are defined as the ratio between the power of light that is absorbed or scattered $W_{\text{abs,sca}}$ and the irradiance I_{inc},

$$C_{\text{abs,sca}} = \frac{W_{\text{abs,sca}}}{I_{\text{inc}}}, \tag{2.39}$$

and the extinction cross-section is the summation of absorption cross-section and scattering cross-section,

$$C_{\text{ext}} = C_{\text{abs}} + C_{\text{sca}}. \tag{2.40}$$

Especially for the scattering cross-section and extinction cross-section for an arbitrary particle, it can be derived further by finding the power W in form of Poynting vector $\mathbf{S}$ through an imaginary sphere surrounding the particle with surface area A,

$$W_{\text{inc}} = -\int_A \mathbf{S}_{\text{inc}} \cdot \hat{\mathbf{r}}\, dA, \quad W_{\text{sca}} = \int_A \mathbf{S}_{\text{sca}} \cdot \hat{\mathbf{r}}\, dA, \quad W_{\text{ext}} = -\int_A \mathbf{S}_{\text{ext}} \cdot \hat{\mathbf{r}}\, dA, \tag{2.41}$$

recalling that the Poynting vector in form of electric field $\mathbf{E}$ and magnetic field $\mathbf{H}$ is defined as

$$\mathbf{S} = \mathbf{E} \times \mathbf{H}. \tag{2.42}$$

Meanwhile, the absorbed light power is written as the sum of three terms: $W_{\text{abs}} = W_{\text{inc}} - W_{\text{sca}} + W_{\text{ext}}$. We can get the scattering cross-section assuming that we are in the far-field region leading to that the imaginary sphere has a large radius. This means that the scattered field only has radial component. Then, if we consider unpolarized incident light, we have to take the rotationally average of the cross-sections by calculating the cross-section over all possible direction of the incident field and take the average of all of the illumination. After we substitute Eq. (2.41), (2.36), (2.37), and (2.38), into Eq. (2.39) and (2.40), we can get the expression of scattering and extinction cross-section in form of T-matrix $\underline{\underline{\mathbf{T}}}$ as

$$C_{\text{sca}} = \frac{4\pi}{k_{\text{bg}}^2} \operatorname{Tr}\left(\left|\underline{\underline{\mathbf{T}}}\right|^2\right), \tag{2.43}$$

$$C_{\text{ext}} = -\frac{4\pi}{k_{\text{bg}}^2} \operatorname{Re}\left[\operatorname{Tr}\left(\underline{\underline{\mathbf{T}}}\right)\right], \tag{2.44}$$

where k_{bg} is the wavenumber of the background medium. Basically, by computing the trace of the T-matrix—a process that essentially sums up its diagonal elements—one can determine these cross-sections.

For an isolated spherical object, the T-matrix can be derived analytically. That simplicity renders possible computations extremely accurate and fast. When determining the T-matrix for such an object, it is crucial to consider the interface conditions that dictate the behavior of the electromagnetic field. For a spherical particle, this concerns the surface of the object. Given the geometry and symmetry of a sphere, the electromagnetic field's behavior can be understood by examining its interface conditions. One of the most fundamental principles at play here is the continuity of the tangential components of the electromagnetic field. Applying this fact in form of spherical coordinate, we express the interface condition,

$$\hat{\mathbf{r}} \times \mathbf{E}_{\text{in}}(r,\omega) - \hat{\mathbf{r}} \times \mathbf{E}_{\text{out}}(r,\omega) = 0, \tag{2.45}$$

$$\hat{\mathbf{r}} \times \mathbf{B}_{\text{in}}(r,\omega) - \hat{\mathbf{r}} \times \mathbf{B}_{\text{out}}(r,\omega) = 0, \tag{2.46}$$

where $\mathbf{E}_{\text{in}}$ denotes the component of E tangential to the surface that resides inside the object and $\mathbf{E}_{\text{out}}$ denotes the component of E tangential to the surface outside of the object. By leveraging this principle and integrating it with Maxwell's equations, an analytical expression for the T-matrix can be derived. The single sphere T-matrix have only diagonal elements $T_{\alpha,n,m}$. Further, the single sphere T-matrix is diagonal, and we can find the diagonal elements of the single sphere T-matrix analytically,

$$T_{n,\alpha} = \frac{\mu_{\mathrm{sph}}\varsigma_{\alpha}^{2} z_n^{(1)}(\Omega kR)[kRz_n^{(1)}(kR)]' - \mu_{\mathrm{sph}} z_n^{(1)}(kR)[\Omega kR z_n^{(1)}(kR)]'}{\mu_{\mathrm{bg}}\varsigma_{\alpha}^{2} z_n^{(1)}(\Omega kR)[kRz_n^{(3)}(kR)]' - \mu_{\mathrm{sph}} z_n^{(3)}(kR)[\Omega kR z_n^{(1)}(kR)]'}. \tag{2.47}$$

The subscript sph and bg mean the sphere media and the background media in order. k is the wavenumber, $k = \frac{\omega}{c}\sqrt{\epsilon_{\mathrm{bg}}\mu_{\mathrm{bg}}}$, R is the radius of the sphere, Ω is the wave impedance, $\Omega = \sqrt{\frac{\epsilon_{\mathrm{bg}}\mu_{\mathrm{bg}}}{\epsilon_{\mathrm{sph}}\mu_{\mathrm{sph}}}}$, and the value of ς_{α} depends on the multipole parity considered α,

$$\varsigma_{\alpha} = \begin{cases} \Omega, & \alpha = 0 \\ \\ 1, & \alpha = 1 \end{cases}. \tag{2.48}$$

However, the realm of particles is vast and varied. For those that possess even more convoluted or irregular geometries, the analytical approach often falls short. In these instances, we must turn our attention to numerical methods, such as the finite element method [54]. These computational techniques, while more resource-intensive, offer a versatile solution, enabling us to tackle a broader spectrum of shapes and configurations. Through iterative calculations and simulations, these numerical strategies can approximate the scattering behavior of these complex entities, providing invaluable insights into their interactions with electromagnetic fields.

2.5 Global T-matrix for a cluster of particles

In this thesis, we are not only considering individual spherical nanoparticle, but also a cluster comprising of finite number of spherical nanoparticles. Then, we need to suitably express the scattering response from that cluster of nanoparticles. To extend the formalism, we essentially write the total incident **E**-field of a nanoparticle in a cluster on nanoparticles as a superposition of the external incident **E**-field ($\mathbf{E}_{\mathrm{inc}}^{\mathrm{ext}}$) and the scattered **E**-field from the other nanoparticles [55, 56],

$$\mathbf{E}_{\mathrm{inc},i}^{\mathrm{total}}(\mathbf{r},\omega) = \mathbf{E}_{\mathrm{inc}}^{\mathrm{ext}}(\mathbf{r},\omega) + \sum_{j\neq i}\mathbf{E}_{\mathrm{sca},j}(\mathbf{r},\omega), \tag{2.49}$$

which we call secondary illumination field $\mathbf{E}_{\mathrm{inc}}^{\mathrm{sec}}$. We have discussed the T-matrix of a single nanoparticle, but the formulation explained beforehand is not suitable for a cluster of nanoparticles. For that purpose, we introduce the local T-matrix T_{local} to describe the scattering from a cluster of particles. The local T-matrix of the overall cluster of nanoparticles represent all of the scattering response from all of individual nanoparticles and the interaction between the neighboring nanoparticles. To accommodate the additional illumination on each particle from the scattered field from all the other particles, we extend Eq. (2.38). Equation (2.38) can be written in a T-matrix equation term as

$$\begin{pmatrix} p_{\alpha,1,m} \\ p_{\alpha,2,m} \\ \cdots \\ p_{\alpha,n,m} \end{pmatrix} = \underline{\underline{\mathbf{T}}} \begin{pmatrix} a_{\alpha,1,m} \\ a_{\alpha,2,m} \\ \cdots \\ a_{\alpha,n,m} \end{pmatrix} + \underline{\underline{\mathbf{T}}} \begin{pmatrix} 0 & \tau_{\alpha,1,2}^{(3)} & \cdots & \tau_{\alpha,1,N}^{(3)} \\ \tau_{\alpha,2,1}^{(3)} & 0 & \ddots & \ddots \\ \vdots & \ddots & 0 & \ddots \\ \tau_{\alpha,N,1}^{(3)} & \ddots & \ddots & 0 \end{pmatrix} \begin{pmatrix} p_{\alpha,1,m} \\ p_{\alpha,2,m} \\ \cdots \\ p_{\alpha,n,m} \end{pmatrix} = \underline{\underline{\mathbf{T}}} \begin{pmatrix} a_{\alpha,1,m} \\ a_{\alpha,2,m} \\ \cdots \\ a_{\alpha,n,m} \end{pmatrix}.$$

$$p_{\text{local}} = T_{\text{local}} a_{\text{local}} + T_{\text{local}} \tau^{(3)}_{\text{local}} p_{\text{local}}. \tag{2.50}$$

Equation (2.50) can be rearranged in a form of local T-matrix, T_{local},

$$p_{\text{local}} = (\mathbb{1} - T_{\text{local}} \tau^{(3)}_{\text{local}})^{-1} T_{\text{local}} a_{\text{local}} \tag{2.51}$$

Since the $\mathbf{E}^{\text{int}}_{\text{sec}}$ of a particle is relevant to the scattered field of neighboring particles, we need to find the element matrix $\tau^{(3)}_{\text{local},\alpha,i,j}$, translation coefficients of the particle-ith to the particle-jth. The translation coefficient allows us to describe the scattered field from a particle relative to a different origin. Previously, we assumed that the coordinate center for the calculation was the same as the center point of the particle. Now, we can move the particle from its coordinate center and calculate the field from a different origin. This means we can determine the field from a particle in relation to other particles that are not positioned at the coordinate center of the system. In essence to express the scattered field from particle j as an incident field on particle i. The translation coefficient $\tau^{(3)}_{i,j}$ is related to the properties of VSWF expansion at different position [57, 58],

$$\tau^{(3)}_{i,j}(k(\mathbf{r} - \mathbf{R})) = \sum_{\lambda=1}^{\infty} \sum_{\mu=-\lambda}^{\lambda} \left[\tau^{(3),1}_{\lambda\mu lm}(-k\mathbf{R}) + \tau^{(3),2}_{\lambda\mu lm}(-k\mathbf{R}) \right] \tau^{(1)}_{\lambda,\mu}(k\mathbf{r}), \quad r < R \tag{2.52}$$

$$\tau^{(3)}_{i,j}(k(\mathbf{r} - \mathbf{R})) = \sum_{\lambda=1}^{\infty} \sum_{\mu=-\lambda}^{\lambda} \left[\tau^{(1),1}_{\lambda\mu lm}(-k\mathbf{R}) + \tau^{(1),2}_{\lambda\mu lm}(-k\mathbf{R}) \right] \tau^{(3)}_{\lambda,\mu}(k\mathbf{r}), \quad r > R \tag{2.53}$$

$$\tau^{(1)}_{i,j}(k(\mathbf{r} - \mathbf{R})) = \sum_{\lambda=1}^{\infty} \sum_{\mu=-\lambda}^{\lambda} \left[\tau^{(1),1}_{\lambda\mu lm}(-k\mathbf{R}) + \tau^{(1),2}_{\lambda\mu lm}(-k\mathbf{R}) \right] \tau^{(1)}_{\lambda,\mu}(k\mathbf{r}). \tag{2.54}$$

Equation (2.52) and (2.53) is used for translating the scattered field when the incident field at the center of coordinate and the particle is translated from vector $\mathbf{r}$ to $\mathbf{R}$ and Eq. (2.54) grant us to translate the incident field to a different origin. Then, the translation coefficients in Eq. (2.52)-(2.54) are related to the translation coefficients $\tau^{(n),v}_{\lambda\mu mn}, v = \{1, 2\}$,

$$\begin{gathered} \tau^{(n),1}_{\lambda\mu mn}(kr) = \frac{\gamma_{lm}}{\gamma_{\lambda\mu}} (-1)^m \frac{2\lambda + 1}{\lambda(\lambda + 1)} i^{\lambda - l} \sqrt{\pi \frac{(l + m)!(\lambda - \mu)!}{(l - m)!(\lambda + \mu)!}} \\ \sum_{n=1} \sum_{p=\lambda+l-(2n-1)}^{\max([\lambda - l], [\mu - m])} \left[i^p \sqrt{2p + 1} z^{(n)}_p (kr) Y_{p,m-\mu}(\hat{\mathbf{r}}) \begin{pmatrix} l & \lambda & p \\ m & -\mu & -m + \mu \end{pmatrix} \begin{pmatrix} l & \lambda & p \\ 0 & 0 & 0 \end{pmatrix} \right. \\ \left. \{ l(l + 1) + \lambda(\lambda + 1) - p(p + 1) \} \right] \end{gathered} \tag{2.55}$$

$$\begin{gathered} \tau^{(n),2}_{\lambda\mu mn}(kr) = \frac{\gamma_{lm}}{\gamma_{\lambda\mu}} (-1)^m \frac{2\lambda + 1}{\lambda(\lambda + 1)} i^{\lambda - l} \sqrt{\pi \frac{(l + m)!(\lambda - \mu)!}{(l - m)!(\lambda + \mu)!}} \\ \sum_{n=1} \sum_{p=\lambda+l-(2n-2)}^{\max([\lambda - l], [\mu - m])} \left[i^p \sqrt{2p + 1} z^{(n)}_p (kr) Y_{p,m-\mu}(\hat{\mathbf{r}}) \begin{pmatrix} l & \lambda & p \\ m & -\mu & -m + \mu \end{pmatrix} \begin{pmatrix} l & \lambda & p - 1 \\ 0 & 0 & 0 \end{pmatrix} \right. \\ \left. \sqrt{[(l + \lambda + 1)^2 - p^2][p^2 - (l - \lambda)^2]} \right] \end{gathered} \tag{2.56}$$

The 3x2 matrices at Eq. (2.55) and Eq. (2.56) are the Wigner 3j-symbol.

The local T-matrix primarily operates within a defined correlation between individual particles. This makes it effective for localized problems but insufficient when addressing the collective behavior. In contrast, the global T-matrix offers a better approach by integrating the properties of each nanoparticle in the cluster, meaning that we can understand a more comprehensive picture of their combined scattering response. This translation from local to global coordinates is made possible by translating the local Mie coefficients, which inherently describe the scattering behavior of single particles, to a global coordinate system centered at $\mathbf{r}_0$. This is especially crucial in research and applications where the interplay between nanoparticles in a cluster can lead to unique optical response, which would not be clear when looking at individual nanoparticles in isolation. The global scattered coefficient p_{global} are related to the the local scattered coefficient p_{local} as

$$p_{\text{global}} = \begin{pmatrix} \tau^{(3)}_{0,1} & \tau^{(3)}_{0,2} & \cdots & \cdots & \tau^{(3)}_{0,N} \end{pmatrix} p_{\text{local}}, \tag{2.57}$$

and

$$a_{\text{global}} = \begin{pmatrix} \tau^{(1)}_{1,0} \\ \tau^{(1)}_{2,0} \\ \cdots \\ \cdots \\ \tau^{(1)}_{N,0} \end{pmatrix} a_{\text{local}}. \tag{2.58}$$

By substituting Eq. (2.57) and (2.58) to Eq. (2.50), the global T-matrix formulation is derived as

$$p_{\text{global}} = \begin{pmatrix} \tau^{(3)}_{0,1} & \tau^{(3)}_{0,2} & \cdots & \cdots & \tau^{(3)}_{0,N} \end{pmatrix} (\mathbb{1} - T_{\text{local}}\tau^{(3)}_{\text{local}})^{-1} T_{\text{local}} \begin{pmatrix} \tau^{(1)}_{1,0} \\ \tau^{(1)}_{2,0} \\ \cdots \\ \cdots \\ \tau^{(1)}_{N,0} \end{pmatrix} a_{\text{global}}$$

$$p_{\text{global}} = T_{\text{global}} a_{\text{global}} \tag{2.59}$$

2.6 Scattering from a two-dimensional periodic layer

We have just demonstrated how to calculate the scattering response of a cluster of nanoparticles. When such a cluster is periodically and infinitely arranged in two dimensions, it forms a consistent layer. In essence, it forms a grating from which we wish to calculate reflection and transmission for a given illumination. This requires to consider the interaction of some central unit cell with all the other unit cells forming the lattice, a process that we sometimes call renormalization [59]. Specifically, we introduce the Ewald summation, a mathematical approach pivotal for efficiently computing interactions in periodic systems [60]. On other hand, we explore the Q-matrix method, an essential tool for deriving the reflection and the transmission coefficient from an individual layer [61]. Both methods are combined with the T-matrix methods explain previously.

Consider a periodic layer that consists of a lattice of clusters. Please be reminded that each of these clusters consists of a larger number of individual metallic nanoparticles that are tightly packed. The layer is illuminated with a plane wave. The plane wave has to be expended into spherical waves since we are dealing with spherical particles inside the lattice. We adopt Eq. (2.51) that express the scattered Mie coefficients to the individual contribution within a lattice and the interaction with all the other particles forming the lattice,

$$p_{\text{layer}} = (\mathbb{1} - T_{\text{lattice}} \sum_{\mathbf{R}}{}' \tau^{(3)}_{\text{lattice}} e^{i\mathbf{k}_{\parallel}\cdot\mathbf{R}'})^{-1} T_{\text{lattice}} a_{\text{layer}} = (\mathbb{1} - U)^{-1} T_{\text{lattice}} a_{\text{layer}} \tag{2.60}$$

where $\mathbf{R} = m_1\mathbf{a}_1 + m_2\mathbf{a}_2$ is the lattice points in term of lattice constant $m_{1,2}$ and primitive vector $\mathbf{a}_{1,2}$. Notice that we do not consider the origin, indicated by primed sum of Eq. (2.60). The difference between Eq. (2.51) and Eq. (2.60) is that the translation coefficient inside Eq. (2.60) accomodates the interaction between all of the periodic lattices by the lattice summation U, instead of particles inside a lattice that interact locally. When attempting to compute the interactions in a layer characterized by an infinite lattices, especially over long ranges, it becomes impractical or even impossible to sum over all pairs of unit cells directly. Therefore, lattice summation techniques exploit the translational symmetry to drastically reduce the computational effort needed to calculate total interaction. Common methods include the Ewald summation [60] and non-Ewald summations, like Wolf summation [62]. In the following, we give an overview the Ewald summation [63].

2.6.1 Ewald summation

Some interactions between the unit cells forming the lattice can be short-range and only affect nearby neighbors, or can have effects over long distances. Computing all these interactions directly, especially for large systems, becomes computationally expensive and often infeasible. Ewald summation allows to compute efficiently the long-range interactions between the unit cell in a periodic lattice system. The basic idea behind Ewald summation is to split the calculation of the interactions into two parts: one in short-range and one in long-range. This separation allows for the summation of each part to converge more rapidly than if one were trying to compute the potential directly over all particle pairs in the system. According to Eq. (2.60) and the concept of the Ewald summation, we separate U into three terms,

$$U_{lm}(\mathbf{k}) = U_{\text{short},lm}(\mathbf{k}) + U_{\text{long},lm}(\mathbf{k}) + U_{\text{corr},lm}(\mathbf{k}). \tag{2.61}$$

A third term $U_{\text{corr},lm}(\mathbf{k})$ is added to Eq. 2.61 to correct the overall summation since the summation does not use periodic condition. In this thesis, we do not approach the full derivation of the decomposition, but the thesis by Beutel had done a great job deriving the Ewald summation that consist of the VSWFs.

The short-range summation is derived by introducing the integral representation of the spherical Hankel functions and the decomposition formula in a paper by Solbrig *et al.*, done in real space, we can get

$$U_{\text{short},lm}(\mathbf{k}) = \frac{-i\sqrt{\frac{2l+1(l-m)!}{4\pi(l+m)!}}P_l^m(0)}{\sqrt{\pi}} \sum_{R} e^{i\mathbf{k}_{\parallel}\cdot\mathbf{R}+im\phi_{-\mathbf{R}}} \frac{1}{k}\left(\frac{2R}{k}\right)^l \int_{T^2}^{\infty} u^{l-\frac{1}{2}} e^{-R^2u+\frac{k^2}{4u}}\, du. \tag{2.62}$$

The integral $I_1(k,R) = \frac{1}{k}\left(\frac{2R}{k}\right)^l \int_{T^2}^{\infty} u^{l-\frac{1}{2}} e^{-R^2u+\frac{k^2}{4u}}\ du$ can be solved by the recursion relation

$$\left(\frac{2RT^2}{k}\right)^l \frac{1}{R^2kT} e^{-r^2T^2+\frac{k^2}{4T^2}} = I_l(k,R) + \frac{1-2l}{rk} I_{l-1}(k,R) + I_{l-2}(k,R). \tag{2.63}$$

Since we want to determine $I_1(k,R)$, we need to know $I_0(k,R)$ and $I_{-1}(k,R)$. They can be expressed by a linear combination of Faddeeva function w,

$$I_0(k,R) \pm I_{-1}(k,R) = \frac{\sqrt{\pi}}{kR} e^{-(RT)^2+\left(\frac{k}{2T}\right)^2} w\left(iRT \pm \frac{k}{2T}\right). \tag{2.64}$$

Then, the long-range summation $U_{\text{long},lm}$ is calculated in reciprocal space to reduce some errors from the calculation of the short-range summation in real space. By using the Fourier transform properties, the contributions emerging from the long-range interaction convergence more rapidly. By introducing the reciprocal lattice vector $\mathbf{G} = M_1\mathbf{b}_1 + M_2\mathbf{b}_2$, with the reciprocal lattice constant $M_{1,2}$ and reciprocal primitive vector $\mathbf{b}_{1,2}$, the final form of $U_{\text{long},lm}$ can be expressed using the incomplete gamma function Γ as

$$\begin{aligned} U_{\text{long},lm}(\mathbf{k}) = \frac{i^m\sqrt{(2l+1)(l-m)!(l+m)!}}{Ak} \sum_{\mathbf{G}} \left(\frac{\left|\mathbf{k}_\parallel + \mathbf{G}\right|}{2k}\right)^l \frac{e^{im\phi_{\mathbf{k}_\parallel+\mathbf{G}}}}{\Gamma_{\mathbf{k}_\parallel+\mathbf{G}}} \\ \cdot \sum_{\lambda=0}^{\frac{l-|m|}{2}} \frac{\left(\frac{\Gamma_{\mathbf{k}_\parallel+\mathbf{G}}}{\left|\mathbf{k}_\parallel+\mathbf{G}\right|}\right)^{2\lambda}}{\lambda!\left(\frac{l+m}{2}-\lambda\right)!\left(\frac{l-m}{2}-\lambda\right)!} \Gamma\left(\frac{1}{2}-\lambda, -\frac{\Gamma^2_{\mathbf{k}_\parallel+\mathbf{G}}}{4T^2}\right). \end{aligned} \tag{2.65}$$

Next, the correction to the Ewald summation must be included to remove errors from the short and long-range summation. The correction is related to an additional self-interaction, because particles now interact with their periodic images, these self-interactions need to be subtracted. This correction is expressed as

$$U_{\text{corr},lm}(\mathbf{k}) = \frac{\delta_{l0}}{4\pi}\Gamma\left(-\frac{1}{2}, -\frac{k^2}{4T^2}\right). \tag{2.66}$$

It is important to determine the appropriate value for the coefficient T in Eq. (2.62), Eq. (2.65), and Eq. (2.66) in advance to ensure that the individual terms vanish quickly as the vector length increases. Additionally, the exponential in the integral representation of the spherical Hankel function used for deriving the $U_{\text{short},lm}$ should be consistent for both the real and reciprocal space components. Also, it is noted that the equations previously use spherical wave as the basis, we have to revert back the Ewald summation to the plane wave basis since the layer mostly is defined as a planar structure, it is better to represent the formulation in Cartesian coordinate and propagation in plane wave is much more likely.

We can represent the total scattered field $\mathbf{E}_{\text{sca}}$ from the lattice scattered Mie coefficient p_{layer} in Eq. (2.60) to relate the formulation to reflection and transmission coefficient further in form of

$$\mathbf{E}(\mathbf{r}) = \sum_{s=\pm}\sum_{d=\updownarrow}\sum_{G} E_{G,sd} e^{i\mathbf{k}_{G,sd}\cdot\mathbf{r}}, \tag{2.67}$$

where

$$E_{G,sd} = \sum_{l=1}^{\infty} \sum_{m=-l}^{l} \frac{2\pi\gamma_{lm}}{Ak_s\Gamma_{\mathbf{G},s} i^{l+1}} \left(\frac{m}{\sin\theta} P_l^m(\cos\theta) + s\frac{\partial}{\partial\theta} P_l^m(\cos\theta) \right). \tag{2.68}$$

Note that, the formulation here is in helicity basis. We can convert the field from the helicity basis into parity basis (TM and TE polarization) later thereafter.

2.6.2 Propagation in multilayer system by Q-matrix method

Until now, we have derived the scattered field from a two-dimensional infinitely extending layer in Eq. (2.68). Taking our analysis further, we now expand our focus from a single layer to a more complex multilayer system. Our primary objective is to determine the reflection and transmission coefficients arising from interactions within this system. A paper by Beutel *et al.* [61] explains a method that is not only fast but also efficient. This approach is referred to as the "Q-matrix method." The essence of the Q-matrix lies in its ability to establish a connection between the incoming fields, both from above and below the layer, and the outgoing fields from the layer. This relationship is shown in the matrix equation presented in Eq. (2.69).

$$\begin{pmatrix} \mathbf{E}_{\uparrow}^{\text{above}} \\ \mathbf{E}_{\downarrow}^{\text{below}} \end{pmatrix} = \begin{pmatrix} \underline{\underline{\mathbf{Q}}}_{\uparrow\uparrow} & \underline{\underline{\mathbf{Q}}}_{\uparrow\downarrow} \\ \underline{\underline{\mathbf{Q}}}_{\downarrow\uparrow} & \underline{\underline{\mathbf{Q}}}_{\downarrow\downarrow} \end{pmatrix} \begin{pmatrix} \mathbf{E}_{\uparrow}^{\text{below}} \\ \mathbf{E}_{\downarrow}^{\text{above}} \end{pmatrix} \tag{2.69}$$

In the context of Eq. (2.69), the first arrow in the subscript of the Q-matrix element indicates the where the field propagation direction and the second arrow expresses the outgoing field propagation direction. For example, in this case, $\underline{\underline{\mathbf{Q}}}_{\downarrow\uparrow}$ means that it is the Q-matrix element that represent the field coming from and to above the layer. Then, the superscript denotes region where the field reside. When considering a multilayer system, each Q-matrix is a representation of the propagation inside a single layer. It is noted also that one observes that an incoming field in one layer could very well correspond to an outgoing field in another layer, and the reverse holds true as well. So that, for a multilayer system, all layers are considered in the process.

The Q-matrix calculation is done in slices. There are interfaces, bulk layers, and layers that contain particles. Figure 2.2 visualizes an example of a multilayer system with their definition of the slices. The Q-matrix elements of an interface between two bulk layers can be calculated as

$$Q_{dd',GG',ss'} = \begin{cases} \delta_{GG'} t_{ss',d}, d = d' \\ \delta_{GG'} r_{ss',d}, d \neq d' \end{cases}, \tag{2.70}$$

where the t and the r is the transmission coefficient and reflection coefficient in order. The first case in Eq. (2.70) is used for an interface that represent the top and bottom edge of a multilayer system and the second case is applied for the interface between layers inside the multilayer system. Next, the field can propagate through a bulk layer, a layer made of homogenous medium. The Q-matrix elements for this homogeneous layer are

$$Q_{dd',GG',ss'} = \delta_{dd'}\delta_{GG'}\delta_{ss'} e^{i\mathbf{k}_{G,sd}\cdot\mathbf{d}}. \tag{2.71}$$

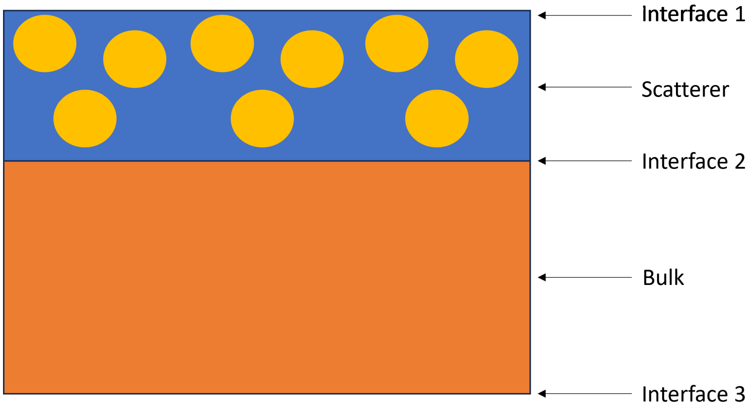

Figure 2.2: Definition of the slices in the Q-matrix method.

The Kronecker Delta in Eq. (2.70) and Eq. (2.71) shows whatever diffraction orders appears in the bulk layer with wavevector $\mathbf{k}_{G,sd}$. The dummies d, G, s are still related to the dummies explained in the Ewald summation chapter. The vector $\mathbf{d}$ determine the center point of the slice relative to its edge. Lastly, the particle in a layer slice has Q-matrices elements to the expansion coefficents that has been modified with Ewald summation in Eq. (2.61). As the last step, we have to combine all of the slices in the multilayer system.

Finally, we can do some post-processing after we obtained the Q-matrix. At first, we can get the expansion Mie coefficients of an electric field, outside and inside the layer. The relations between the Q-matrix element to the expansion coefficients of outgoing wave below and above the multilayer system are

$$\mathbf{E}_{\uparrow}^{\text{above}} = (\mathbb{1} - \underline{\underline{\mathbf{Q}}}^{a}_{\uparrow\downarrow}\underline{\underline{\mathbf{Q}}}^{b}_{\downarrow\uparrow})^{-1}\underline{\underline{\mathbf{Q}}}^{a}_{\uparrow\uparrow}\mathbf{E}_{\uparrow}^{a} + \underline{\underline{\mathbf{Q}}}^{a}_{\downarrow\uparrow}(\mathbb{1} - \underline{\underline{\mathbf{Q}}}^{a}_{\uparrow\downarrow}\underline{\underline{\mathbf{Q}}}^{b}_{\downarrow\uparrow})^{-1}\underline{\underline{\mathbf{Q}}}^{b}_{\downarrow\downarrow}\mathbf{E}_{\downarrow}^{b}, \tag{2.72}$$

$$\mathbf{E}_{\downarrow}^{\text{below}} = \underline{\underline{\mathbf{Q}}}^{b}_{\downarrow\uparrow}(\mathbb{1} - \underline{\underline{\mathbf{Q}}}^{a}_{\uparrow\downarrow}\underline{\underline{\mathbf{Q}}}^{b}_{\downarrow\uparrow})^{-1}\underline{\underline{\mathbf{Q}}}^{a}_{\uparrow\uparrow}\mathbf{E}_{\uparrow}^{a} + (\mathbb{1} - \underline{\underline{\mathbf{Q}}}^{a}_{\uparrow\downarrow}\underline{\underline{\mathbf{Q}}}^{b}_{\downarrow\uparrow})^{-1}\underline{\underline{\mathbf{Q}}}^{b}_{\downarrow\downarrow}\mathbf{E}_{\downarrow}^{b}. \tag{2.73}$$

Starting from this point, determining the reflection and transmission coefficient becomes feasible, as they correlate directly to the expansion coefficients of the electric field, as highlighted in Eq. 2.72 and Eq. 2.73. The directionality of the incoming wave plays a pivotal role in this determination. To illustrate, when the incoming field approaches from a downward trajectory, the reflection coefficient is derived from Eq. 2.72. Conversely, for the calculation of the transmission coefficient, one would reference Eq. 2.73.

2.7 Homogenization of a layer

Up until this point, our discussion has focused on the characterization of thin films without delving into the optimization of their properties. As outlined in the previous sections, our approach involves defining the arrangement of particles within the film using a fixed filling fraction and dimensions of the unit cell comprising these particles. Therefore, adjusting the thickness of the thin film in a continuous fashion is challenging, as it would entail introducing empty gaps between the top and bottom of the film within the particles packing domain. To overcome this challenge, one viable solution is to homogenize the thin film containing the metallic nanoparticles, effectively treating it as a continuous medium with bulk properties [15, 64, 65, 66, 67]. This allows us to represent the thin film as a whole, characterized by its effective electric relative permittivity (ϵ_{eff}) and effective relative magnetic permeability (μ_{eff}), simplifying the analysis and enabling a more comprehensive exploration to the properties of the film. That is possible because once we know the effective properties, we can treat it as a homogeneous film and can continuously change its thickness in the analysis.

Prior to delving into the methodology for determining the effective relative permittivity of a thin film, it is essential whether the system in question is indeed feasible to homogenization. We can turn to the valuable insights provided by Zerulla *et al.* [67]. Their work presents an approach to determine whether a material can be homogenized or not by exploring their band structure, facilitated through the utilization of an effective T-matrix. Meanwhile, the band structure itself can be derived by solving the eigenvalue equation associated with the material starting from the Q-matrix [68, 69]. Not that the unit cells inside the film has lattice vector $\mathbf{a}_3$ in z-axis. Because that the plane wave from the N-th slice reaching the adjacent slice becomes generalized Bloch waves with property

$$\mathbf{E}^{\uparrow\downarrow}(N+1) = e^{i\mathbf{k}\cdot\mathbf{a}_3}\mathbf{E}^{\uparrow\downarrow}(N), \tag{2.74}$$

where the arrow is a notation whether the electromagnetic coming from below or above, stated previously in Eq. (2.69). Note that the wavevector $\mathbf{k}$ is a function of $\mathbf{k}_{\parallel}$ and the z-component of the wavevector k_z. We will find the band structure in form of k_z through the $\mathbf{k}$. Then, the electric fields at slice N-th and $N+1$-th are connected through the elements of the Q-matrix as follows

$$E^{\uparrow}_{N+1} = Q_{\uparrow\uparrow}E_{\uparrow,N} + Q_{\uparrow\downarrow}E_{\downarrow,N+1}, \tag{2.75}$$

$$E^{\downarrow}_{N} = Q_{\downarrow\uparrow}E_{\uparrow,N} + Q_{\downarrow\downarrow}E_{\downarrow,N+1}. \tag{2.76}$$

Substituting Eq. (2.74) to Eq. (2.75) and Eq. (2.76), we can get an eigenvalue equation,

$$\begin{pmatrix} Q_{\uparrow\uparrow} & Q_{\uparrow\downarrow} \\ -[Q_{\downarrow\downarrow}]^{-1}Q_{\downarrow\uparrow}Q_{\uparrow\uparrow} & [Q_{\downarrow\downarrow}]^{-1}[\mathbb{1} - Q_{\downarrow\uparrow}Q_{\downarrow\downarrow}] \end{pmatrix} \begin{pmatrix} E_{\uparrow,N} \\ E_{\downarrow,N+1} \end{pmatrix} = e^{i\mathbf{k}\cdot\mathbf{a}_3} \begin{pmatrix} E_{\uparrow,N} \\ E_{\downarrow,N+1} \end{pmatrix}. \tag{2.77}$$

So that by finding the eigenvalues of Eq. (2.77), we can find a set of numbers that is equal to $e^{i\mathbf{k}\cdot\mathbf{a}_3}$ for a given parallel wave vector component $\mathbf{k}_{\parallel}$ and frequency ω.

The upper frequency up to which we consider a material to be homogenizable can be derived from a basic condition. The condition that we impose on the band structure is that the second derivative of the frequency (f) to the wavenumber component perpendicular to the thin film (k_z) is equal to zero [67],

$$\frac{\partial^2 f}{\partial k_z^2} = 0. \tag{2.78}$$

For all frequencies below that condition, we expect the material to be homogenizable. At the frequency where this condition is met, the dispersion relation is roughly in the center of the Brillouin zone, and we expect that the electromagnetic field does not experience the spatial periodicity of the underlying medium. For example, in

Fig. 2.3, the band-structure of an example of a thin film shows that there is no discontinuity along all of the frequency considered. This means that this thin film is homogenizable in the entire spectrum.

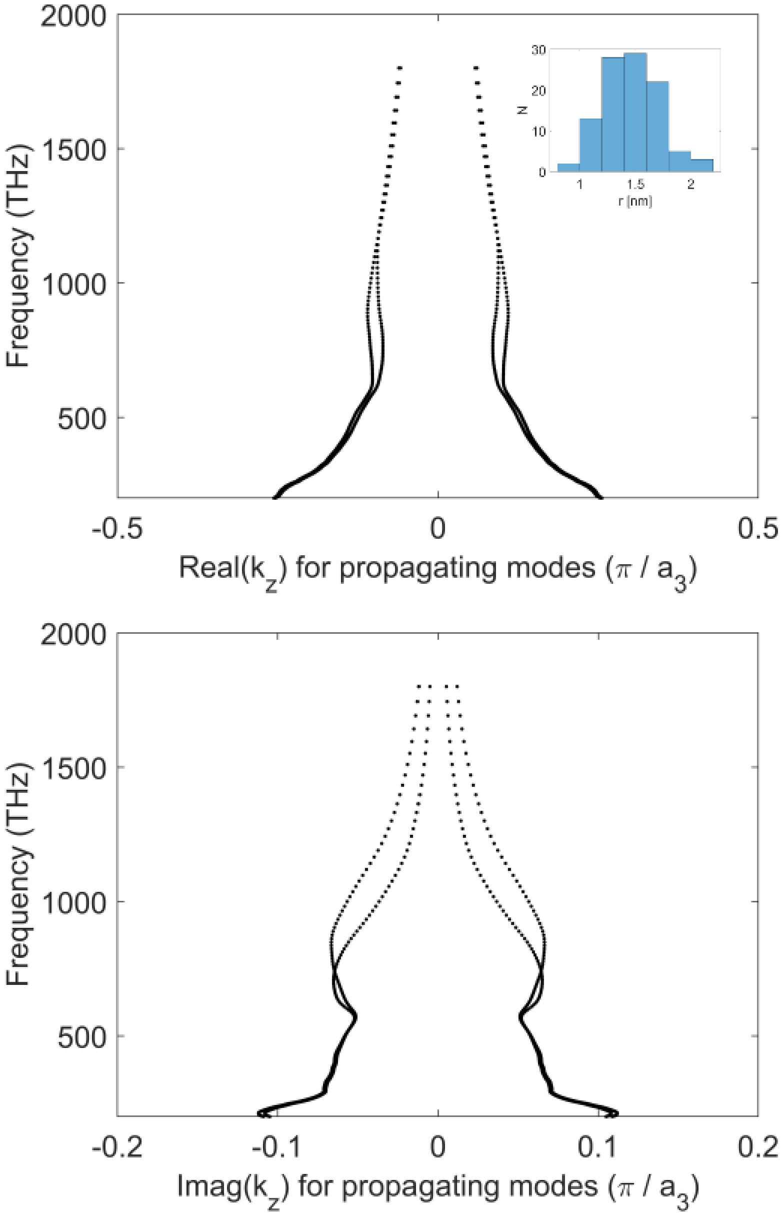

Figure 2.3: (a) The real component and (b) imaginary component of the band structure of a thin film consisting of copper nanoparticles in alumina media. Total number of nanoparticles = 102, filling fraction = 58% and the thickness of the film = 16.1 nm. The inset shows the size distribution of the copper nanoparticles.

In this thesis, effective medium retrieval method is used to homogenize the thin film containing the nanoparticles [70, 71]. This method considers the reflection and transmission coefficient from a thin film with given thickness. The approach basically takes the reflection and transmission coefficient from the actual film and tries to identify the effective material parameters of a homogeneous thin film that would give the same reflection and transmission coefficient. Within the application of this method in this thesis, we assume linear-polarized plane-wave illumination at normal incidence and the thin film is surrounded by a vacuum. The thin film at the effective level is made from an isotropic, homogeneous, local medium, and without electromagnetic coupling. We can find the ϵ_{eff} and the μ_{eff} once we know the effective wavenumber and its effective impedance by

$$\epsilon_{\text{eff}} = \frac{k_f}{\eta_f}, \tag{2.79}$$

$$\mu_{\text{eff}} = \left(\frac{k_f c}{\omega}\right)^2 \left(\frac{\eta_f}{k_f}\right), \tag{2.80}$$

where parameters k_f and η_f are defined as

$$\eta_f = i\sqrt{\frac{k_s^2(r-1)^2 - k_c^2(t)^2}{(t)^2-(r+1)^2}}, \tag{2.81}$$

$$k_f = \left(-\cos^{-1}\left(\frac{k_s - r^2k_s + (t)^2k_c}{(k_s+k_c-k_st+k_cr)(t)}\right) + 2\pi m\right)\left(\frac{1}{d}\right), \tag{2.82}$$

where integer m is the branch order. The branch order is picked at the start of the method to ensure continuity of the wave vector in the respective medium. The subscript f, s, and c mean the film, substrate, and cladding in order. We can make Eq. (2.81) and Eq. (2.82) much simpler because the substrate and the cladding are set as vacuum, so that wavenumber of the substrate and the cladding is equal, $k_s = k_c = \frac{2\pi}{\lambda}$, where λ is the wavelength of the incoming wave.

2.8 Transfer-matrix method

The transfer-matrix method is an elegant approach deeply rooted in linear algebra, which provides a systematic way to analyze multilayer systems, commonly encountered in optics and photonics [40, 72]. Given that real-world applications often involve various materials with distinct optical properties, this method is invaluable for predicting how light interacts with layered structures. When light encounters such a system, it undergoes multiple reflections and transmissions at each interface. By using the transfer-matrix method, these interactions are represented by matrices, and their cumulative effect is determined by the multiplication of these matrices in a specific sequence. This results in a global matrix, from which the overall reflection and transmission coefficients of the entire structure can be derived. Furthermore, the method's versatility is highlighted by its capability to handle both transverse electric (TE) polarized and transverse magnetic (TM) polarized light. Also, the transfer-matrix method can accommodate oblique incidences.

We start by assuming that its interfaces are within the x-y plane. We consider full invariance in y-direction, and the incident plane wave has a wavevector in the x-z plane. We start the mathematical derivation of the transfer matrix by assuming two type of linear polarization, transverse electric (TE) and transverse magnetic (TM), as two separate problems. We assume that the field is invariance in x-axis, so that

$$\mathbf{E}(x,z) = \mathbf{E}(z)e^{ik_x x}, \tag{2.83}$$

$$\mathbf{H}(x,z) = \mathbf{E}(z)e^{ik_x x}. \tag{2.84}$$

It is noted for the TE polarization, we choose the component of the electric field points into the y-direction $E_y(z)$, since the tangential component of the electric field is continuous along the y-axis in the TE polarization. So that, the only the magnetic field that matters ($H_x(z)$) in the plane of propagation, x-z plane. Substituting Eq. (2.83) and Eq. (2.84) into the Helmholtz equation yields

$$i\omega\mu_0 H_x(z) = \frac{\partial}{\partial z}E(z). \tag{2.85}$$

For TM polarization we have to consider the H-field that is parallel to the y-axis. Following the same approach as in the TE case, we can get the expression for the TM polarization,

$$-i\omega\epsilon_0 E_x(z) = \frac{1}{\epsilon_f}\frac{\partial}{\partial z}H(z), \tag{2.86}$$

the subscript f means the region inside the film. Then, we can generalize Eq. (2.85) and Eq. (2.86) for both polarization cases that

$$G(z) = \varrho\frac{\partial}{\partial z}F(z), \tag{2.87}$$

where for TE polarization case, $G(z) = i\omega\mu_0 H_x(z), F(z) = E(z), \varrho = 1$, and for TM polarization case, $G(z) = -i\omega\epsilon_0 E_x(z), F(z) = H(z), \varrho = 1/\epsilon_f$. Then, since we know the incoming field at the interface between the substrate (the region where the incident field propagates initially before contacting the film's interface) and the film, or we can say that at $z = 0$, we can solve an initial value problem by choosing a suitable ansatz. We consider the ansatz

$$F(z) = C_1 e^{ik_{f,z}z} + C_2 e^{-ik_{f,z}z}. \tag{2.88}$$

Here, the C_1 and C_2 coefficients are to be determined from the interface conditions that the tangential component of the electric field is continuous at the interface of the film, in this case at $z = 0$. This means that

$$F(0) = C_1 + C_2, \tag{2.89}$$

and

$$G(0) = i\varrho k_{f,z}[C_1 - C_2]. \tag{2.90}$$

The $k_{f,z}$ is the z-component of the $\mathbf{k}_f$. Since we have two equations as a requirement to find C_1 and C_2, we get

$$C_1 = \frac{1}{2}\left[F(0) - \frac{i}{\varrho k_{f,z}}G(0)\right], \tag{2.91}$$

and

$$C_2 = \frac{1}{2}\left[F(0) + \frac{i}{\varrho k_{f,z}}G(0)\right]. \tag{2.92}$$

At last we know the constants C_1 and C_2, so that we can substitute the constants to the ansatz $F(z) = C_1 e^{ik_{f,z}} + C_2 e^{ik_{f,z}}$, yields

$$F(z) = \cos(k_{f,z}z)F(0) + \frac{1}{\varrho k_{f,z}} \sin(k_{f,z})G(0), \tag{2.93}$$

and

$$G(z) = -\varrho k_{f,z} \sin(k_{f,z})F(0) + \cos(k_{f,z}z)G(0). \tag{2.94}$$

We can write Eq. (2.93) and Eq. (2.94) as a matrix equation,

$$\begin{pmatrix} F(z) \\ G(z) \end{pmatrix} = \hat{\mathbf{m}} \begin{pmatrix} F(0) \\ G(0) \end{pmatrix}. \tag{2.95}$$

The $\hat{\mathbf{m}}$ is the transfer matrix for a single slab, that is represented as

$$\hat{\mathbf{m}} = \begin{pmatrix} \cos(k_{f,z}z) & \frac{1}{\varrho k_{f,z}} \sin(k_{f,z}z) \\ -\varrho k_{f,z} \sin(k_{f,z}) & \cos(k_{f,z}z). \end{pmatrix} \tag{2.96}$$

Further on, we can determine the transfer matrix of a multilayer system that has total a thickness D consisting of N individual layers with thickness $d = d_1, d_2, ..., d_N$ by computing the product of all the individual transfer matrices associated with each layer. This process is mathematically represented by Eq. (2.97),

$$\begin{pmatrix} F(z) \\ G(z) \end{pmatrix}_{d_1+d_2+...+d_N=D} = \prod_{i=1}^{N} \hat{\mathbf{m}}_i(d_i) \begin{pmatrix} F(z) \\ G(z) \end{pmatrix}_0 = \hat{\mathbf{M}} \begin{pmatrix} F(z) \\ G(z) \end{pmatrix}_0, \tag{2.97}$$

which systematically combines these matrices to capture the cumulative effect of the entire multilayered system. Beforehand, we have to know the configuration, sketched in Fig. 2.4. The cladding layer or can be called the coating layer is the first layer when the incident field illuminated to the stacks and the substrate layer is the last layer of the stacks. The remaining of the stacks then sandwiched by a cladding layer and a substrate layer.

Specifically, when examining the field in the cladding, one must understand it as a composite of both the incident field (F_I) and any field reflected (F_R) from the slab. To do this, since the field in the cladding consists of the incident field and the reflected field from the entire layer stack, the ansatz for the field in the cladding is

$$F_{\text{clad}}(x, z) = e^{ik_x x} \left[F_I e^{ik_{\text{clad},z} z} + F_R e^{ik_{\text{clad},z} z} \right], \tag{2.98}$$

and

$$G_{\text{clad}}(x, z) = i\varrho k_{\text{clad},z} e^{ik_x x} \left[F_I e^{ik_{\text{clad},z} z} - F_R e^{ik_{\text{clad},z} z} \right]. \tag{2.99}$$

The subscript 'clad' means cladding, subscript I and R imply incident wave and reflected wave. Then, we define the ansatz for the field in the slabs as

$$F_{\text{f}}(x, z) = e^{ik_x x} F(z), \tag{2.100}$$

and

$$G_{\text{f}}(x, z) = e^{ik_x x} G(z). \tag{2.101}$$

By using the same way when determining the matrix equation for the single film case, we can find the same matrix equation for the interface between the substrate

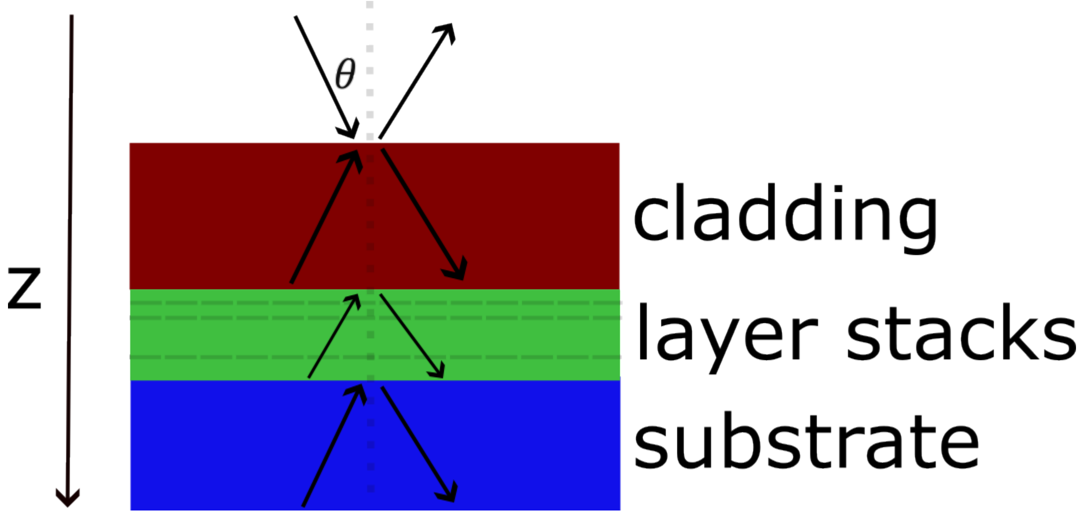

Figure 2.4: A sketch of a multilayer system consisting of stacks of layers that are sandwiched by a cladding or coating layer and a substrate layer. The layer stacks in the figure can indicate one or more layers in the middle of the multilayer. The incoming electromagnetic wave comes from above to the cladding layer with angle of incident θ and the arrows show that the electromagnetic wave can propagates inside the layers in frequent.

and the slabs in Eq. (2.97). However, we have to relate the field in the substrate and the cladding (the region where the transmitted field propagates outside the stratified film) to relate to the final reflectance and the transmittance. Again, we define the ansatz for the field in the substrate in terms of transmitted field (F_T) as

$$F_{\text{subs}}(x,z) = e^{ik_x x} F_T e^{ik_{\text{subs},z}(z-D)}, \tag{2.102}$$

and

$$G_{\text{subs}}(x,z) = i\varrho_{\text{subs}} k_{\text{subs},z} e^{ik_x x} F_T e^{-ik_{\text{subs},z}(z-D)}. \tag{2.103}$$

Combining Eq. (2.98) and Eq. (2.99) with Eq. (2.102) and Eq. (2.103) results in a matrix equation that represents the field in substrate and cladding linked with a transfer matrix $\hat{\mathbf{M}}$,

$$\begin{pmatrix} F(z) \\ G(z) \end{pmatrix}_D = \hat{\mathbf{M}} \begin{pmatrix} F(z) \\ G(z) \end{pmatrix}_0 \quad \Rightarrow \quad \begin{pmatrix} F_T \\ i\varrho k_{\text{clad},z} F_T \end{pmatrix} = \begin{pmatrix} M_{11} & M_{12} \\ M_{21} & M_{22} \end{pmatrix} \begin{pmatrix} F_I + F_R \\ i\varrho k_{\text{clad},z}(F_I - F_R). \end{pmatrix} \tag{2.104}$$

The transfer matrix $\hat{\mathbf{M}}$ connects the fields over an interface through the boundary conditions of Maxwell's equations. This means that we can find the reflected field and transmitted field amplitudes depending on the incident field amplitude by solving the system of coupled equations above as,

$$F_R = \frac{(\varrho_{\text{subs}} k_{\text{subs},z} M_{22} - \varrho_{\text{clad}} k_{\text{clad},z} M_{11}) - i(M_{21} + \varrho_{\text{subs}}\varrho_{\text{clad}} k_{\text{subs},z} k_{\text{clad},z} M_{12})}{(\varrho_{\text{subs}} k_{\text{subs},z} M_{22} + \varrho_{\text{clad}} k_{\text{clad},z} M_{11}) + i(M_{21} - \varrho_{\text{subs}}\varrho_{\text{clad}} k_{\text{subs},z} k_{\text{clad},z} M_{12})} F_I, \tag{2.105}$$

$$F_T = \frac{2\varrho_{\text{subs}} k_{\text{subs},z}(M_{11}M_{22} - M_{12}M_{21})}{(\varrho_{\text{subs}} k_{\text{subs},z} M_{22} + \varrho_{\text{clad}} k_{\text{clad},z} M_{11}) + i(M_{21} - \varrho_{\text{subs}}\varrho_{\text{clad}} k_{\text{subs},z} k_{\text{clad},z} M_{12})} F_I. \tag{2.106}$$

Equation (2.105) and Eq. (2.106) depend on the polarization of the incident field that is considered. For the TE case, the F field is the E field and H field for the TM case. Also, note that the value of $\varrho_{\mathrm{TE}} = 1$ and $\varrho_{\mathrm{TM}} = 1/\epsilon_{\mathrm{layer}}$ are set previously. At last, we can find the reflection and transmission coefficient of the multilayer system. The reflection coefficient r is defined as the ratio of the reflected wave's complex electric field amplitude for TE case and magnetic field amplitude for TM case to that of the incident wave. Similar when finding the reflection coefficient, the transmission coefficient t is the ratio between the transmitted wave to the incident wave,

$$r_{\mathrm{TE,TM}} = \frac{F_R}{F_I}, \tag{2.107}$$

$$t_{\mathrm{TE,TM}} = \frac{F_T}{F_I} \tag{2.108}$$

Finally, we can define the reflectance (R) and the transmittance (T) from the multilayer system illumination. The reflectance is equivalent to the ratio of the power of the reflected wave to the incident wave and the transmittance is equivalent to the ratio of the power of the transmitted wave to the incident wave. We can find the reflectance (R) and the transmittance (T) by the reflection and transmission coefficient,

$$R_{\mathrm{TE,TM}} = \left|r_{\mathrm{TE,TM}}\right|^2 , \tag{2.109}$$

$$T_{\mathrm{TE,TM}} = \frac{\mathrm{Re}|k_{\mathrm{clad},z}|}{k_{\mathrm{subs},z}} \left|t_{\mathrm{TE,TM}}\right|^2 , \tag{2.110}$$

2.9 Summary

In this chapter, we have explained the intricate framework of multiscale modeling employed through this thesis. At its essence, once the physical configurations of a nanoparticle cluster, coupled with its corresponding global T-matrix, are found, we can calculate the scattering properties of a singular layer composed of these clusters. Not stopping there, the further steps involve the deployment of techniques like homogenization and the transfer-matrix method. On the upcoming chapter, we will talk about how we apply the multiscale modeling framework to analyze the nanoparticle-based thin film absorber, approached from both the individual molecular nanoparticle and the bulk nanoparticle perspectives.

3. Nanoparticle-based Multilayer Broadband Absorber

Having covered the theoretical background, we are now ready to use the multiscale modeling to explore the optical functionality of some selected into applications. Our primary focus will be on understanding the optical functionality of the absorber part of a nanoparticle-based thin-film solar thermal collector (STC). This emphasis arises from the multiscale modeling ability to bridge the small dimensions of the nanoparticles with the operational dynamics of a larger scale device through the application of multiscale modeling techniques. By describing into the optical functionality of the absorber, we aim to study how the nanoparticles capability to be the basis of a thin-film absorber, and we demonstrate its potential to have a strong and broadband absorption. We start this chapter by considering Au_{144} molecules as the nanoparticle, and as we progress, our discussion will cover the incorporation of copper nanoparticles into the thin-film absorber. We have complemented the theoretical study with practical fabrication of the absorber. We note that the results presented in this chapter is based on results published in [73, 74, 75].

3.1 The concept of nanoparticle-based solar thermal collector

A solar thermal collector can collect the sunlight because of a particular component within its structure known as the 'absorber'. In nanoparticle-based STCs, multiple processes inside the structure are responsible for the efficient absorption of sunlight and its conversion into heat. A predominant one is plasmonic light trapping that requires densely packed metallic nanoparticles [76]. These nanoparticles not only scatter but also effectively trap sunlight between the nanoparticles gap, enhancing the overall light absorption and making it more efficient. It is helpful to see these nanoparticles as secondary light sources, especially after the initial scattering of incoming light. This results in an increased photon flux between the nanoparticles in the absorber, increasing the likelihood of light being trapped [77]. The intensity of the near-field produced by these nanoparticles is influenced by their characteristics, such as size, shape, and material composition. For instance, optimizing light trapping can be achieved by minimizing the gap between nanoparticles, thereby increasing the cluster's filling fraction. We will explain more about this physical statement by utilizing the concept of plasmonic hybridization in later sections. Furthermore, designing nanoparticles with pronounced features, like nanocylinders and nanocubes, concentrates charges at their edges and corners, allowing us to harness the lightning-rod effect [78, 79], which also contributes to the absorption enhancement.

Another contributing factor is to the overall absorption destructive interference caused by multiple reflections inside the absorber layers. As light waves reflect multiple times within this layers, certain waves can interfere and cancel each other out, thereby minimizing energy losses different than absorption [80]. To minimize these other loss channels, one can design the system so that the thickness of these layers is optimized. The goal is to achieve zero reflection at the interface of the top layer in the thin-film. For this to occur, it is essential that the generalized impedance of the combined thin-film absorber layers aligns or matches with that of air. When this matching is achieved, it ensures minimal reflections and maximizes the amount of light that is absorbed. Of course, not just reflection needs to be minimized but the same holds also for transmission. However, that is usually not a major issue, since transmission can always be suppressed by using a rather metallic film as the terminating layer of the thin-film. When reflection and transmission is suppressed, light can only be dissipated inside the thin-film which implies in the current scenario that heat is generated. It is worthwhile to mentioned that all these properties have to be satisfied in an extended spectral domain, which contributes to the design challenge.

In the following section, we continue with the study of the nanoparticle-based thin-film STCs absorber with two types of scatterers: Au_{144} molecules and copper nanoparticles.

3.2 Thin-film absorber with Au_{144} molecules

In this section, we will discuss metallic molecules as the constituents of a thin-film perfect absorber, specifically focusing on those comprising 144 gold atoms, denoted as Au_{144}. The choice of Au_{144} is not arbitrary. It stands out due to its stability, as affirmed by density functional theory (DFT) energy computations and energy decomposition analysis. Notably, this molecule forms a bridge to the broader realm of gold nanoparticles, which would traditionally be the subject of pure classical electromagnetic simulations, illustrated in Fig. 3.1. The advantage here is the feasibility offered by the multiscale modeling, facilitating the study of phenomena across multiple scales as explained before. As we progress in our discussion, we will demonstrate that the performance of an absorber utilizing Au_{144} molecules is on par with that of gold nanoparticles and it has a promising result. This comparison holds significant implications. It suggests that the modeling of Au_{144} provides a closer alignment with real-world scenarios, particularly since gold nanoparticles, in essence, are assemblies of gold molecules. This analytical approach ensures that we are not only operating in the realm of theoretical constructs but are also anchoring our findings in tangible, practical scenarios.

This study is made possible through the use of time-dependent density functional theory (TD-DFT), which allows for the chemical calculation of a molecule's T-matrix. We note that the TD-DFT calculation is done by Dr. Christof Holzer. TD-DFT is a theoretical framework used in quantum chemistry and condensed matter physics to study the electronic structure and dynamics of molecules, atoms, and solids. It is an extension of density functional theory (DFT), which is primarily used to calculate the ground state electronic structure of systems, by introducing time-dependent perturbation to the system, often in the form of an external electromagnetic field (such as light). This perturbation can excite electrons from the ground state to higher energy states, creating excited states. By solving coupled-perturbed Kohn-Sham

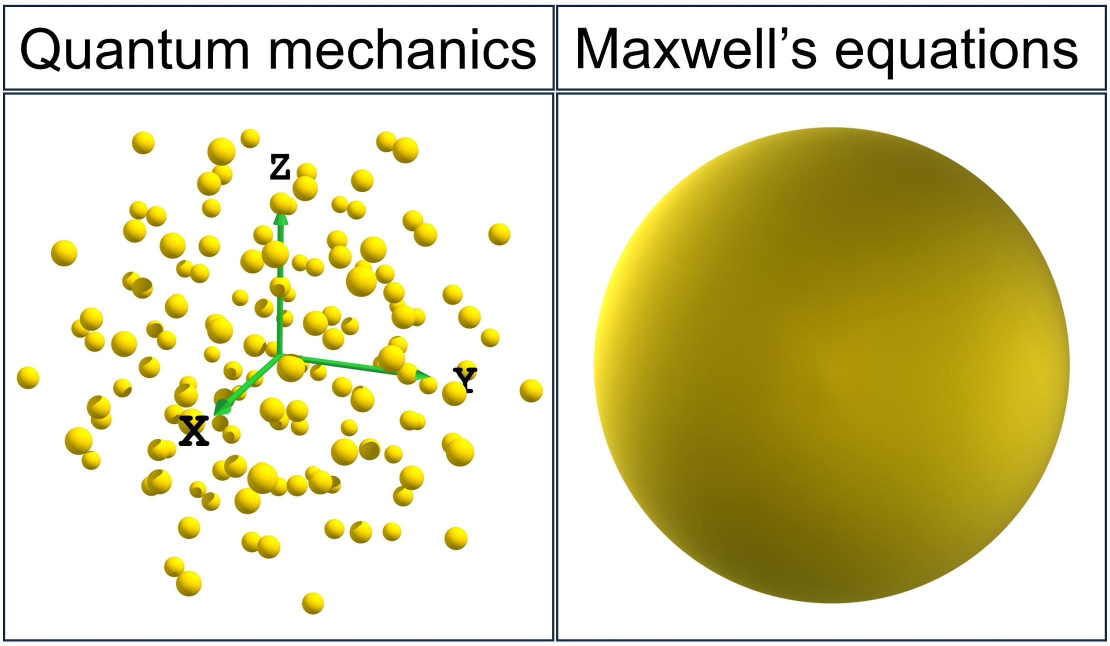

Figure 3.1: Au_{144} molecule that is constructed by the quantum chemical method is approximated with a sphere in the Maxwell equation-type computational method. Adapted from [73].

equations, we can obtain the dipolar electric polarizability tensor from a molecules through the transition density of it in the excited states [81, 82]. The resulting transition density outlines the average charge motion away from the atoms in this band.

The T-matrix calculation is done by Turbomole program. In our case, we calculate the T-matrix from a stable Au_{144}. The radius equal to 0.7516 nm. Figure 3.2 shows its transition density.

3.2.1 Application of the multiscale modelling

We now employ the molecular T-matrix obtained through TD-DFT simulations to describe the optical properties of a realistic macroscopic device. We specifically focus on the characteristics of Au_{144} gold molecules, which are considered as the nanoparticles embedded within the thin-film absorber. Using Eq. 3.1, we can calculate the T-matrix in dipole approximation for this molecule linked to the molecule's electric polarizability tensor, which measures the induced electric dipole moment in response to an external electric field. Please note, we consider here only the electric dipolar polarizability, since this is the only term that has a nonvanishing contribution. Electromagnetic coupling terms are not important because of the quasispherical symmetry of the considered object, and magnetic dipole moments or even higher-order multipole moments are too weakly excited. Further, Fernandez-Corbaton *et al.* [83] have derived a one-to-one relationship between the electric polarizability tensor $\underline{\underline{\boldsymbol{\alpha}}}$ as expressed in Cartesian coordinates and the T-matrix $\underline{\underline{\mathbf{T}}}$ of

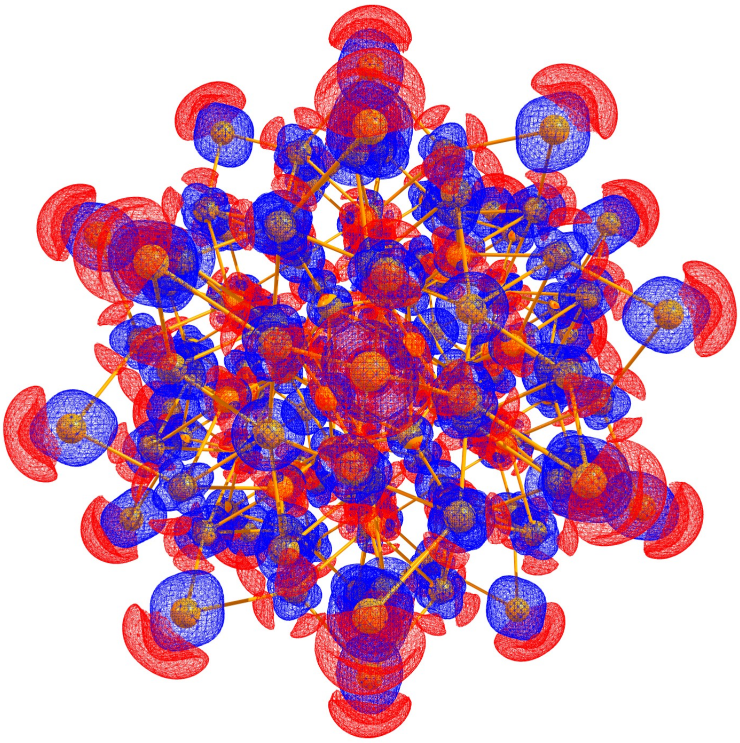

Figure 3.2: Transition density at the plasmonic peak ($\lambda = 460$ nm) of the Au_{144} generated from the polarizabilities from 2.0 to 2.5 eV. An isovalue of 0.00015 a.u. was used. Adapted from [73].

a molecule. This relationship is expressed as

$$\underline{\underline{\mathbf{T}}} = -\frac{Zk^3c}{6\pi i}\underline{\underline{\mathbf{M}}}\left(\underline{\underline{\boldsymbol{\alpha}}}\right)\underline{\underline{\mathbf{M}}}^{-1}, \quad \underline{\underline{\mathbf{M}}} = \begin{pmatrix} \frac{1}{\sqrt{2}} & \frac{i}{\sqrt{2}} & 0 \\ 0 & 0 & 1 \\ -\frac{1}{\sqrt{2}} & \frac{i}{\sqrt{2}} & 0 \end{pmatrix}^{-1}, \tag{3.1}$$

where Z is the wave impedance, k is the wavenumber of the background medium, c is the speed of light, and the matrix $\underline{\underline{\mathbf{M}}}$ is the transformation matrix from a Cartesian to spherical basis since we are dealing with further formulations in spherical coordinate. Equation (3.1) is derived by considering that the dipolar incident Mie coefficients $a_{\alpha,n,m}$ are proportional to the incident electromagnetic wave at the origin in spherical coordinates. We apply then Eq. (3.1) to express the Au_{144} molecule T-matrix that is obtained through TD-DFT. Figure (3.3) depicts the electric polarizability of the Au_{144} molecule in vacuum and silica (SiO_2) background. The electric polarizability of the metallic molecule in vacuum (blue line in Fig. (3.3)) indicates that the Au_{144} nanoparticle possesses two pronounced maxima peaks that can lead to localized surface plasmon resonance (LSPR) at $\lambda = 460$ nm and $\lambda = 565$ nm. When the Au_{144} molecule is placed in a vacuum, its electric polarizability is solely determined by the intrinsic properties of the nanoparticle itself. However, when the gold nanoparticle is embedded in a SiO_2 matrix, the two maxima peaks are still evident but exhibit a slight shift to lower energies and an increase in magnitude. This suggests that the SiO_2 matrix has the ability to enhance the strength of the LSPR generated by the induced electric dipole within the nanoparticle. Such a redshift of the LSPR resonance is fully inline with the phenomenological description that we have developed in subsection

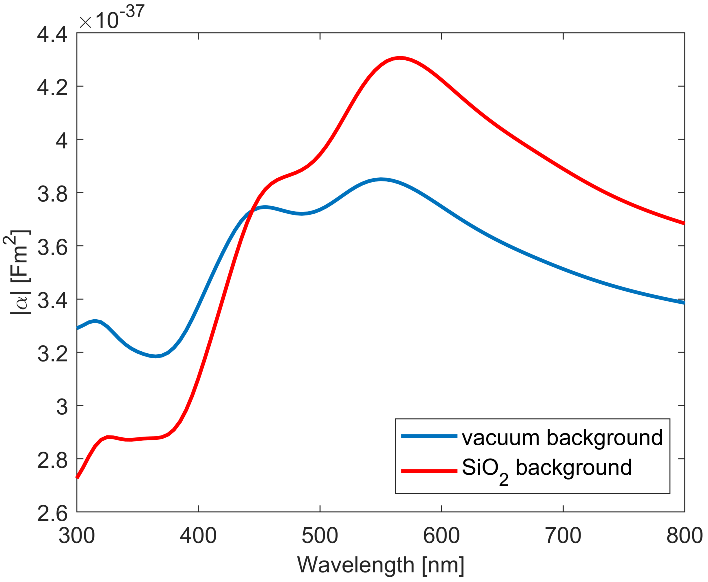

Figure 3.3: Magnitude of the electric dipolar polarizability of an Au_{144} nanoparticle in air and SiO_2. Adapted from [73].

2.3.2. When describing the LSPR of a small metallic nanoparticle, we have seen that an increase in the permittivity of the background material forces the LSPR to occur at a wavelength where the permittivity takes more negative values. When considering the metal to be described with a Drude type material dispersion, this more negative permittivity occurs at smaller frequencies so at longer wavelengths. And it is that change in the resonance wavelength that we even see to emerge at the level of a TD-DFT simulation.

As a next step, we wanted to describe the response from a larger cluster of such metallic molecules that we consider later as one unit cell that is periodically arranged to study the reflection and transmission from a thin-film. For that purpose, we assembled 500 Au_{144} molecules into a cubic unit cell with a side length of 12.5 nm utilizing the force-biased algorithm. Figure 3.4 illustrates an exemplarily cluster of these molecules with a filling fraction of 45%. Advancing in our multiscale modeling approach, we determined the global T-matrix for this cluster. Given that all molecules in the cluster are identical, it is much easier and faster to compute the cluster's global T-matrix only with a T-matrix of single gold molecule. After having computed the T-matrix of the cluster of metallic molecules in a local formulation, translation operations are performed to obtain the global T-matrix for the entire cluster. Utilizing this global T-matrix, we computed the absorption cross-section of the molecules cluster. Figure 3.5 shows the absorption cross-section of a single Au_{144} molecule and a configuration of 101 densely packed Au_{144} molecules embedded in a silica matrix. For comparison, we also show the absorption cross-sectioon of a single gold nanoparticles with nominal the same radius as the Au_{144} molecule and a configuration of 101 gold nanospheres embedded in the same background medium. When treating them at the level of a gold nanosphere, the polarizability was expressed purely on classical grounds. This comparison aims to ascertain the optical interactions, if any, between the molecules when closely packed. To be specific, the T-matrix of this particular single gold nanosphere is calculated analytically through Eq. (2.47), and the cluster of 101 gold nanospheres are generated in full agreement with the cluster made from

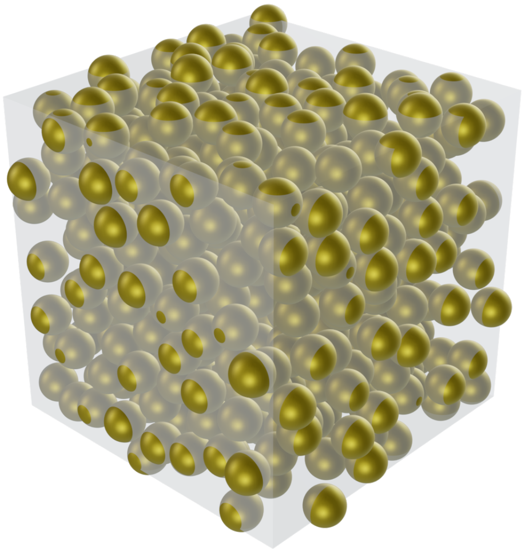

Figure 3.4: Cubical unit cell for a cluster containing 500 metallic molecules classically described as small metallic nanoparticles. Adapted from [73].

with the Au_{144} molecules. Note that we use the Johnson-Christy experimental gold permittivity [45] with size effect added for the gold nanosphere calculation.

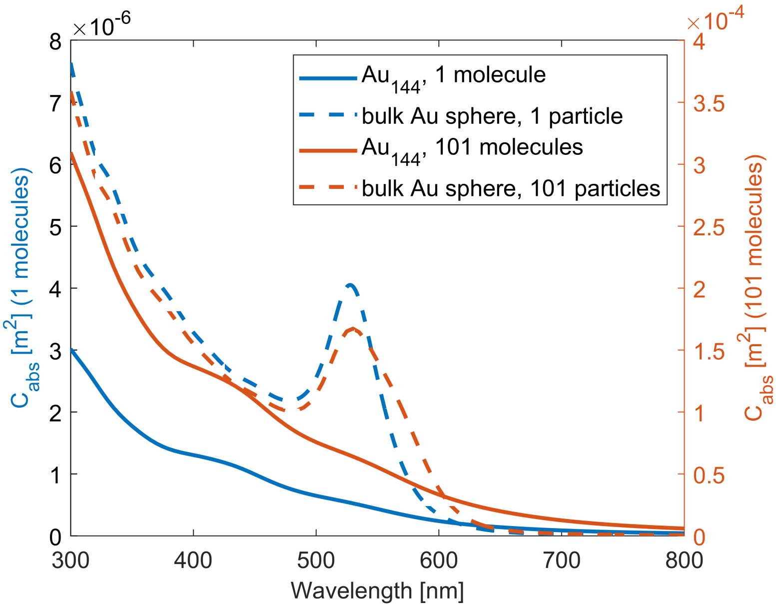

Figure 3.5: The absorption cross-section from a single Au_{144} molecule (solid line, left y-axis), a single Au nanosphere (dashed line, left y-axis), a cluster comprising 101 Au_{144} molecules (solid line, right y-axis), and a cluster comprising 101 Au nanospheres (dashed line, right y-axis).

The interaction between the gold molecules in a unit cell does not introduce new resonance peaks in the visible light spectrum. It also applies to the gold nanospheres. Drawing upon the principles of plasmon hybridization theory, the induced electric dipoles between the gold molecules are neither completely in-phase nor out-of-phase.

As a result, the antibonding mode typically seen at shorter wavelengths is absent in this scenario. A distinct resonance peak for an individual gold nanosphere is identified at $\lambda = 526$ nm, corresponding to the localized surface plasmon resonance (LSPR) of that specific nanosphere. In contrast to this, the absorption cross-section for the gold molecule does exhibit a barely pronounced weak resonance peak. The weak resonance can be attributed to the longer atomic spacing within the gold molecule compared to a gold nanosphere of the same dimensions, leading to less of probability of electrons interact to each other in the molecule, so that causing lack of resonance for the molecule. Also, the quantum simulation is unable to compute the plasmonic interactions from the molecule electron gas correctly. The molecules of that small size cannot be treated on the base of classical Maxwell's equations where the material properties are captured with a dielectric function. So that, the discrete nature of the transitions that we still observed in the polarizability clear speaks against such a treatment of the Au_{144} molecule at the level of a continua. Furthermore, the absorption magnitude intensifies with the inclusion of more gold molecules or nanospheres. This is not just a result of increased quantities leading to a higher probability of absorption, but also due to the fact that gold molecules tend to weakly interact with one another, primarily through van der Waals forces. Given the minuscule size of these particles, scattering effects are minimal, effectively ruling out any significant radiative interaction among them. These findings align well with established physical theories and expectations. Importantly, throughout our study, we have thoroughly considered and incorporated the effects of these interactions in our modeling and analysis.

We continue the multiscale modeling by creating a layer that is periodically and infinitely arranged in two dimensions. In our case, a layer consisting of Au_{144} molecules in silica matrix cluster is build. The thickness equal to the lattice constant of the cluster unit cell, which is $d = 12.5$ nm. Substrate and cladding consists of a vacuum. Then, we can calculate the reflection coefficient and the transmission coefficient of this layer through the previously described Q-matrix method. This allow us to find the effective electric permittivity of this layer by s-parameter retrieval method in form of Eq. (2.79). We can retrieve the effective magnetic permeability as well. However, it is negligibly dispersive relative to the vacuum permeability because the Au_{144} molecule is nonmagnetic. We also want to study the optical response when considering thin-films with different thicknesses. For this purpose, we consider layers comprising of the Au_{144} molecules layer stacked to each other. We consider that the thin-film will have 1, 2, and 4 layers as a stack. This means that the thickness of each stack equal to $d = \{12.5, 12.5 \cdot 2, 12.5 \cdot 4\}$ nm. Figure 3.6 presents the effective relative electric permittivity of the Au_{144} molecules thin-film stacks that was retrived from the respective complex reflection and transmission coefficients. We observe that the real and imaginary components of the effective relative electric permittivity for both a single stack and multiple stacks are nearly identical. This suggests that the permittivity is not dependent on the thickness of the layer, classifying this layer as homogeneous. Consequently, the effective permittivity retrieval algorithm appears to be working correctly. Additionally, two peaks are noticeable in the real component of the permittivity curve. These peaks correspond to wavelengths that bear resemblance to the electric polarizability curve presented in Fig. 3.3. This observation holds true for the peak of the imaginary component of the electric polarizability at a wavelength of 635 nm. Furthermore, the curve of the real part displays an increase

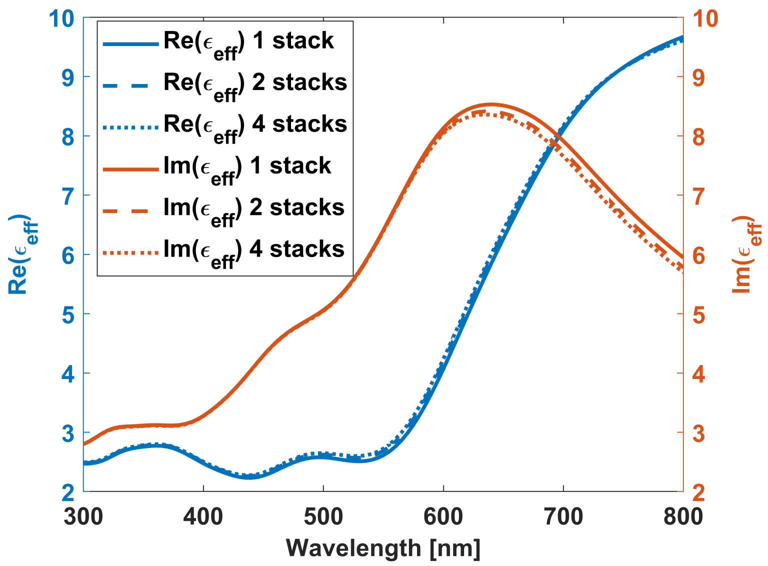

Figure 3.6: Real and imaginary part of the effective relative electric permittivity of the Au_{144} nanoparticles in SiO_2 matrix thin-film stacks. Adapted from [73].

and subsequently starts to decay at longer wavelengths. This behavior is reminiscent of the real part of the Lorentz oscillator permittivity model, a modification of the Drude permittivity model. The Lorentz models consider that there is a virtual spring that bound an electron with an another electron. Causing Eq. (2.24) has additional term with Lorentz oscillation frequency (ω_0), stated in Eq. 3.2,

$$\epsilon(\omega) = \epsilon_0 \left(1 + \frac{\omega_{\mathbf{p}}^{\mathbf{2}}}{\omega_0^2 - \omega^2 - i\gamma\omega}\right). \tag{3.2}$$

Now, since we have the effective relative electric permittivity of a thin-fim made from densely packed Au_{144} molecules, we can use that to optimize a multilayer system to act as a broadband perfect absorber. This multilayer system is a thin-film system where the Au_{144} molecule layer discussed previously with thickness d_{np} is deposited on top of a pure SiO_2 matrix spacer layer with thickness d_{spacer} and a very large thick gold mirror, illustrated in Fig. 3.7. We exploit the concept of multiple reflections within the spacer layer, facilitated by the gold mirror. The design in Fig. 3.7 is intended to ensure that the final reflected outgoing wave at the interface of the Au_{144} molecule layer and vacuum is effectively vanishing due to destructive interference. Moreover, when light penetrates the Au_{144} molecule layer, it may be absorbed by the Au_{144} molecules. Consequently, the design of this device is proposed to achieve a broad and strong absorption of the incident electromagnetic waves across a wide spectrum. We consider light illumination in normal incidence with wavelength in visible light spectrum, which ranges from $\lambda = 300$ nm to $\lambda = 800$ nm. We want to maximize the objective function in Eq. 3.3, over the area τ, normalized below the absorption curve, so that has a quantity between 0 and 1.

$$f_{\text{ob}}(d_{\text{np}}, d_{\text{spacer}}) = \frac{\int_{\lambda=300\text{ nm}}^{\lambda=800\text{ nm}} \tau(d_{\text{np}}, d_{\text{spacer}})\, d\lambda}{\int_{\lambda=300\text{ nm}}^{\lambda=800\text{ nm}} d\lambda}, \tag{3.3}$$

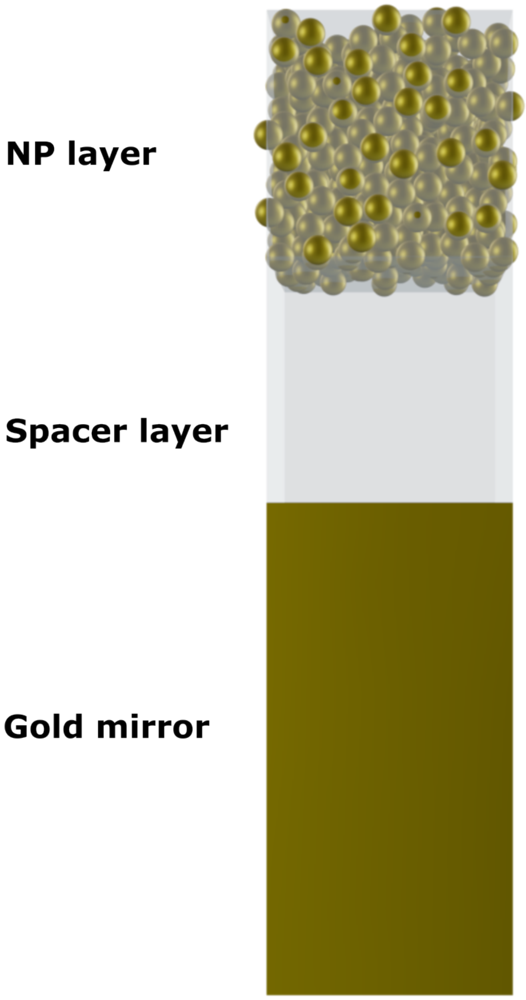

Figure 3.7: Scheme of the considered multilayer thin-film system. Adapted from [73].

We seek to optimize the objective function by pinpointing the ideal thickness for both the Au_{144} molecules and spacer layers. To accomplish this, we evaluate the reflectance (R), transmittance (T), and absorptance (A) of the absorber utilizing the classical thin-film transfer matrix method. This methodology presents a significant speed advantage for calculations over the Q-matrix method, particularly when considering many wavelengths. For each variation in layer thickness within the range $d_{\text{np}} = 0 - 100$ nm and $d_{\text{spacer}} = 0 - 100$ nm, we compute the absorptance area τ. The resulting colormap is presented in Fig. 3.8(a). There is a noticeable region of the optimal layer thicknesses, which is highlighted with a blue ring in Fig. 3.8(a). The optimal thicknesses are determined to be around $d_{\text{np}} = 15$ nm and $d_{\text{spacer}} = 39$ nm. To further validate these findings, we show the reflectance (R), transmittance (T), and absorptance (A) of the absorber in relation to the specified film thicknesses against wavelength, as depicted in Fig. 3.8(b). Remarkably, approximately 97% of the absorption curve is encapsulated beneath the absorption curve, indicating that nearly the entirety of light in the visible spectrum is absorbed by the device. Additionally, we predict that the overall response gets weaker at infrared wavelength. This is not surprising considering the weaker plasmonic response of the metallic molecules at these wavelengths. Additionally,

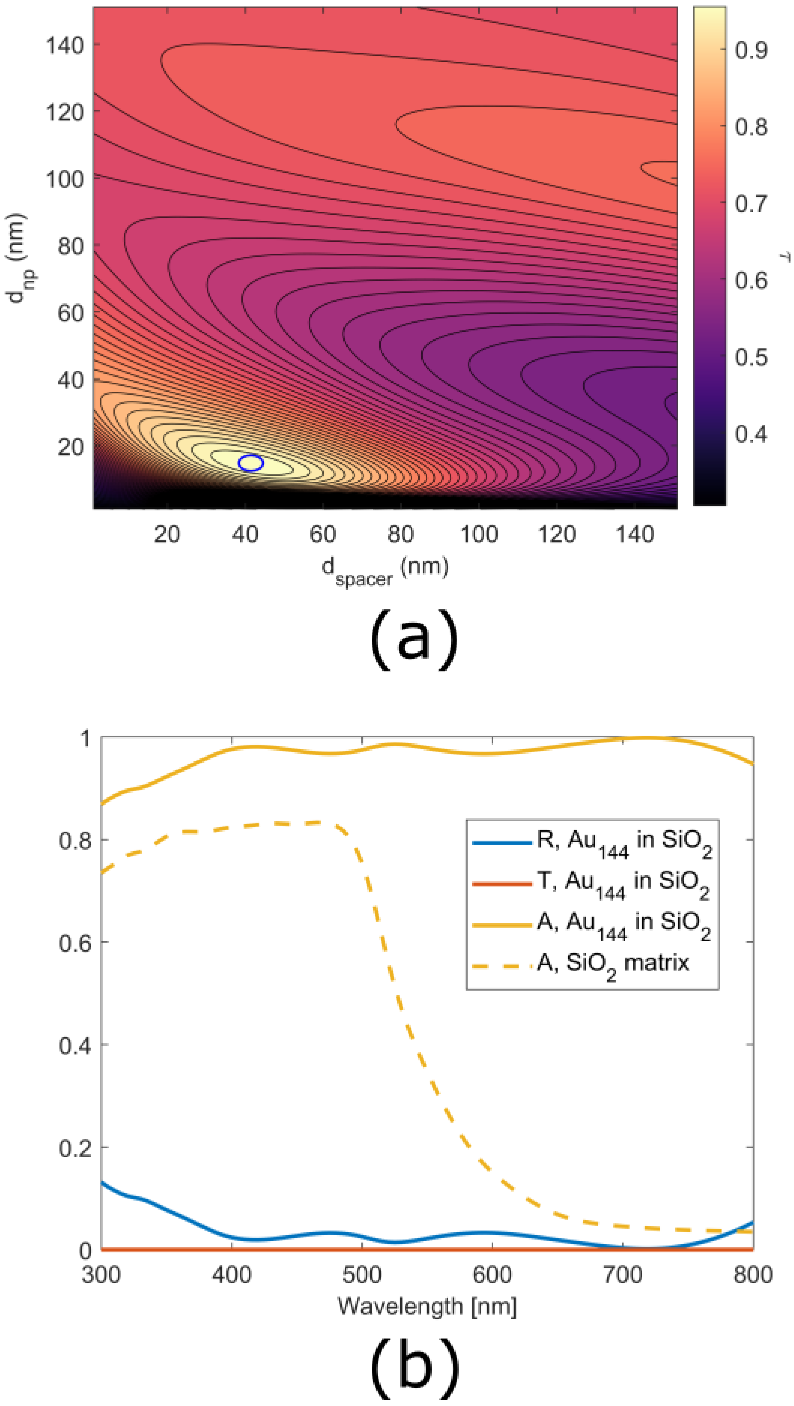

Figure 3.8: (a) The integrated absorption of perfect absorbers containing Au_{144} molecules and a silica spacer layer on top of a gold substrate as a function of the thicknesses of the involved layer of Au_{144} molecules thin-film and dielectric spacer layer thicknesses. A blue ring points to the optimal nanoparticle layer and spacer layer thickness where the total absorption is maximized. (b) Wavelength dependent reflectance, transmittance, and absorptance for the optimal thin-film layers thicknesses. The absorptance of a referential structure consisting of a silica layer on top of a gold substrate is also shown for comparison. Adapted from [73].

we analyzed the absorptance curve of the absorber without the inclusion of Au_{144} molecules. For the thin-film lacking of the Au_{144} molecules, the absorption curve begins to attenuate starting from a wavelength of approximately 500 nm. This observation suggests that the molecular/nanoparticles interactions play a significant role at wavelengths exceeding 500 nm, while the absorption at shorter wavelengths is predominantly driven by the destructive interference effect. Consequently, by carefully engineering the interactions between nanoparticles within the thin-film, there is potential to enhance and optimize absorptance at these higher wavelengths.

In conclusion, we have successfully engineered a broadband perfect absorber in the visible light domain using Au_{144} molecules as the foundation of the absorber.

3.3 Thin-film broadband absorber with copper nanoparticles

We have proposed a broadband thin-film absorber that is based on Au_{144} molecules. This absorber has showcased a broadband and rather strong absorption capabilities within the visible light spectrum. As our research progresses, we are exploring the potential of absorbers using metallic nanoparticles, specifically copper (Cu) nanoparticles. Historically, noble metals such as gold (Au) and silver (Ag) have been preferred in plasmonic absorbers because of their outstanding low-loss plasmonic properties [84, 85, 86]. However, the limited availability of both silver and, in particular, gold, combined with their high material costs, makes gold nanoparticle-based absorbers economically challenging. Based on that concern, we study the feasibility of absorbers constructed from more economical and readily available materials, such as copper nanoparticles combined with an alumina (Al_2O_3) dielectric. Notably, the performance of copper nanoparticles can compete with that of silver and gold, especially when the particles are non-spherical [87]. Furthermore, the natural color of copper, which arises from its particle composition, correlates directly with the wavelength of its plasmon resonance peak. In comparison to gold and silver, the plasmon resonance peaks of copper occur at longer wavelengths [88]. This means that it is advantageous as it broadens the absorption spectrum, while absorption at shorter wavelengths is achieved through the multiple reflection effect within the multilayer system, as detailed in the previous section. Moreover, while Cu offers performance that might be comparable to Ag and Au, it has a noticeable tendency to oxidize [89], which can significantly impair the plasmonic response of the nanoparticles. Fortunately, oxidation can be mitigated by applying ultra-thin protective coatings [90] or by treating the nanoparticles with corrosion inhibitors [91].

In this section, we undertake an experimental effort to realize the optimal configuration of a copper nanoparticles based thin-film broadband absorber taken from predictions obtained with our multiscale modeling technique, leading to the subsequent fabrication of the selected thin film. We observe that the fabrication and the characterization of the copper nanoparticle layer is carried out exclusively by the research group led by Prof. Franz Faupel at Kiel University. Their group possesses the expertise to fabricate absorber samples using two different techniques, namely the gas aggregation source (GAS) [74, 92] and simultaneous co-sputtering method [75]. In the gas aggregation source method, the sample is fabricated inn a RF magnetron sputtering system with an alumina target and a separately attached custom-built gas aggregation source. Then, as comparison, in the co-sputtering method, the absorber is fabricated via a magnetron sputter deposition technique in a custom-built high vacuum deposition system. This method has two separate sources to deposit Cu nanoparticles and an alumina matrix onto the thin-film surface.

Then, we explore initially the impact of several degrees of freedom on the performance of the device and conclude on promising samples that shall be realized and characterized. We then compared the results obtained with the different absorber fabrication techniques to simulations. Further, we extend the study from absorber characterized by a single layer containing nanoparticles with a certain filling fraction (FF), referred to as a single-nanocomposite layer, to samples that contain a stack of more than one copper nanocomposite layer featuring different filling fractions. This configuration is termed a multi-nanocomposite layer. Our findings reveal that the multi-nanocomposite absorber demonstrates better absorption capabilities in comparison to its single-nanocomposite counterpart.

We start by packing a cluster of nanoparticles in a unit cell. The size distributions of the nanoparticles is taken according to an absorber sample fabricated through gas aggregation source technique, shown in Fig. 3.9. This reduces the number of nanoparticles in the simulations, which simplifies the computations, while the approximated experimental size distribution is preserved. Then, as well, we use the same approach for determining the absorptance of the copper nanoparticle thin-film absorber as with the Au_{144} in the previous section. The same formalism was applied until the calculation of the absorptance by the transfer matrix method, where the thin-film optimization starts. We mention that the experimental copper permittivity data by Johnson-Christy [45] and alumina permitivity data by Boidin [93] are used in the computation. Also, we assume that the T-matrices of the copper nanoparticles have up to eighth multipolar order. We consider the absorber configuration analogous to the Au_{144} absorber, with that the Au_{144} molecules are substituted with copper nanoparticles in alumina matrix, the spacer layer is considered as pure alumina matrix and the copper mirror is used as the substrate, illustrated in Fig. 3.7. Note

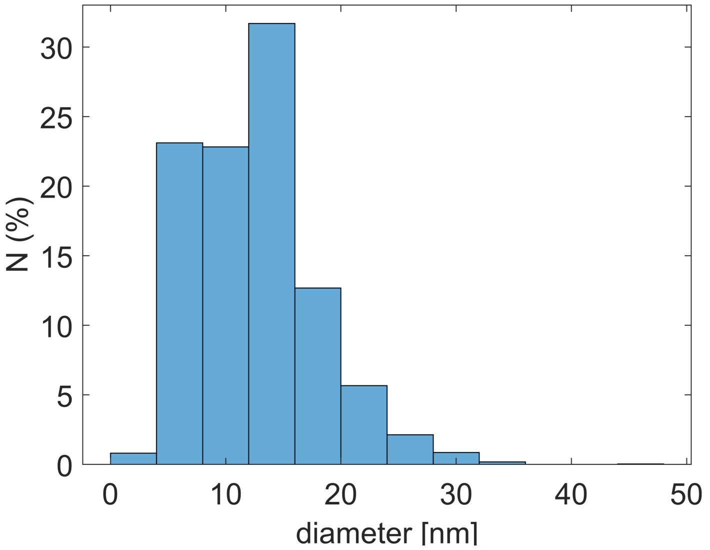

Figure 3.9: Nanoparticles size distribution for FF = 33.0% as measured. Adapted from [74].

that, we use the size-corrected copper permittivity in Eq. (2.26) since the sizes of the nanoparticles are very small but not too small to require a description at the level of a TD-DFT.

We can take an early guess about the effect of the nanoparticle filling fraction on the absorption by the thin-film absorber by plotting the effective permittivity across the relevant spectral domain from 250 nm until 1800 nm of the copper nanoparticle using the s-parameter retrieval method, shown in Fig. 3.10. It is shown that there are two noticeable peaks seen at around 800 nm and 1000 nm induced through the antibonding mode resulting from the hybridization of plasmons from interacting nanoparticles in the layer. Meanwhile, a weaker peak around 600 nm is linked to the intrinsic localized surface plasmon resonance peak for a single copper nanoparticle, redshifting along a larger filling fraction. The real and imaginary parts of the effective permittivity peaks also tend to move to longer wavelengths or redshift and the magnitude of the effective permittivity is larger, especially in lower energy, as the filling fraction is higher. This is good for absorber application because we can say that the thin film with a high filling fraction of copper nanoparticles results in broadband and strong absorption.

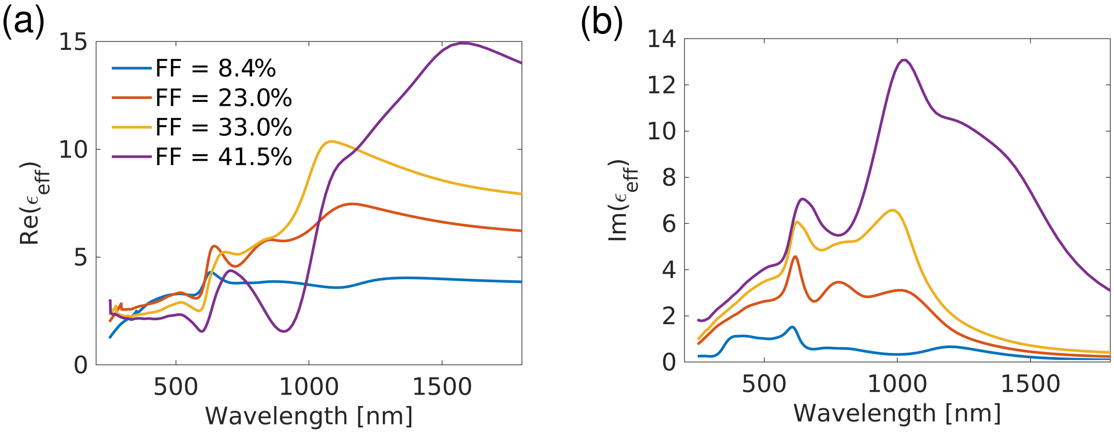

Figure 3.10: (a) Real and (b) imaginary part of the effective permittivity of thin-films made from copper nanoparticles for different filling fractions in the spectral range from $\lambda = 250 - 1800$ nm. Adapted from [74].

Next, we want to know the effect of the angle of incidence on the absorber. Transverse magnetic (TM) polarization light is considered with oblique incidence, while its angle is varied from $\theta = 0 - 80°$. Figure 3.11 displays the integrated absorptance with respect to the angle of incidence. From the figure, we can tell that there is an optimal angle, around 60 degrees for all of the filling fraction variation, which is coincidentally connected to Brewster's angle, that can cause the reflection to go to zero and hence maximize the absorption. So then, we consider the optimal angle of incidence to be $\theta = 60°$ later be used in this thesis.

We start to optimize the thin film by finding the optimal thicknesses of the thin film, the nanoparticle layer thickness (d_{np}) and the dielectric spacer layer (d_{spacer}). We sweep the d_{np} and d_{spacer} from 0 to 150 nm and the integrated absorptance spectra is calculated for all of the thicknesses possibility with the optimal angle determined before. The colormap depicted in Fig. 3.12 shows the contours of the integrated

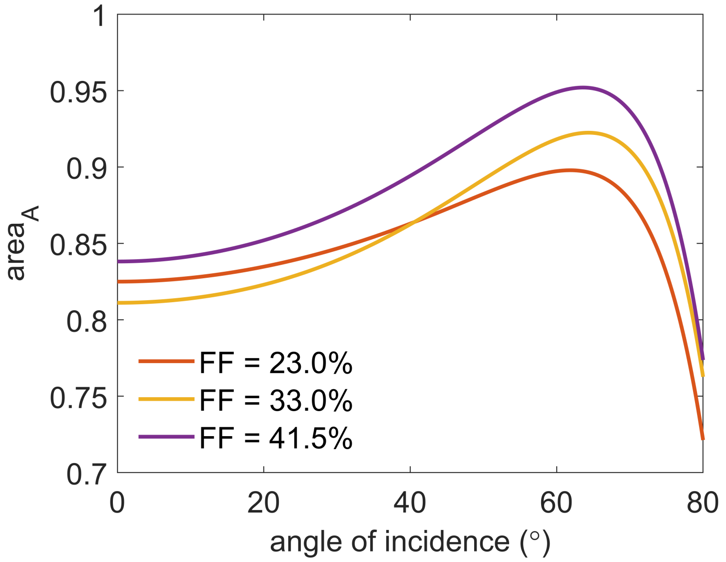

Figure 3.11: Normalized area of absorptance as a function of the incidence angle for a TM polarized plane wave illumination and as a function of the filling fraction. Adapted from [74].

absorptance as a variation of the nanoparticle layer and spacer layer thickness for filling fraction variation, calculated at normal and oblique incidence. From the

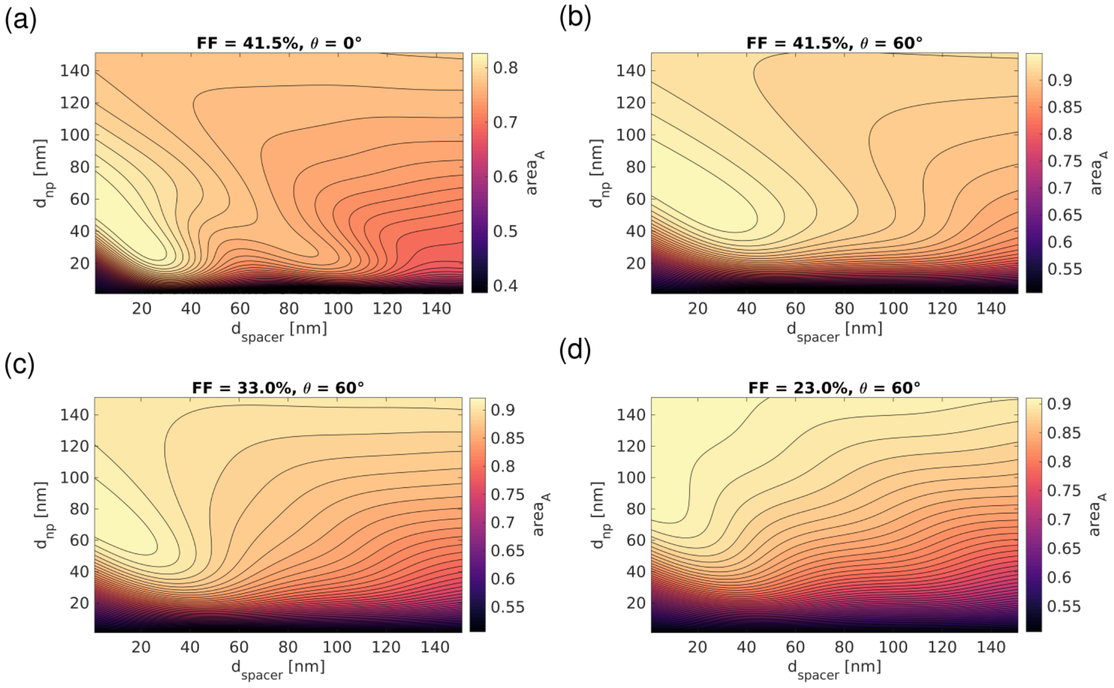

Figure 3.12: The normalized area of absorptance in the broadband perfect absorber containing Cu nanoparticles at incidence angle (a) $\theta = 0°$ and (b) $\theta = 60°$ for 41.5% filling fraction (FF) as a function of the layer thickness and the thickness of the spacer layer. Comparison to lower filling factor for (c) FF = 33.0% and (d) FF = 23.0% at $\theta = 60°$ are also depicted. Adapted from [74].

figure, it is observed that there exist specific optimal d_{np} and d_{spacer} for thin films, which are distinctly highlighted in the contour colormaps as the brightest regions. These optimal thicknesses ensure that the thin film absorber is capable of efficiently absorbing more than 80% of incident light energy. Remarkably, the optimal thin film exhibits a remarkable ability to absorb a broad spectrum of light, demonstrating strong absorption characteristics even when its thickness is kept relatively thin, typically below 100 nm. For proving this, we plot the absorptance of a thin film absorber with optimal d_{np} and d_{spacer} according to the colormap in Fig. 3.12(b), in form of Fig. 3.13. As depicted in Fig. 3.13, the thin film absorber with a 41.5% filling fraction demonstrates almost perfect light absorption capabilities, across a wide spectral range encompassing the ultraviolet to the near-infrared regions. Even, thin film absorbers with lower filling fractions show integrated absorptance exceeding 90%. Furthermore, an oscillatory pattern emerges in the absorptance data, which can be attributed to the phenomenon of Fabry-Perot resonance. In this context, denser nanoparticles effectively nullifies reflection inside the layers, thereby yielding enhanced absorption across an extended spectral region. These observations lead us to a compelling conclusion: the filling fraction of nanoparticles employ an important aspect in designing the nanoparticle-based thin-film absorber. For optimal design of a thin-film-based perfect absorber, a higher nanoparticle filling fraction is advisable. Yet, it is worth noting that determining the optimal absorber layer thicknesses for maximizing absorption is not trivial, it calls for further study in future research efforts.

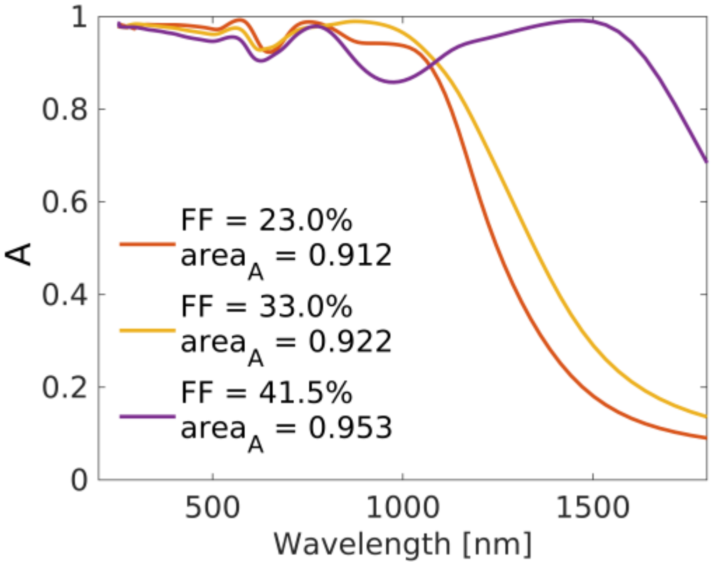

Figure 3.13: Absorptance in a few selected examples where the thicknesses of the layers has been chosen at $d_{\mathrm{np}} = 80$ nm, $d_{\mathrm{spacer}} = 13$ nm. The absorptance is shown for three different filling fractions previously considered. The angles of incidence are chosen to be $\theta = 60°$. Adapted from [74].

Further, we apply the optimal thin film absorber thickness to the experimental fabrication with gas aggregation source method and compare the absorptance obtained through simulation and experiment. For this reason, we consider the thin filn absorber with the 114 nm nanoparticle layer thickness for 33.0% nanoparticle filling fraction and 105 nm nanoparticle layer thickness for 41.5% filling fraction with the alumina spacer layer thickness is consistent to 20 nm, shown in Fig. 3.14. There is an apparent discrepancy between the simulation and experimental absorptance curves, according to Fig. 3.14. The experimentally measured absorptance is weaker than that simulated, though the prominant peaks can be correlated to each other, illustrated by the arrows in the figure. This discrepancy can be attributed to the gas aggregation source-derived absorber's inhomogeneity in thickness, which results from touching particles and the aggregation of nanoislands within the nanocomposite layer, seen in Fig. 3.15(a). Figure 3.15(a) shows an SEM micrograph capturing the thin-film absorber consisting copper nanoparticles on a silicon wafer after a deposition duration of 30 seconds. Agglomerated nanoparticles or nanoislands, which are of particular interest, have been highlighted using red circles in the figure. Based on our analysis, we predict that nanoparticles in touch likely do not exhibit electromagnetic coupling. Further, to evaluate the impact of closely spaced nanoparticles on the observable characteristics, we show in Fig. 3.15(b) an example that compares the absorption cross section of a pair of touching nanoparticles (gap distance = 0 nm) to a pair of only nearly touching nanoparticles (gap distance = 1 nm). It can clearly by seen that a non-touching copper dimer can have a higher absorption cross-section in general, except at wavelength above 900 nm. The absorption at these longer wavelength can be made stronger when more than two particles interact, leading to a pronounced of coupling due to plasmonic hybridization, as we have already discussed in the previous section. So, we can say that touching particles decrease the performance of the absorber because the light trapping potential between the particles can be lost. This reduces the likelihood of plasmonic interactions between the nanoparticles and give a roughened surface to the layer according to Fig. 3.15(c). Figure 3.15(c) is an AFM topography taken on top of the thin-film absorber surface. It seems like there is a flucuative of roughness shows by a significant difference of surface roughness amplitude. This is due that large-sized nanoparticles that creating the roughness caused by small surface diffusion at the absorber surface. Such a surface,

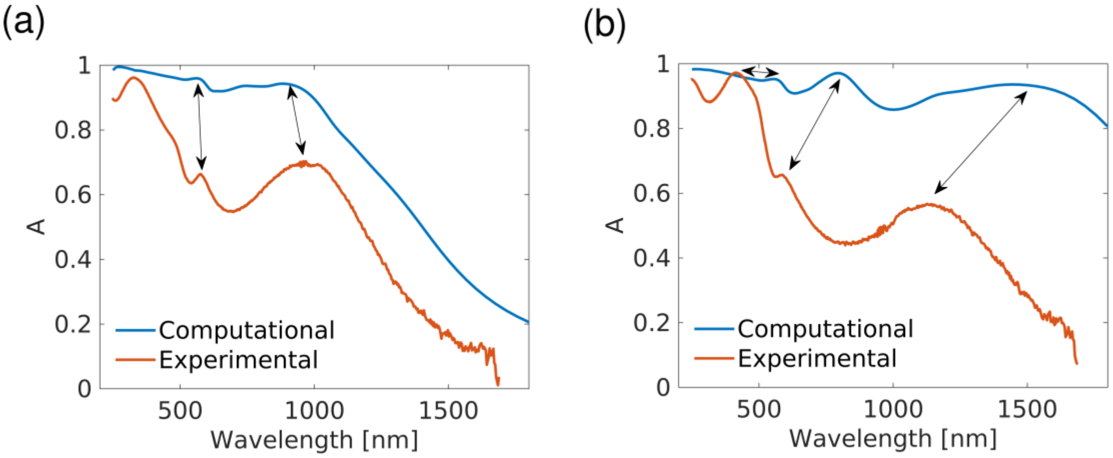

Figure 3.14: Comparison of the simulation and experimental absorptance curves for two selected samples characterized by (a) FF $= 33.0\%, d_{\mathrm{np}} = 114$ nm and (b) FF $= 41.5\%, d_{\mathrm{np}} = 105$ nm at $d_{\mathrm{spacer}} = 20$ nm and for an incidence angle of $\theta = 60°$. The arrows act as a guide to the eye to highlight similar features between the experimental and numerical results. Adapted from [74].

in turn, leads to increased outward reflection, which is unfavorable to the absorber's performance.

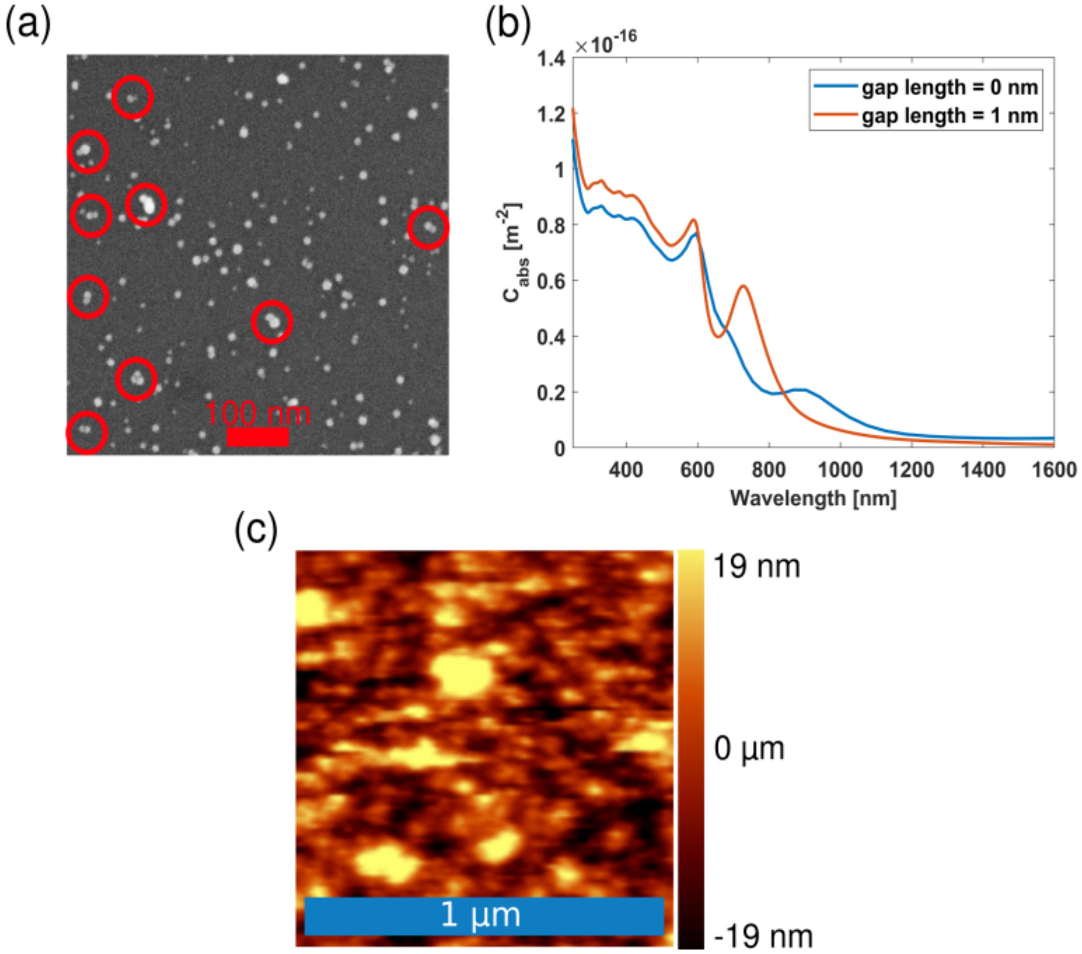

Figure 3.15: (a) SEM picture after 30 s of copper nanoparticle deposition onto Si substrate. It is well visible that some nanoparticles are in touch with others. Some of them are marked with blue circles. (b) Absorption cross-section of touching and non-touching (gap separation = 1 nm) 5 nm radius copper dimer in alumina. (c) AFM topography color plot of an exemplary absorber layer structure with a total thickness of 47.1 nm is shown. The difference between the hills and valleys is 38 nm. This proves that the surface roughness can partially cause deviations between simulations and experiments. Adapted from [74].

We now try to compare the performance of the thin film absorber based on gas aggregation source and co-sputtering method. We start by considering size distributions shown in Fig. 3.16(a) and Fig. 3.16(b), respectively. The size distributions are considered in the simulations to reproduce the details of the experimental size distribution. That should allow us to make simulations close to what is experimentally possible. The clusters in the simulations are formed from 100 nanoparticles with FF = 33% for the gas aggregation source method and 115 nanoparticles with FF = 32% for the co-sputtering method.

Going into the absorptance calculation by the transfer matrix, we consider that, since the unpolarized light is used as the incident light in the experimental

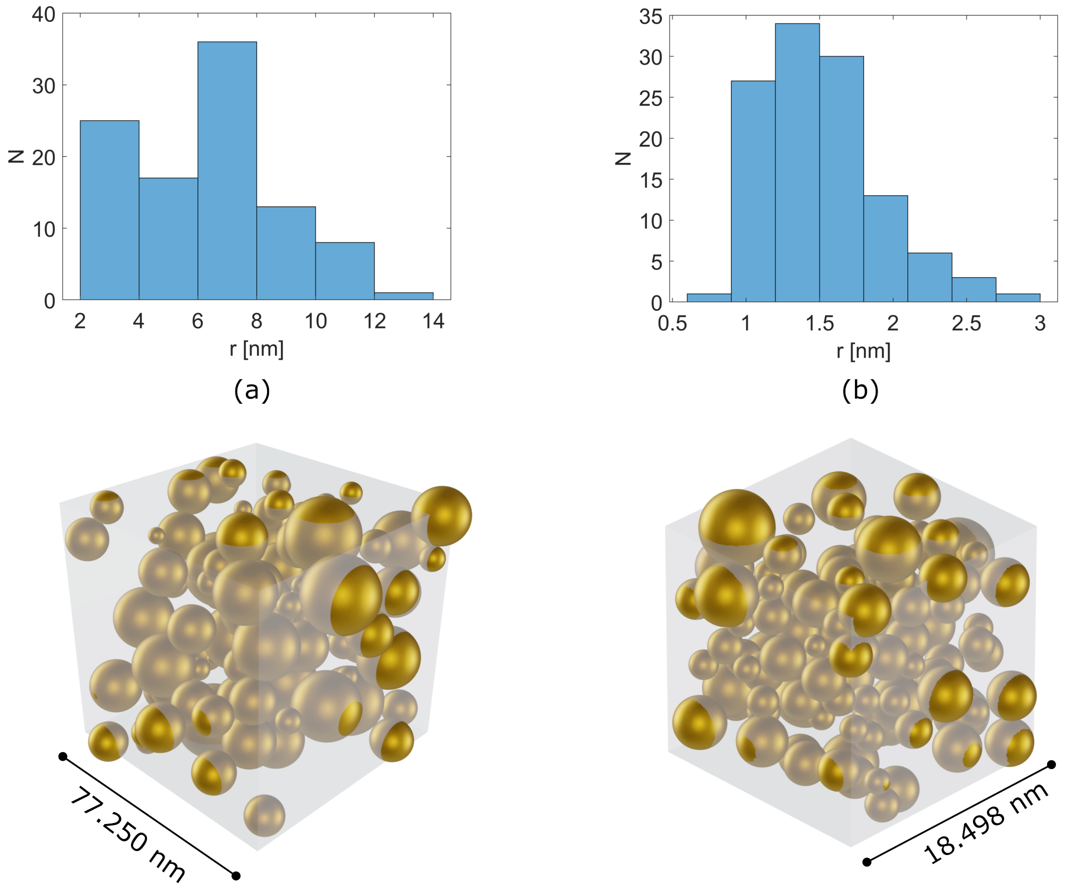

(a) (b) (c) (d)

Figure 3.16: Size distribution of nanoparticles obtained through (a) gas aggregation source method with $N = 100, FF = 33\%$ and (b) co-sputtering method with $N = 115, FF = 32\%$. Visualization of the nanoparticles cluster with its configuration according to (c) gas aggregation source and (d) co-sputtering method size distribution.

characterization of the thin film, we can find the reflectance of an unpolarized incident film by using Eq. 3.4. In that equation,the reflectance of unpolarized light (R_{unp}) is equal to the average reflectance of TE-polarized (R_{TE}) and TM-polarized (R_{TM}) waves as

$$R_{\text{unp}} = \frac{R_{\text{TE}} + R_{\text{TM}}}{2}. \tag{3.4}$$

We set the wavelength of the incident light from the ultraviolet to the near-infrared region ($\lambda = 250 - 1800$ nm), resembling the AM1.5 solar spectrum [94]. Additionally, we considered an oblique incidence for the incoming light, setting the angle of incidence at 60°, instead of normal incidence. This is done to better approximate real-world scenarios and to more accurately assess the performance of our copper absorber. This setting is in full agreement with the experimental details. Afterward, we compared the absorptance spectra of both the gas aggregation source-derived absorber and the co-sputtered absorber, as illustrated in Fig. 3.17. This figure presents a side-by-side comparison of the absorptance curves obtained from both experimental measurements and computational simulations. The gas aggregation

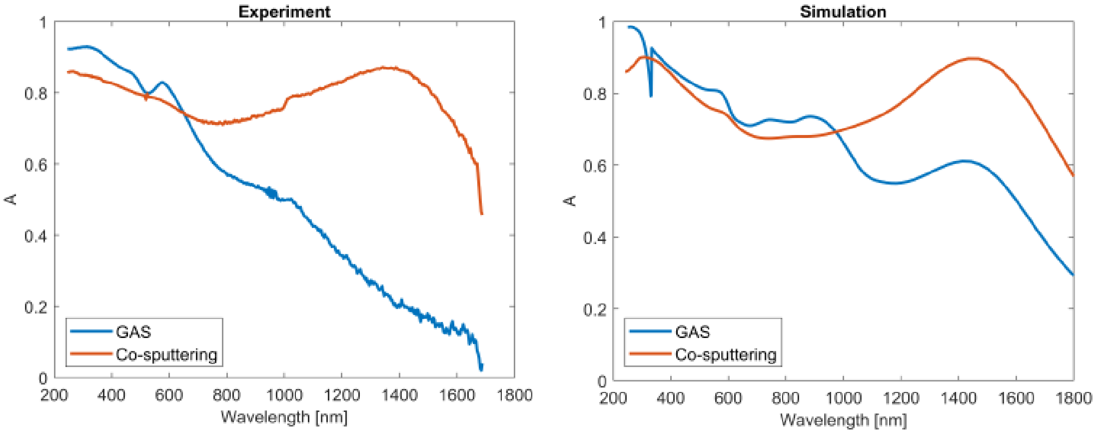

Figure 3.17: The absorptance spectra for plasmonic thin film absorbers fabricated via gas aggregation source (104 nm nanocomposite thickness, 33% Cu FF, blue curves) and simultaneous co-sputtering (100 nm nanocomposite thickness, 32% Cu FF, red curves). The side-by-side comparison of the experimentally obtained (left) and modeled (right) absorptance spectra is included.

source-derived absorber absorptance reveals discrepancies when comparing measured spectra to simulations, particularly at longer wavelengths. Both curves align closely in the shorter wavelength region. This can be attributed to the fact that the generalized impedance of the overall thin film layer stack matches that of air, leading to destructive interference in reflection and a rather high absorption. This suggests that the congruence observed in this region is primarily a result of the intrinsic properties of the thin film as a whole, rather than being influenced by the interactions of nanoparticles within the film. In other words, the intrinsic characteristics of the thin-film, like the material and the thickness of the thin-film, dominate the properties of the absorber at shorter wavelengths, i.e., around below $\lambda = 500$ nm. A similar trend has also been observed also at the Au_{144} absorber in Fig. 3.8(b). Meanwhile, the interaction of nanoparticles play a role at much longer wavelengths to have a broadband and strong absorption. Notably, the simulation (illustrated by blue lines in Fig. 3.17 on the right side) displays several maxima in this region, indicative of Fabry-Perot oscillation characteristics. In contrast, such oscillations are absent for the measured gas aggregation source-derived absorber. In the optimal design, reflection should be suppressed as much as possible. On the other hand, we observe an excellent agreement between the simulated and experimental absorptance spectra for the co-sputtered absorbers in Fig. 3.17.

This is evident both in the general shape of the curve, which presents a peak around 1400 nm, and in the overall absorptance values. Thus, it can be inferred that the co-sputtering technique offers a more effective approach to fabricate a layer embedded with metal nanoparticles for absorber devices compared to the gas-aggregation source method. In general, the absorptance curve has a strong and spectrally broad feature that is caused by the light that get trapped between the copper nanoparticles due to interaction between the copper nanoparticles at the antibonding mode, which is induced at wavelength around 1400 nm, in which not seen when we take a look on the Au_{144} molecules case.

From this point forward, our focus will be on a study of the copper nanoparticle absorber fabricated using the co-sputtering method. We are considering variations in the filling fraction, which are 25%, 32%, 40%, and 50%, as well as different nanocomposite layer thicknesses: 60 nm, 80 nm, 100 nm, and 140 nm. So that, we have a total of 16 absorber samples to examine. The absorptance spectra for each of these samples have been calculated, and the value of integrated absorptances, as defined in Eq. (3.3), have been obtained for each sample. To simplify the visualization and comparison of results, we have created an integrated absorptance heatmap that contains all variations in filling fraction and nanocomposite layer thickness, presented in Fig. 3.18. This figure facilitates a direct comparison of integrated absorptance between the experimental and simulated absorbers across the range of filling fractions and nanocomposite thicknesses. In the heatmap, a greyscale color scheme is used to represent the integrated absorptance values. A value of 0.604 corresponds to the absorber exhibiting the lowest absorptance, depicted in black and represents the 80 nm nanocomposite layer with a 50% filling fraction. On the other end of the spectrum, a value of 0.836, which is represented in white, corresponds to the absorber with the highest reflectance, specifically the 60 nm nanocomposite layer with a 25% filling fraction. From Fig. 3.18(c), a noticeable deviation is observed between the simulation and experimental results for the absorber thin films with a 50% filling fraction. As the layer becomes densely packed with copper nanoparticles, there arises a potential for the nanoparticles to come into contact with each other, possibly leading to the formation of accumulations termed as nanoislands, as previously discussed. This can result in an absorber where the nanoparticles exhibit weakened overall plasmonic interactions between their gaps. Furthermore, experimental observations, particularly from SEM images, show that at higher filling fractions, the nanoparticles deviate from a spherical shape. In such cases, standard geometrical descriptors like diameter or radius lose their relevance in characterizing the size of the copper nanoparticle within the nanocomposite. This deviation is a possible reason for the discrepancy observed between experimental and simulated absorption spectra. On the other hand, both simulated and experimental absorptance spectra have similar feature that there exists an optimal nanocomposite thickness beyond which increasing the thickness does not further reduce the integrated reflectance. For instance, the integrated reflectance for a 140 nm thick absorber consistently exceeds that of its 100 nm counterpart.

Lastly, we consider a multi-nanocomposite absorber. This absorber contains a stack of many separate copper nanocomposite layers with different filling fraction. The stack is deposited on top of an alumina spacer layer with 20 nm thickness and a copper mirror, illuminated with unpolarized light at 60° angle of incidence, just like when we consider a single-nanocomposite absorber. We define the stack with thickness equal to d_{dc}, so that each nanocomposite layer has a layer thickness of d_{dc}/N, where N is the number of layers in the stack. We consider cases where $N = 2$ and $N = 4$. We vary also the order of the layers according to the filling fraction of the nanocomposite layer, the filling fraction of the layers are made increasing or decreasing from top to bottom, illustrated in Fig. 3.19(a). For instance, we have a stack consisting of $N = 2$ layers with 25% filling fraction and 50% filling fraction. The layers here can have increasing or decreasing filling fraction from top to the bottom of Fig. 3.19(a). It is also the same when we consider $N = 4$ layers with 25% filling fraction, 32% filling fraction, 40% filling fraction and 50% filling fraction. So that, we continue by calculating the absorption spectra for all of the configuration of the absorber mentioned. Having established these configurations, our next course of

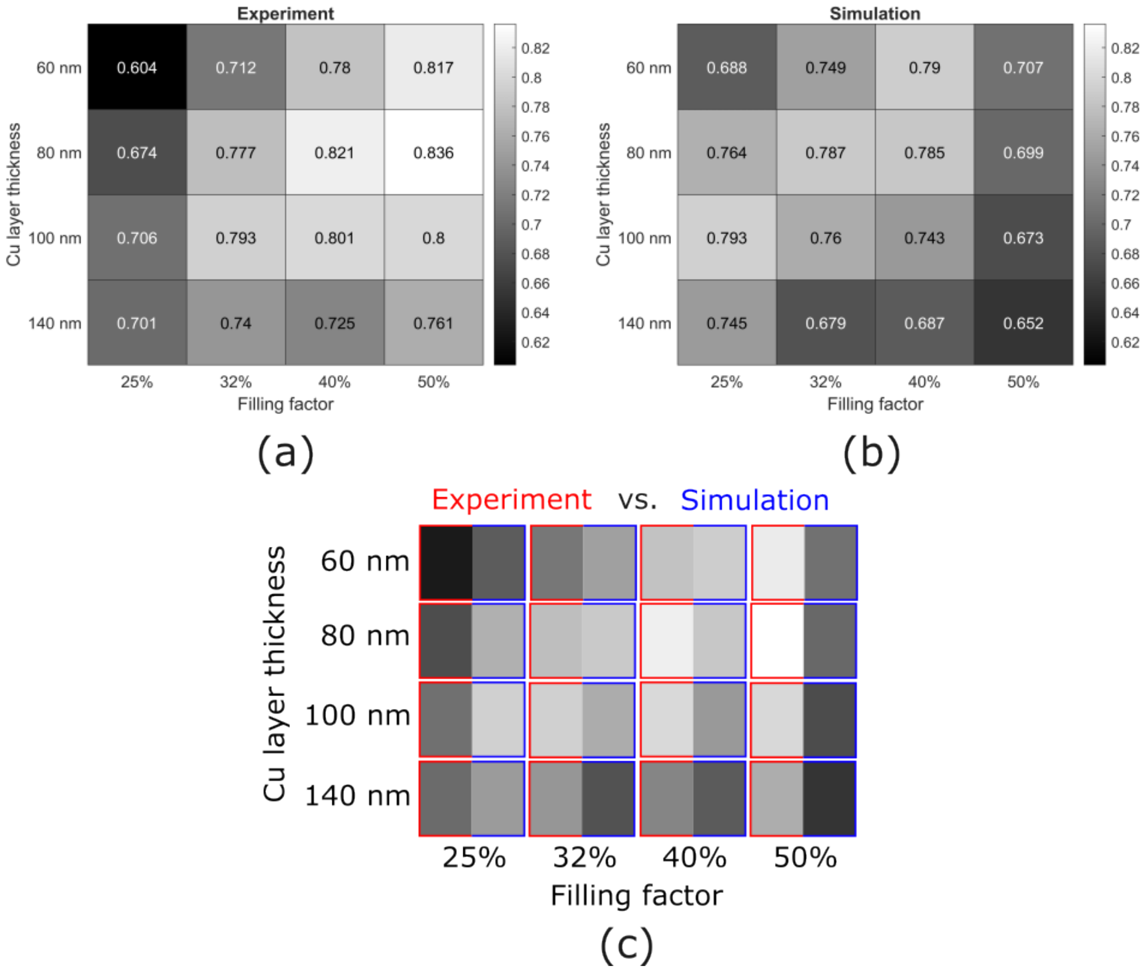

Figure 3.18: Heatmaps for the integrated absorptance that is (a) experimentally obtained as well as retrieved by (b) simulation. The nanocomposite film thicknesses is labelled in the y-axis and the filling fraction is in the x-axis. The greyscale represents the integrated absorptance, with white and black colors corresponding to the highest and lowest obtained absorptance, respectively. (c) A direct comparison between the experiment and simulation is provide. Adapted from [75].

action is to compute the absorption spectra for each distinct multi-nanocomposite absorber setup, shown in Fig. 3.19(b) in form of a colormap.

The results reveal the absorption curve of the multi-nanocomposite absorber with an increasing filling fraction has absorptance value with the best broadband absorption, compared to the other configurations. So that, the multi-nanocomposite absorber with an increasing filling fraction demonstrates better broadband absorption when compared to both the single-nanocomposite absorber and the multi-nanocomposite absorber with a decreasing filling fraction. Consequently, the results from the multi-nanocomposite absorbers indicate that there is a great potential for optimizing the absorption spectra of plasmonic absorbers.

Our next objective is to enhance the performance of the copper nanoparticles thin film absorber, optimizing it for broader and stronger light absorption. In subsequent subsections, we describe multiple aspects of the thin film absorber. First,

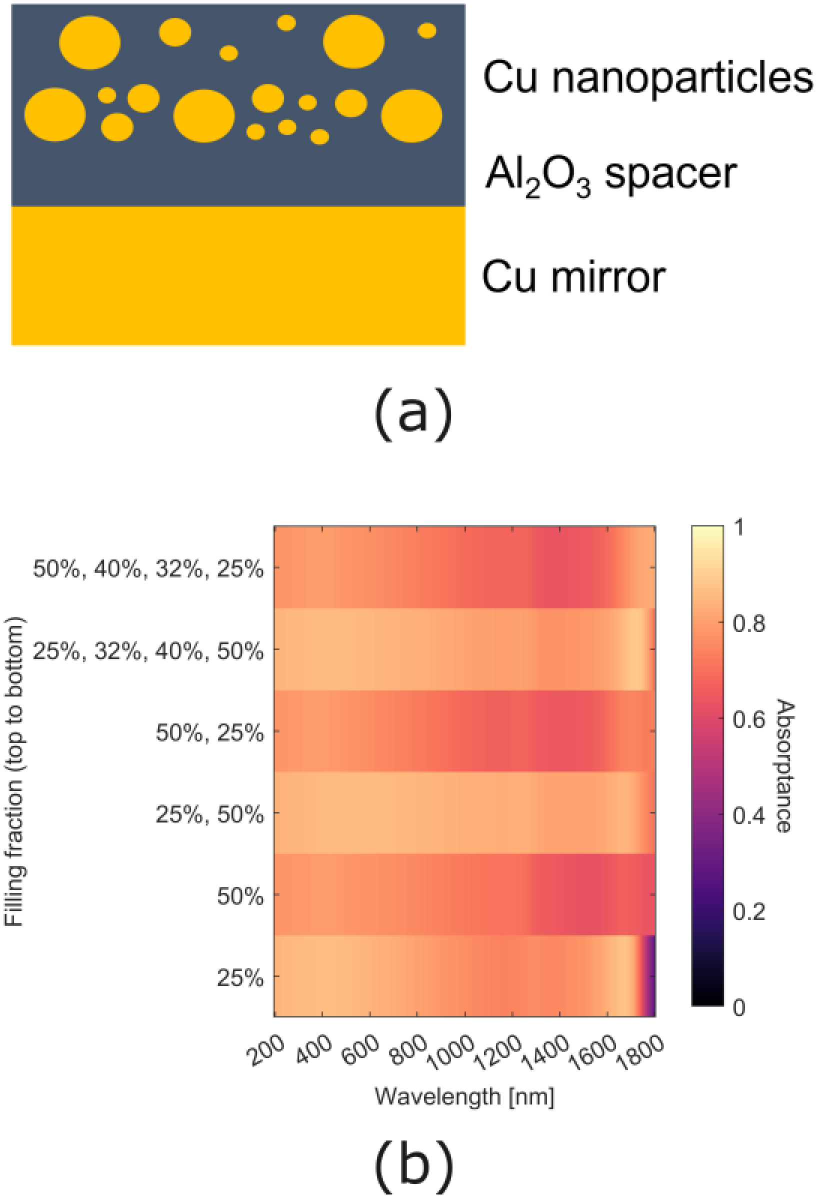

Figure 3.19: (a) The dual-nanocomposite absorber sketch, consisting of two layers of increasing nanoparticle filling fraction, an alumina spacer layer, and a copper mirror. (b) Absorption spectra colormap of copper single-nanocomposite absorber with 25% and 50% filling fraction, and multi-nanocomposite absorber with increasing and decreasing filling fraction. $d_{\mathrm{dc}} = 100$ nm is chosen.

we explore the thermal emission properties of the absorber, particularly focusing on calculations done in the infrared region. This is followed by an investigation into the influence of the surface roughness on the absorber's performance. Our prior discussions have highlighted that increased surface roughness can lead to attenuated absorption, especially at longer wavelengths, as observed in the experimental results. Further, we consider the thin film absorber with a mixture of copper and tungsten nanoparticles. The reason behind this mixture stems from the tungsten nanoparticles' ability to induce localized surface plasmon resonance at longer wavelengths than noble metals, therefore offering the potential to further broaden the absorptance spectrum. Concluding this section, we conduct a brief analysis of the thin film absorber that incorporates sharp-edged copper nanoparticles, aiming to discern the unique properties and performance enhancements they might contribute.

3.3.1 Thermal emission spectrum of the copper nanoparticle thin film absorber

In this section, we study the effect of emission at the infrared spectrum as we compare the absorptance from the thin-film absorber with the AM1.5 sunlight spectrum. The electromagnetic radiation emitted by the Sun due to its high temperature, is primarily in the form of visible light and near-infrared radiation. The Sun's intense heat, generated by nuclear fusion processes in its core, causes it to behave like a blackbody radiator. To understand the sunlight radiation, we have to know the Planck's law of blackbody radiation. Planck's law essentially describes how the intensity of radiation emitted by a blackbody varies with temperature and wavelength or frequency. It is worth noting that Planck's law played a pivotal role in the development of quantum mechanics because it introduced the idea that energy is quantized in discrete units (quanta), which was a departure from classical physics at the time. The spectral irradiance $I(T,\lambda)$ of a body can be known through Planck's law of blackbody radiation equation in the specific absolute temperature of the body T, and wavelength λ is

$$I(T,\lambda) = \frac{2hc^2}{\lambda^5}\frac{1}{e^{\frac{hc}{\lambda k_\mathrm{B} T}} - 1}, \tag{3.5}$$

where h is the Planck constant, c is the speed of light, and k_B is the Boltzmann constant. According to Planck's law of blackbody radiation in Eq. 3.5, the Sun's emission spectrum closely follows that of an ideal blackbody, with a peak in the visible part of the spectrum.

We calculate the light emission through emissivity. Emissivity is a material property that describes how efficiently an object or material emits thermal radiation. According to Kirchhoff's law of thermal radiation, the emissivity of an object at a particular wavelength is equal to its absorptivity at that same wavelength. This means that materials that are good at absorbing thermal radiation at a given wavelength are also good at emitting radiation at that wavelength. To obtain the emissivity, it is important to determine the fraction of sunlight energy that the Earth absorbs. Considering that the energy from the sun propagates in a spherically expanding wavefront, we can calculate the radiant flux, denoted as Φ_earth, at the Earth's surface. The radiant flux can be computed by multiplying the spectral irradiance $I(T,\lambda)$ by the Earth's surface area, which is approximately $1.3 \times 10^{14}\mathrm{m}^2$. For the sake of simplification in our model, we have chosen to ignore the influence of the Earth's atmosphere. Subsequently, the radiant flux of our thin-film absorber sample can be calculated by multiplying the radiant flux of the Earth with the absorptivity of the absorber. The emissivity is then defined as the ratio of the Earth's radiant flux to the sample's radiant flux, as stated in Eq. 3.6.

$$e = \frac{\Phi_\mathrm{sample}}{\Phi_\mathrm{earth}}. \tag{3.6}$$

So, the emissivity typically ranges between 0 and 1, where 0 indicates a perfect thermal reflector (no emission), and 1 signifies a perfect thermal emitter (complete emission). However, we want to minimize the emission in the infrared spectrum. In devices like STC, minimizing infrared emission is crucial because infrared represents heat. If a device absorbs sunlight (or any other form of energy) and then re-emits a significant portion of it in the form of infrared radiation, it effectively loses energy. By minimizing this infrared emission, the device retains more of the absorbed energy, therefore operating at a higher efficiency. Also, if the absorber continually emits and thus loses energy as infrared, it might need external cooling solutions to prevent overheating. Meanwhile, we consider the absorptivity as the objective function in Eq. 3.3.

We consider the thin-film absorber calculated through simulation with the nanoparticle size distribution obtained by the gas aggregation source method with 41.5% nanoparticle filling fraction, as the first sample. This will be compared with the much more superior 25% – 50% FF dual-nanocomposite configuration, illustrated in Fig. 3.19(a), as the second sample. We set the working temperature of the thin-film absorber to a maximum of 400K [95]. This temperature can be achieved through concentration technologies such as parabolic troughs or linear fresnel collectors that track the sun with moving mirrors or a reflective coating [96]. We note that both thin film absorber is illuminated with unpolarized light with normal incidence. The first sample has $d_{\text{np}} = 35$ nm and $d_{\text{spacer}} = 46$ nm and the second sample has $d_{\text{np}} = 35$ nm and $d_{\text{spacer}} = 46$ nm. In Fig. 3.20 and Fig. 3.21, we compare the absorptance with the sunlight spectral irradiance in the ultraviolet to near-infrared (UV-NIR) region ($\lambda = 250 - 1800$ nm) in a same figure. Also, we compare the absorptance with the absorber emission curve from the UV to the infrared region ($\lambda = 250 - 20000$ nm) to determine the emissivity of the sample. From Fig. 3.20, it is evident that the thin film absorber with single-layer copper nanoparticles showcases an absorptivity of 7.6% across the ultraviolet to near-infrared (UV-NIR) spectrum. Interestingly, this absorber's capacity to absorb light is particularly concentrated in the region corresponding to the most intense sunlight radiation, which falls within the green part of the spectrum. Even at longer wavelengths, where sunlight radiation is less intense, the absorber still retains a decent absorptance. However, as we take a look into

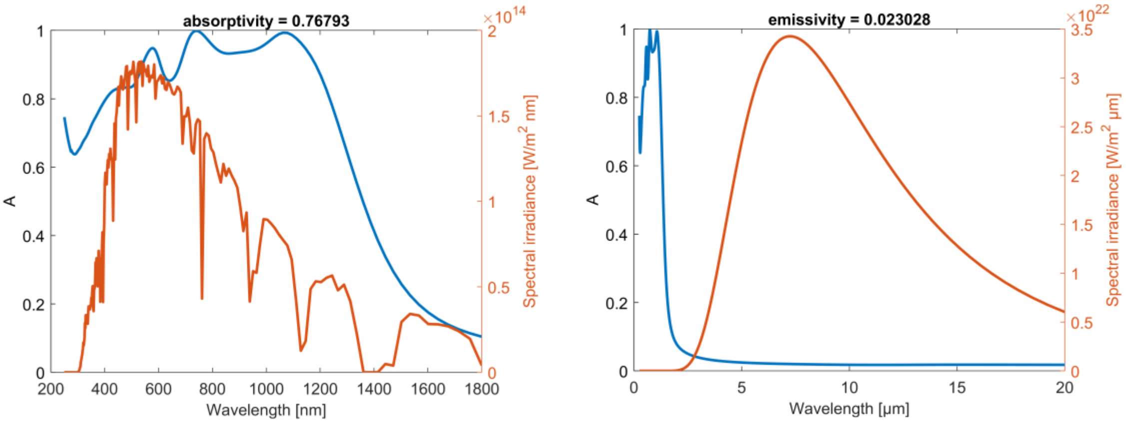

(a) (b)

Figure 3.20: The absorptance curve for a thin film absorber with a single nanoparticle layer 41.5% nanoparticle filling fraction (red line) and the AM1.5 sunlight spectrum spectral irradiance curve, calculated in (a) $\lambda = 250 - 1800$ nm and (b) $\lambda = 250 - 20000$ nm.

much longer wavelengths—extending up to 20 micrometers in the infrared domain, particularly starting from 1100 nm—the absorptance curve exhibits a marked decline. Notably, when the absorber operates at a temperature of 400K, it emits robust thermal radiation around the 7-micrometer wavelength at its strongest, with an emissivity of 2.3%. At this specific wavelength, the absorber displays minimal light absorption, which consequently contributes to its high efficiency.

Then, we consider the dual-nanocomposite thin film absorber, which has been shown in previous sections can absorb the electromagnetic field better. The absorptance curves in comparison with the sunlight and the working absorber emission spectrum are shown in Fig. 3.21. From our observations, it is evident that the dual-nanocomposite thin film absorber maintains an almost constant absorptance, with an 87% absorptivity across the UV-NIR spectrum. This consistency is indicative of an ideal scenario for achieving broadband-perfect absorption. Furthermore, the absorptance exhibits an oscillatory pattern, which can be attributed to the Fabry-Perot resonance. In contrast, the emissivity value of this dual-nanocomposite thin film is significantly higher than that of its single-nanocomposite counterpart. For applications, it is crucial to optimize the design of the thin film absorber such that we maximize absorptivity in the sunlight spectrum region while minimizing emissivity in the infrared region, as this dual quality enhances the material's performance in thermal management and energy-harvesting applications.

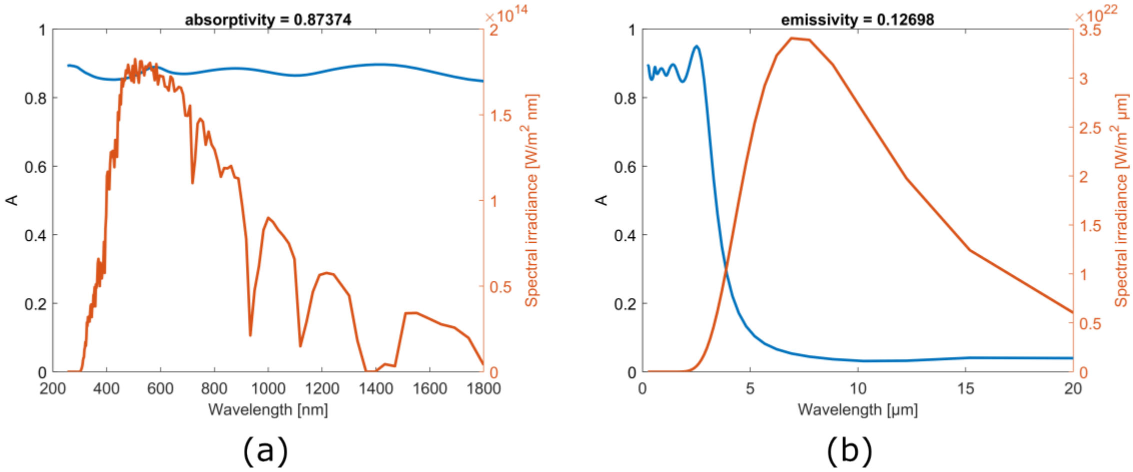

(a) (b)

Figure 3.21: The absorptance curve for thin film absorber with a dual-nanocomposite layer, 25% – 50% (top to bottom) nanoparticle filling fraction (red line) and the AM1.5 sunlight spectrum spectral irradiance curve, calculated in (a) $\lambda = 250 - 1800$ nm and (b) $\lambda = 250 - 20000$ nm.

3.3.2 The effect of surface roughness at the thin film broadband absorber

As mentioned previously, the absorptance of the copper thin film absorber fabricated through the gas aggregation source method fails to match the absorptance calculated through simulation. One significant reason for this discrepancy is the introduction of surface roughness on the upper layer of the absorber causing additional unwanted reflection. So, in this section, we study briefly the effect of surface roughness on the thin film absorber with computational means. To model this, we can initiate by representing the rough surface using a three-dimensional grid. Each point on this grid is characterized by a displacement vector, capturing the details of the surface profile.

The surface roughness can be modeled by generating random roughness. We start by defining a three-dimensional grid that represents the surface. Each grid point can be associated with a displacement $(\Delta x, \Delta y)$ for 3D. One of the primary tools to analyze this modeled surface is the auto-correlation function (ACF) [97]. The ACF aids in determining the spatial relationships or correlations between different points on the rough surface. Specifically, it quantifies how the elevation or depth at one specific point relates to that of another point located at a distinct distance. Through this function, we can extract vital insights about the periodicity, randomness, or dominant features of the surface. For instance, if the ACF drops to zero rapidly, it implies that the surface has a short-range order, indicating a high degree of randomness. On the other hand, a slow decay may suggest periodic or structured patterns in the roughness. The auto-correlation function Ξ of a surface height profile $h(x, y)$ is given by

$$\Xi(\Delta x, \Delta y) = \langle h(x, y)h(x + \delta x, y + \delta y)\rangle, \tag{3.7}$$

where the angle brackets denote an average overall position (x, y). Among the various forms of auto-correlation functions, the exponential and Gaussian auto-correlation functions stand out due to their unique characteristics and wide applicability. The exponential auto-correlation function captures correlations that decay at a constant rate and the Gaussian auto-correlation function is characterized by its bell-shaped curve. The exponential and Gaussian auto-correlation function is defined in Eq. 3.8 and Eq. 3.9,

$$\Xi(\delta x, \delta y) = \sigma^2 e^{2.3}(\frac{\sqrt{x^2 + y^2}}{b}), \tag{3.8}$$

$$\Xi(\delta x, \delta y) = \sigma^2 e^{-\frac{\pi}{4}}(\frac{\sqrt{x^2 + y^2}}{b}). \tag{3.9}$$

The auto-correlation function depends on the root-mean-square (RMS) roughness σ, which is the standard deviation of the surface topography, stated in Eq. 3.10,

$$\sigma = \sqrt{\lim_{L_x, L_y \to \infty} \frac{1}{L_x L_y} \int_{-L_y/2}^{L_y/2} \int_{-L_x/2}^{L_x/2} [z(x, y) - \bar{z}]^2 \; dx \; dy}. \tag{3.10}$$

The RMS roughness provides a quantitative measure of surface height variations from the mean surface height, meaning the general magnitude of surface irregularities. The auto-correlation function uses this value to determine how these height variations or features correlate over different spatial scales or distances. In essence, the auto-correlation function gives insight into the patterns and periodicities of the roughness, while the RMS roughness determines the roughness magnitude. Then, the correlation length b, the length that denotes the distance over which two points on a surface remain correlated affects the auto-correlation function. The correlation length can provide insight into the size of the dominant features or patterns on the surface. For instance, if a surface has a short correlation length, it suggests that the surface has rapidly varying features, whereas a long correlation length would imply more extended, larger-scale features or patterns. We plot the autocorrelation function of exponential and Gaussian distribution in Fig. 3.22. Then, we determine the power

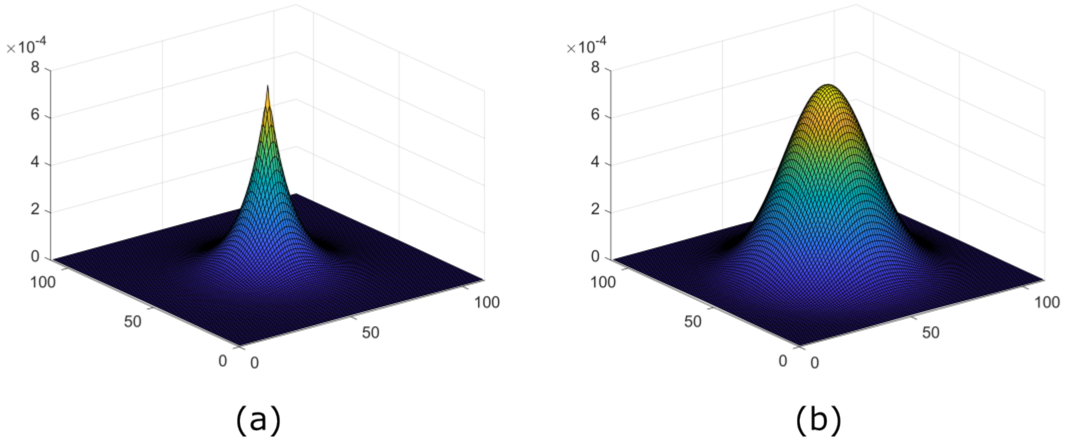

Figure 3.22: The auto-correlation function of (a) exponential and (b) Gaussian distribution. $\sigma = 0.1$ and $b = 0.028$ are used in this figure.

spectral density function. This function provides a representation of the amplitude of a surface's roughness as a function of the spatial frequency of the roughness. After determining the power spectral density function, it is essential to remember that it sheds light on which frequencies are dominant and which ones are less pronounced. By performing the Fourier transform of the auto-correlation function, we are essentially transitioning from the spatial domain into the frequency domain. This representation makes it easier to scales of roughness present in our surface. Subsequently, by taking the inverse Fourier transform of this frequency response, we obtain a filter function. This filter function acts as a function to generate the desired surface profile with roughness. The result is the surface profile depicted in Fig. 3.23(a-c). It can be seen from Fig. 3.23(a) and Fig. 3.23(b) that a smaller RMS roughness (σ) indicates a higher degree of randomness in surface roughness. Specifically, surfaces characterized by an exponential auto-correlation function display much sharper peaks compared to those with a Gaussian auto-correlation function. This pronounced peak structure is inherently characteristic of the exponential auto-correlation function. On the other hand, when we consider the surface profile governed by the Gaussian auto-correlation function, as depicted in Fig. 3.23(c), we observe a considerably smoother surface.

For the next step, we determine the reflection and transmission coefficients for a stack that comprises copper nanoparticles within an alumina layer, with rough alumina surfaces atop the nanoparticle layer, using an in-house infinite-difference time-domain method code. Subsequently, the stack's effective permittivity is calculated using the retrieval method, which will then be applied to the transfer matrix method to accommodate more complex layers. The thin film absorber is illustrated in Fig. 3.23(d). We fixed the copper nanoparticle thickness and the alumina spacer layer to 120 nm and 20 nm, respectively. We consider normal incidence with TM polarization. Then, we calculate the absorptance from 250 nm to 1400 nm wavelength, represented in Fig. 3.23(e). When comparing the black line with the solid red and blue lines in Fig. 3.23(e), it becomes apparent that the inclusion of surface roughness in the thin film absorber results in reduced absorption at wavelengths above 600 nm. Notably, the surface profile does not introduce any additional distinct absorptance curve features. Further, the absorptance associated with the absorber possessing a

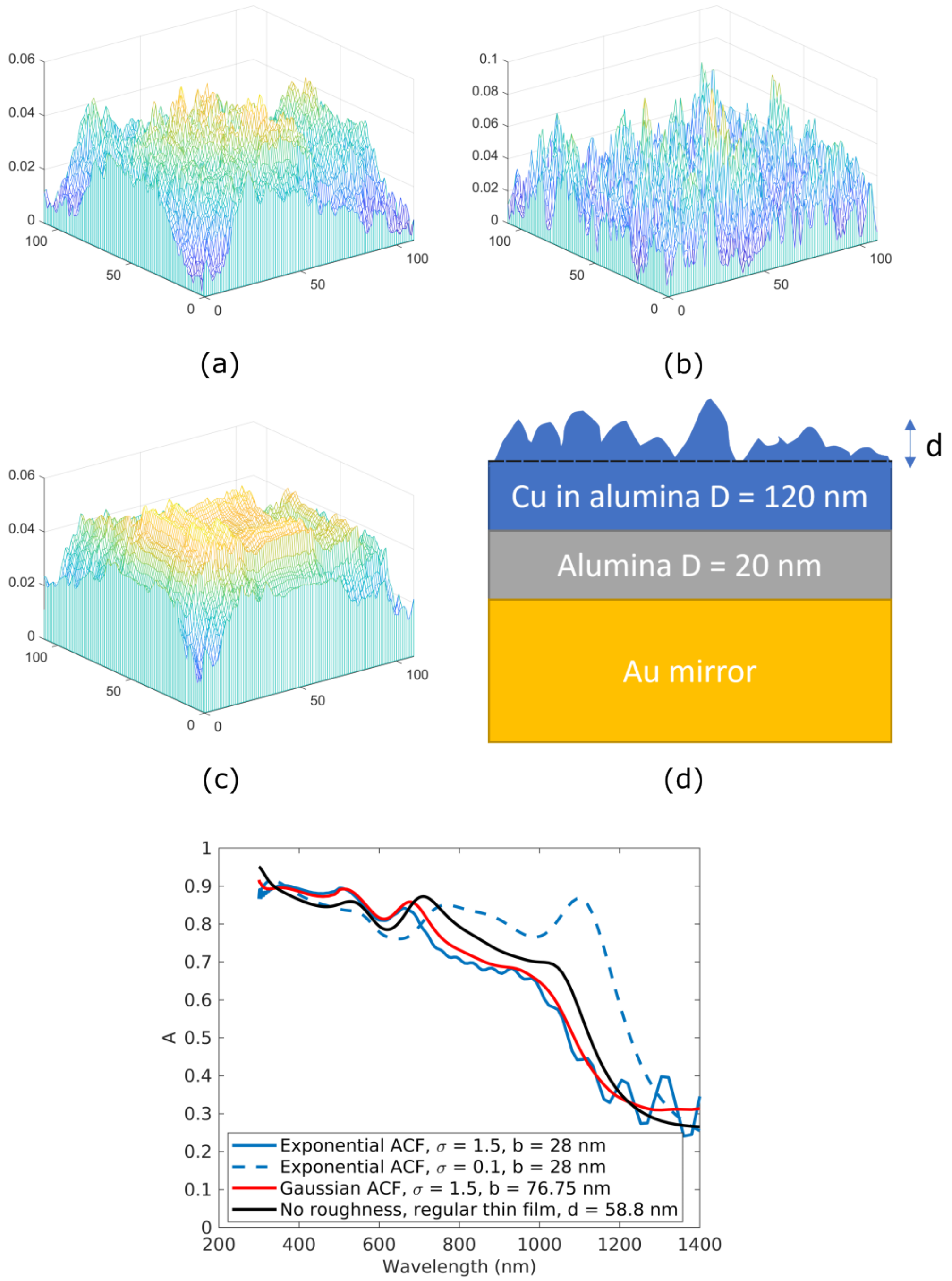

(a) (b)

(c) (d)

(e)

Figure 3.23: The surface profile generated by exponential auto-correlation function with (a) $\sigma = 1.5, b = 28$ nm and (b) $\sigma = 0.1, b = 28$ nm. (c) The surface profile by Gaussian auto-correlation function with $\sigma = 1.5, b = 76.25$ nm. (d) A sketch of the copper nanoparticle thin film absorber with the surface profile integrated on top of the absorber. The distance between the surface of the nanoparticle layer to the tallest peak of the rough surface is defined as d. (e) The absorptance of the thin film absorber varies with changes in the surface profile. For comparison, the absorptance of the thin film absorber without surface roughness is also included.

smaller RMS roughness, as depicted by the dashed blue line, surpasses that of the non-rough absorber. This suggests a possibility of surface roughness optimization. Such optimization can provide a balance between achieving broadband and strong absorptance and preserving the structural integrity of the absorber.

3.3.3 Thin film absorber with copper-tungsten nanoparticles mixture

In our next research, we examine thin film absorbers embedded with copper nanoparticles, which are also combined with nanoparticles of alternative materials. The primary objective is to ascertain whether this combination can enhance the absorber's performance, enabling it to absorb light at wavelengths extending beyond the near-infrared region. One promising approach involves integrating nanoparticles made of materials known to sustain localized surface plasmon resonance at near-infrared wavelengths, such as tungsten, as discussed by Andersen *et al.* [98]. Consequently, we aim to analyze the interaction between tungsten and copper nanoparticles in broadening the absorptance spectrum. To initiate our simulation, we refer to the size distribution of nanoparticles depicted in Fig. 3.24, which is representative of a sample fabricated using the gas aggregation source method. As the next step, in the multiscale modeling technique, we partition the nanospheres such that one half comprises one specific material, while the other half is composed of a different material. We refer to this configuration as a "nanoparticle mixture." To enlighten, consider a cluster composed of 324 nanospheres, which is a number of spheres considered in Fig. 3.24: we would allocate 162 nanospheres to be made of copper and the remaining 162 to be made of tungsten. The assignment of each nanosphere to its respective material is done randomly to ensure a heterogeneous distribution. On the technical front, we initially calculate two distinct T-matrices: one for a singular copper nanosphere

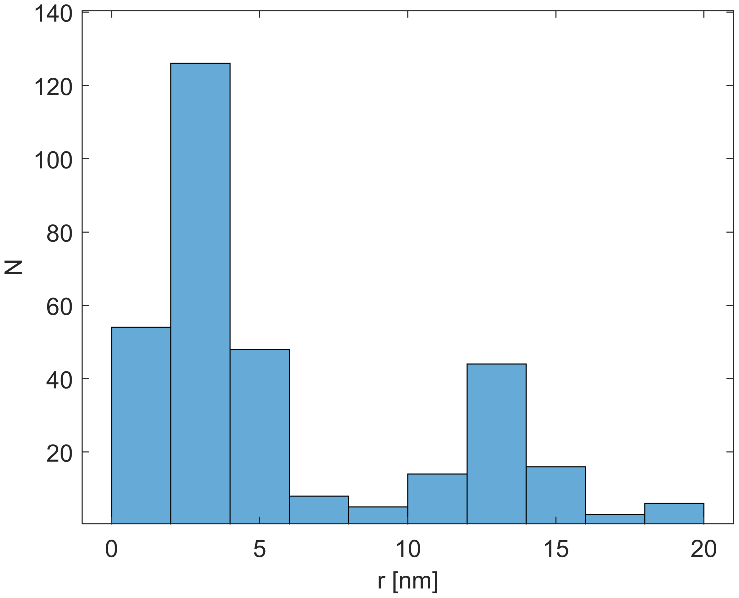

Figure 3.24: Size distribution of nanoparticles with 40% filling fraction in 136 nm side lattice length cubical unit cell.

and another for a singular tungsten nanosphere. From there, we compute the global T-matrix for the entire cluster, taking into account the nanoparticle mixture of both copper and tungsten. We apply the experimental refractive index by Werner *et al.* [99]. Once this is achieved, the following steps in the multiscale modeling technique align with the methods in previous sections. Specifically, we determine the absorptance of a thin film system. This system is comprised of an alumina layer embedded with a copper-tungsten nanoparticle mixture, an alumina spacer layer, and a reflective copper mirror base. The thin film absorber is illuminated with TM-polarization with 52.5852° optimized angle of incidence. The nanoparticle layer and spacer layer thickness are swept along 0 to 100 nm to find the optimal configuration of the thin film absorber. Figure 3.25(a) shows the integrated absorptance colormap, concerning the thicknesses of the thin film absorber. From Fig. 3.25(a), it is observed that the thin film absorber exhibits its largest integrated absorptance when the nanoparticle layer has a thickness of 62 nm and the spacer layer has 8 nm in thickness. We plot the absorptance of the nanoparticle mixture thin film absorber with this particular thickness configuration in Fig. 3.25(b). According to Fig. 3.25(b), it is seen that the absorptance remains consistently close to one across the ultraviolet to the visible light spectrum with an impressive 0.96578 integrated absorptance. However, there is a noticeable decline beginning at a wavelength of 825 nm and continuing beyond this point. Based on these observations, we guess that there exists an ideal mixture composition that could sustain an absorptance value of over 0.9 across the entirety of the considered spectral region.

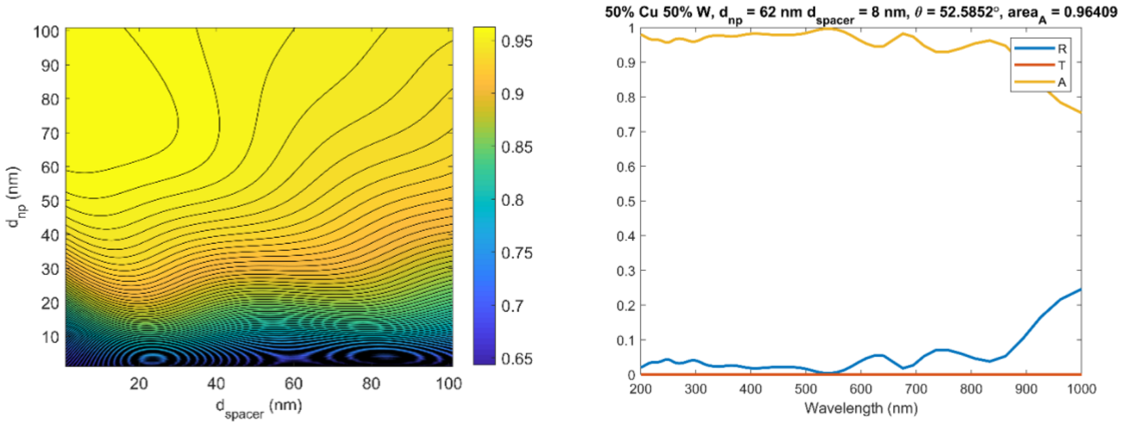

(a) (b)

Figure 3.25: (a) A colormap describing the integrated absorptance in respect to the copper-tungsten nanoparticle mixture layer thickness d_{np} and the alumina spacer layer thickness d_{spacer}. The region in yellow determine the region of optimal thin film absorber thicknesses. (b) Absorptance curve with $d_{\mathrm{np}} = 70$ nm and $d_{\mathrm{spacer}} = 8$ nm, according to the Fig. (a).

Furthermore, we explore a nanoparticle mixture composed of three metals: copper, gold, and aluminum. The localized surface plasmon interactions within a single cluster containing nanoparticles of these varied metallic compositions present a potential for a study. In this scenario, we adjust the percentage compositions of the metals in the nanoparticles, with maintaining the same size distribution as we previously observed in the copper-tungsten nanoparticle mixture. Following a similar approach as before, we identify the optimal metallic nanoparticle mixture and proceed to calculate the absorptance based on this optimized composition. Initially, we set the nanoparticle layer thickness at 32 nm and the spacer layer thickness at 10 nm. These thin film absorber configurations have been derived from the optimal thin film thicknesses observed when the cluster consists of 100% copper nanoparticles. Later, with these parameters fixed, we compute the integrated absorptance across various metal mixture possibilities. The results of these calculations are visualized in a ternary plot, as depicted in Fig. 3.26(a). According to the ternary plot in Fig. 3.26(a), the optimal nanoparticle mixture comprises 63% copper, 33% gold, and 4% aluminum. This suggests that aluminum interacts minimally with the other nanoparticles within the cluster. However, when comparing the performance, it appears that the absorber with the copper-gold-aluminum nanoparticle mixture is less effective than the one with the copper-tungsten nanoparticle mixture. Specifically, the absorptance is strongest between wavelengths of 300 nm and 500 nm. This can be attributed to the proximity of the localized surface plasmon resonance peak wavelengths of the metals in consideration. Generally, copper, gold, and aluminum exhibit LSPR peaks at wavelengths shorter than 800 nm. This similarity in their localized surface plasmon resonance wavelengths results in weaker plasmon interactions at longer wavelengths. From this analysis, we can infer that by combining nanoparticles with diverse localized surface plasmon resonance peaks spanning a broader spectrum, it is possible to achieve both broadband and strong absorption within the thin film absorber.

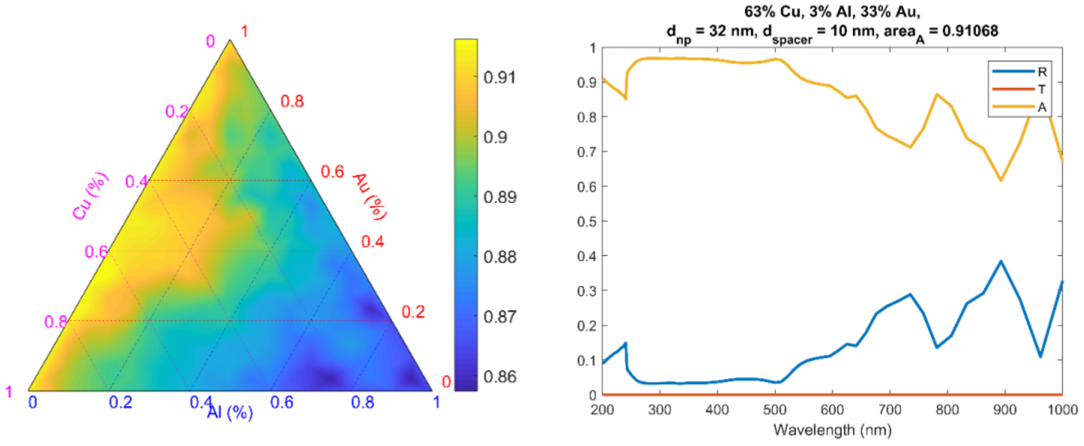

(a) (b)

Figure 3.26: Cubical unit cell for a cluster containing 500 metallic molecules classically described as small metallic nanoparticles.

3.3.4 The effect of oxidized copper nanoparticles to the thin film broadband absorber

In this subsection, we examine thin film absorbers that incorporate copper oxide nanoparticles. Unlike pure copper nanoparticles, a significant portion can undergo oxidation during the sputtering deposition process, resulting in the formation of copper oxide or cuprite (CuO) nanoparticles, as noted by Su *et al.* [100]. This means that, from an experimental standpoint, the nanoparticle layer will not exclusively contain pure copper nanoparticles. As a consequence, it becomes vital to understand the implications of the presence of cuprite nanoparticles on the absorptive properties of the thin film absorber. We calculate the absorptance for this particular type of absorber, taking into account a filling fraction of 40% for both types of nanoparticles and an incidence angle of 52 degrees under TM-polarization. We note that the experimental cuprite refractive index is used [101] in this case. Figure 3.27 presents the absorptance data for the thin film absorber with pure copper and copper oxide nanoparticles. The thickness of these absorbers then is optimized by parameter sweeping to maximize the integrated absorptance. From the data presented in Fig. 3.27, it is clear that the absorptive properties of thin film absorbers with cuprite nanoparticles are less effective than those of pure copper nanoparticles, especially in the longer wavelength range. This reduced absorptive capability of cuprite can be attributed to its attenuated localized surface plasmon resonance strength, which results from the presence of its oxygen atoms that make cuprite. Consequently, the presence of cuprite within the nanoparticle layer can be pinpointed as a contributing factor to the observed diminished near-infrared absorption, as depicted in Fig. 3.17.

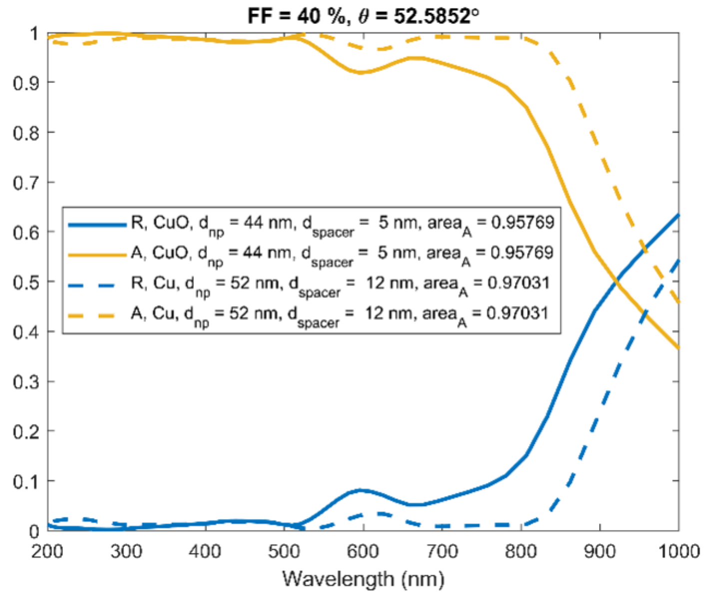

Figure 3.27: The reflectance and absorptance of thin film absorber with copper and copper oxide nanoparticles. The optimal thin film thicknesses are used in this figure for each case copper and copper oxide thin film absorber, stated in the figure legend, with their integrated absorptance.

3.3.5 The potential of using sharp-tipped nanoparticles to the thin-film broadband absorber

The plasmon interaction between non-spherical nanoparticles presents interesting research, particularly when examining nanoparticles with sharp tips, such as nanocones and nanostars. Studies have shown a significant near-field enhancement induced due to localized surface plasmon resonances at the tips of these structures, thereby increasing the probability of light trapping between the sharp-tipped nanoparticles [102, 103]. This can be attributed to the concentrated electric field at the sharp edges and tips, which amplifies the interaction with incident light. To validate this claim, we analyze where we calculate the absorption cross-section of various structures with similar size: a single gold nanosphere, a nanocone, and a stellated nanooctahedron, depicted in Fig. 3.28(a). We can see from Fig. 3.28 that the absorption cross section for sharp-tipped nanoparticles is generally larger than with spherical nanoparticles, except at the localized surface plasmon resonance peak of the nanosphere around 550 nm wavelength. It is noted that the absorption cross section for the nanocone features a very strong and sharp at $\lambda = 683$ nm. Also, the stellated nanooctahedron absorption cross-section curve has slower decay in longer wavelength compared with the other curves, leading to broader absorption. So that, we can exploit these features of the sharp-tipped nanoparticles to be applied to the thin film absorber.

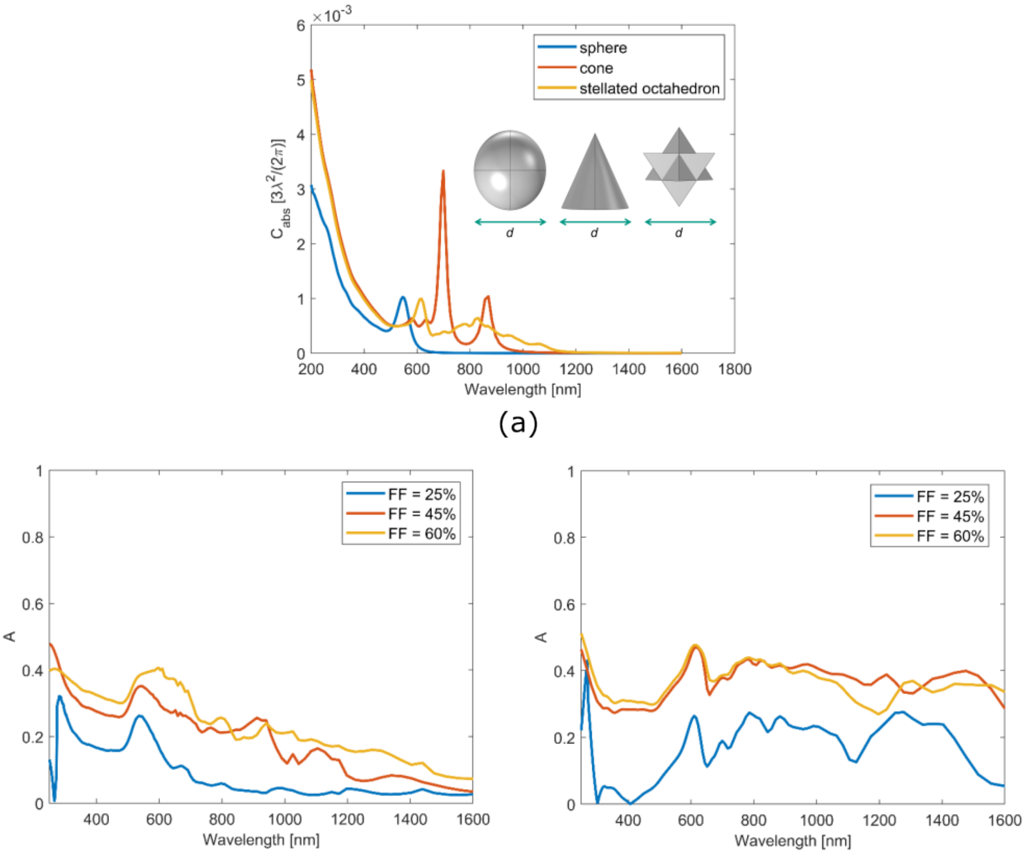

(a)

(b)

(c)

Figure 3.28: (a) The absorption cross section of a single gold nanosphere, nanocone, and stellated nanooctahedron. The dimension length d of the nanoparticles considered is set equal to 10.62 nm, illustrated in the inset of the figure. The absorptance of the golden (b) nanocones and (c) stelllated nanooctahedrons thin film absorber with variation of filling fractions $[FF = 25\%, 45\%, 60\%]$

Further, we consider the thin-film absorber with nanocones and stellated nanooctahedron with a variation of nanoparticles filling fractions, which is $FF = 25\%, 45\%, 60\%$. Figure 3.28(b) and (c) represents the absorptance resulting from the sharp-tipped nanoparticles thin-film absorber. It is observed that the golden stellated nanooctahedron absorbs light more consistently and is stronger at a longer wavelength, compared to the nanocone. This is due to that a stellated nanooctahedron has more sharp tips than a nanocone, causing more near-field enhancement surrounding the stellated nanooctahedron. However, we see that the thin film absorber with sharp-tipped nanoparticles absorptance value is lower as not be expected from results in this thesis for all of the nanoparticles filling fraction variation. We note that this anomaly is due to that the Rayleigh hypothesis is violated. The Rayleigh hypothesis is an assumption often used to state that the scattered field can be expanded everywhere outside a particle with a series of spherical waves arising from the origin of the scatterer, but only valid in the region outside of a sphere that circumscribes this particle [104, 105]. This means that the near-field interaction between the sharp-tipped nanoparticles is invalid, leading to weak absorption.

3.4 Thin-film broadband absorber with cobalt nanoparticles

In this section, we study a thin-film absorber with cobalt nanoparticles. The cobalt nanoparticles have been studied as a basis for an electromagnetic wave absorber in microwave region [106]. So, we want to know whether cobalt nanoparticles could be used to absorb light in optical frequencies. In this case, the thin film is considered to consist of a layer with cobalt nanoparticles in a silica matrix and a glass substrate ($n = 1.5$) as the reflector. Experimentally, the cobalt nanoparticles thin film is fabricated by utilizing an in-house magnetron sputtering system, having size distributions according to Fig. 3.29. Then, using the size distribution, we utilize

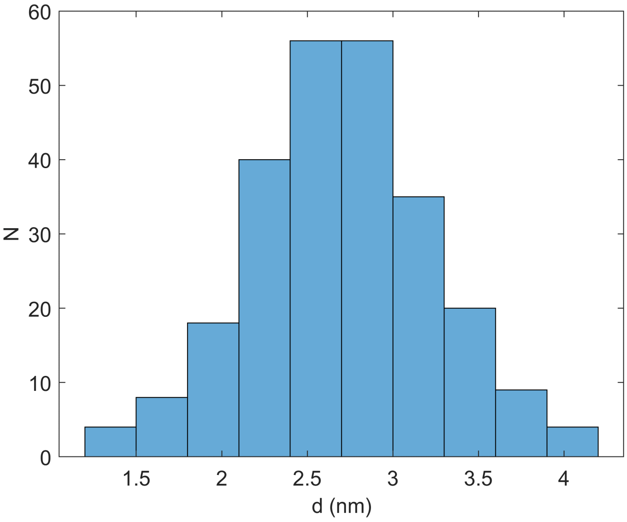

Figure 3.29: Cobalt nanoparticles size distribution for 48% filling fraction, consisting of 250 spheres in a cubical unit cell lattice constant equal to 18.5 nm.

the same computational methods and details used in Section 3.3 to calculate the reflectance at $\lambda = 250 - 1600$ nm. The thin-film absorber is illuminated with light with oblique incidence with an angle of incidence equal to 45° and 70°. We set the nanoparticle layer thickness fixed to 20 nm and the nanoparticle filling fraction is varied from 28% to 58%. The reflectance curves measured by the experiment and calculated through simulation are compared for all of the degree of freedom variations, shown in Fig. 3.30. We should begin by acknowledging that absorptance

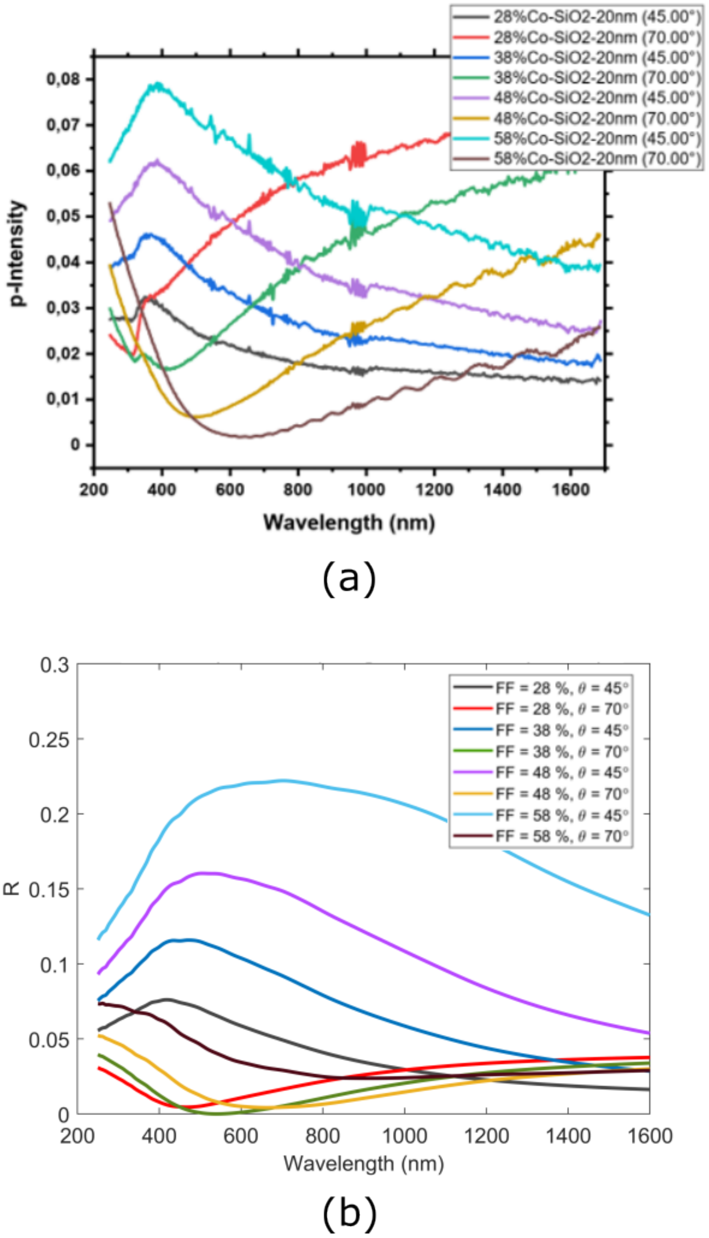

Figure 3.30: Reflectance curves for cobalt nanoparticles thin film absorber obtained by (a) experiment and (b) simulation. 28% to 58% nanoparticle filling fraction variation is considered with 45° and 70° angle of incidence.

can be expressed as one minus reflectance when considering a glass substrate with a notably very high thickness, making transmittance negligible. This implies that low reflectance values correspond to high absorptance. According to Fig. 3.30, we figure out a correspondence between the experimental and computational reflectance data, revealing shared features while notably diverging in terms of amplitudes. It is reasonable to guess that this discrepancy may caused by limitations in measurement sensitivity within the experimental apparatus. Nonetheless, the overall qualitative agreement highlights the validity of our computational approach. Surprisingly, we observe a trend where reflection becomes stronger as the filling fraction of cobalt nanoparticles increases, irrespective of the angle of incidence, with slight redshifting. This presents a contrast to what we might expect based on previous experiences with copper nanoparticle thin films. The explanation behind this lies in cobalt's inherently weaker localized surface plasmon resonance (LSPR) strength in comparison to copper, This diminished LSPR effect results in a reduced interaction due to plasmon hybridization between cobalt nanoparticles, therefore showing the importance of the role of nanoparticle filling fraction in enhancing absorption. Furthermore, we note a difference in reflectance curve feature between two different angles of incidence at 45° and 70°, one with weaker and stronger absorption, respectively. The difference is marked by distinct peaks at around 400 nm wavelength for the 45° incidence and corresponding valleys for the 70° incidence. We note that the latter angle is in closer proximity to Brewster's angle, especially given our utilization of transverse magnetic (TM) polarization illumination. These peaks are related to the localized surface plasmon resonance peak of a single cobalt nanoparticle. This concludes that cobalt nanoparticle's thin film absorber has potential because the absorber can perform better than copper nanoparticle absorber with stronger absorption, though it has not been experimentally proven.

3.5 Summary

In this chapter, we have employed the multiscale modeling technique to investigate the performance of a nanoparticle-based multilayer broadband absorber. Our motivation for this study stems from prior research indicating the potential of nanoparticle-based solar thermal collectors. Our objective was to study into the optimization of this absorber. To achieve this, we establish a multilayer system consisting of a layer of Au_{144} gold nanoparticles in conjunction with copper and cobalt nanoparticles in a dielectric matrix, a dielectric spacer layer, and a metallic mirror. Our results demonstrate a nearly perfect broad absorption of up to 90% of incident light energy. Further, we made an effort to optimize the copper nanoparticle thin film absorber by considering many properties inside the absorber, like adding nanoparticles with different material other than copper, studying the effect of surface roughness at the surface of the thin film absorber, and subsituting the nanoparticles inside the thin film with ones with sharp tips. Moreover, we compared the computational results obtained from the copper and cobalt nanoparticles absorber with experimental data, showing a noticeable agreement. These findings not only confirm the validity of the computational result but also provide valuable insights for further enhancements in the absorber's performance.

4. Conclusion and outlook

We have studied in this thesis broadband perfect absorbers based on thin film systems with plasmonic nanoparticles. The thin film consists of a layer with many metallic nanoparticles, a dielectric spacer layer, and a metallic mirror as the substrate. We utilize the multiscale modeling methods to study the optical properties of such an absorber. The method starts by considering the optical properties of nanoparticles or a molecule and further utilizes the small-scale optical properties to be applied in a large-scale device, a thin-film absorber in our case.

For instance, the T-matrix of an Au_{144} gold molecule obtained through TD-DFT can be scaled up to be transformed into a T-matrix of a cluster of many identical Au_{144} molecules. Later, we can find the scattering response from a layer built from a periodic arrangement of clusters in two dimensions. Finally, we can find the absorptance from the absorber with a layer of molecules. It turns out that the light can be almost perfectly absorbed in a visible light spectrum ($\lambda = 300 - 800$ nm), approximately 97% of light energy is absorbed by the thin film when we consider a specific thin film thickness, which is a pretty good finding. Further, we take a look at bulk copper nanoparticles inside an alumina matrix as the nanoparticles layer for the next study. By considering various copper nanoparticles cluster filling fraction, we understand that a larger filling fraction of copper nanoparticles is beneficial to absorb more light at longer wavelength, especially in near-infrared regions ($\lambda \approx 1800$ nm). We found that it is possible to have 90% of light energy absorption according to computation. Additionally, a research group led by Prof. Franz Faupel at Kiel University explored the fabrication of the absorbers, had their configurations according to the design predicted by our computations. We compare the results from the fabricated and the simulated samples. It turns out that we have generally very good agreement with both the results in specific filling fractions. Only for excesssively large filling fractions, the agreement between experiment and simulation was not very satisfying. This disagreement was explained by the violation of specific assumptions made in the simulations. Specifically, we observed at high filling fractions for the fabricated nanoparticle layers an aggregation of nanoparticles to form nanoislands within the layer. That aggregation diminishes the plasmonic interaction between the nanoparticles, observed through measurements in the experiment. That interaction of fused nanoparticles is not taken into account in our simuations.

There are many interesting ideas reported by many people to improve our absorber, so that the absorber can strongly absorb electromagnetic waves in a much broader spectrum, expectantly up to the mid-infrared region ($2500 - 25000$ nm). For instance, applying non-spherical nanoparticles to the absorber, several papers have reported near-infrared plasmon resonances [107, 108, 109]. This is a challenge computationally because we have to find the T-matrix of non-spherical nanoparticles. We can use numerical methods to find this T-matrix, but it only works when the nanoparticles are not interacting in the near-field region, due to Rayleigh hypothesis [105]. However, ongoing research in the group of Prof. Carsten Rockstuhl's at the Karlsruhe Institute of Technology explores an algorithm to create a T-matrix for non-spherical nanoparticles expioiting the concept of a topological skeleton. Then, it will be interesting if we can improve the absorption of light at much longer wavelengths than near-infrared regions. For example, applying materials that sustains LSPR at wavelengths in the near-infrared region like indium tin oxide [110], could be one option. Alternatively, we can employ a metasurface on top of our absorber with chiral plasmonic materials [111], vanadium oxide nanorods [112], and adding cermet thin films as the spacer layer [113].

As we venture into solar harvesting applications, it becomes essential for future studies to compare the performance of our absorber with the actual solar radiation spectrum. Evaluating its effectiveness across specific operating temperatures is also essential. Given that we aim to position the absorber in areas with high sunlight intensity, such as areas near the equator and deserts with notably high ambient temperatures, understanding its thermal performance will be important. It is also noteworthy that sunlight emits a decent infrared light. Therefore, to optimize its efficiency, the design of the solar absorber should prioritize the absorption of sunlight primarily at wavelengths with the highest intensity, which peaks in the visible spectrum and gradually decreases at longer wavelengths. This means that it would ensure maximum sunlight energy absorption while minimizing losses, leading to enhanced overall efficiency of the solar harvesting system.

Bibliography

[1] R. P. Feynman, R. B. Leighton, M. Sands, and S. B. Treiman. The feynman lectures on physics. Physics Today, 17(8):45–46, August 1964.

[2] S. Satrusalya and L. Goswami. Review on free space optical communication. Materials Today: Proceedings, 81:231–234, 2023.

[3] A. A. B. Raj, P. Krishnan, U. Darusalam, G. Kaddoum, Z. Ghassemlooy, M. M. Abadi, A. K. Majumdar, and M. Ijaz. A review–unguided optical communications: Developments, technology evolution, and challenges. Electronics, 12(8):1922, April 2023.

[4] D. Ganguly, S. Chakraborty, M. Balitanas, and T. H. Kim. Medical imaging: A review. In Communications in Computer and Information Science, pages 504–516. Springer Berlin Heidelberg, 2010.

[5] S. Wang, G. Cao, Y. Wang, S. Liao, Q. Wang, J. Shi, C. Li, and D. Shen. Review and prospect: Artificial intelligence in advanced medical imaging. Frontiers in Radiology, 1, December 2021.

[6] S. J. Corbitt, M. Francoeur, and B. Raeymaekers. Implementation of optical dielectric metamaterials: A review. Journal of Quantitative Spectroscopy and Radiative Transfer, 158:3–16, June 2015.

[7] Z. Wang, F. Cheng, T. Winsor, and Y. Liu. Optical chiral metamaterials: a review of the fundamentals, fabrication methods and applications. Nanotechnology, 27(41):412001, September 2016.

[8] J Jung, H Park, J Park, T Chang, and J Shin. Broadband metamaterials and metasurfaces: a review from the perspectives of materials and devices. Nanophotonics, 9(10):3165–3196, June 2020.

[9] A. Ali, A. Mitra, and B. Aïssa. Metamaterials and metasurfaces: A review from the perspectives of materials, mechanisms and advanced metadevices. Nanomaterials, 12(6):1027, March 2022.

[10] J. Wu, Z. T. Xie, Y. Sha, H. Y. Fu, and Q. Li. Epsilon-near-zero photonics: infinite potentials. Photonics Research, 9(8):1616, July 2021.

[11] V. Pacheco-Peña, D. M. Solís, and N. Engheta. Time-varying electromagnetic media: opinion. Optical Materials Express, 12(10):3829, September 2022.

[12] P. Garg, A. G. Lamprianidis, D. Beutel, T. Karamanos, B. Verfürth, and C. Rockstuhl. Modeling four-dimensional metamaterials: a t-matrix approach to describe time-varying metasurfaces. Optics Express, 30(25):45832, December 2022.

[13] X. Wang, M. S. Mirmoosa, V. S. Asadchy, C Rockstuhl, S. Fan, and S. A. Tretyakov. Metasurface-based realization of photonic time crystals. Science Advances, 9(14), April 2023.

[14] A. T. Young. Rayleigh scattering. Applied Optics, 20(4):533, February 1981.

[15] B. Zerulla, M. Krstić, D. Beutel, C. Holzer, C. Wöll, C. Rockstuhl, and I. Fernandez-Corbaton. A multi-scale approach for modeling the optical response of molecular materials inside cavities. Advanced Materials, 34(21):Art.Nr. 2200350, 2022. 43.32.02; LK 01.

[16] B. Zerulla, C. Li, D. Beutel, S. Oßwald, C. Holzer, J. Bürck, S. Bräse, C. Wöll, I. Fernandez-Corbaton, L. Heinke, C. Rockstuhl, and M. Krstić. Exploring functional photonic devices made from a chiral metal–organic framework material by a multiscale computational method. Advanced Functional Materials, April 2023.

[17] M. M. Müller, N. Perdana, C. Rockstuhl, and C. Holzer. Modeling and measuring plasmonic excitations in hollow spherical gold nanoparticles. Journal of Chemical Physics, 156(9):Art.–Nr.: 094103, 2022. 43.32.02; LK 01.

[18] V. Sebestyén. Renewable and sustainable energy reviews: Environmental impact networks of renewable energy power plants. Renewable and Sustainable Energy Reviews, 151:111626, November 2021.

[19] S. A. Kalogirou. Solar thermal collectors and applications. Progress in Energy and Combustion Science, 30(3):231–295, 2004.

[20] L. Evangelisti, R. D. L. Vollaro, and F. Asdrubali. Latest advances on solar thermal collectors: A comprehensive review. Renewable and Sustainable Energy Reviews, 114:109318, October 2019.

[21] A. Jamar, Z.A.A. Majid, W.H. Azmi, M. Norhafana, and A.A. Razak. A review of water heating system for solar energy applications. International Communications in Heat and Mass Transfer, 76:178–187, August 2016.

[22] C. Xi, Y. Hongxing, L. Lin, W. Jinggang, and L. Wei. Experimental studies on a ground coupled heat pump with solar thermal collectors for space heating. Energy, 36(8):5292–5300, August 2011.

[23] L. Kumar, M. Hasanuzzaman, and N.A. Rahim. Global advancement of solar thermal energy technologies for industrial process heat and its future prospects: A review. Energy Conversion and Management, 195:885–908, September 2019.

[24] J. A. Duffie and W. A. Beckman. Design of Photovoltaic Systems. John Wiley & Sons, Ltd, 2013.

[25] R.B. Pettit, R.R. Sowell, and I.J. Hall. Black chrome solar selective coatings optimized for high temperature applications. Sol. Energ. Mater., 7(2):153–170, 1982.

[26] B. X. Wang, L. L. Wang, G. Z. Wang, W. Q. Huang, X. F. Li, and X. Zhai. Metamaterial-based low-conductivity alloy perfect absorber. J. Lightwave Technol., 32(12):2293–2298, 2014.

[27] J. Zhou, Z. Liu, G. Liu, P. Pan, X. Liu, C. Tang, Z. Liu, and J. Wang. Ultra-broadband solar absorbers for high-efficiency thermophotovoltaics. Opt. Express, 28(24):36476–36486, Nov 2020.

[28] J. Li, Z. Chen, H. Yang, Z. Yi, X. Chen, W. Yao, T. Duan, P. Wu, G. Li, and Y. Yi. Tunable broadband solar energy absorber based on monolayer transition metal dichalcogenides materials using au nanocubes. Nanomaterials, 10(2):257, 2020.

[29] H. Wang and L. Wang. Perfect selective metamaterial solar absorbers. Opt. Express, 21(S6):A1078–A1093, Nov 2013.

[30] H. Cai, Y. Sun, X. Wang, and S. Zhan. Design of an ultra-broadband near-perfect bilayer grating metamaterial absorber based on genetic algorithm. Opt. Express, 28(10):15347–15359, May 2020.

[31] V. Stelmakh, V. Rinnerbauer, R. D. Geil, P. R. Aimone, J. J. Senkevich, J. D. Joannopoulos, M. Soljačić, and I. Celanovic. High-temperature tantalum tungsten alloy photonic crystals: Stability, optical properties, and fabrication. Appl. Phys. Lett., 103(12):123903, 2013.

[32] M.G. Nielsen, A. Pors, O. Albrektsen, and S.I. Bozhevolnyi. Efficient absorption of visible radiation by gap plasmon resonators. Opt. Express., 20(12):13311–13319, 2012.

[33] R. Piao and D. Zhang. Ultra-broadband perfect absorber based on nanoarray of titanium nitride truncated pyramids for solar energy harvesting. Phys. E: Low-Dimens. Syst. Nanostructures, 134:114829, 2021.

[34] B. Guo, Y. Zhang, J. Hu, J. Li, F. Wu, Q. Peng, and Q. Zhang. Two-dimensional irregular packing problems: A review. Frontiers in Mechanical Engineering, 8, 2022.

[35] J. Mościński, M. Bargieł, Z. A. Rycerz, and P. W. M. Jacobs. The force-biased algorithm for the irregular close packing of equal hard spheres. Molecular Simulation, 3(4):201–212, 1989.

[36] A. Bezrukov, M. Bargieł, and D. Stoyan. Statistical analysis of simulated random packings of spheres. Particle & Particle Systems Characterization, 19(2):111–118, 2002.

[37] J. D. Jackson. Classical electrodynamics. Wiley, New York, NY, 3rd ed. edition, 1999.

[38] A. Taflove and S. C. Hagness. Finite-Difference Time-Domain Solution of Maxwell's Equations, pages 1–33. John Wiley & Sons, Ltd, 2016.

[39] K. D. Paulsen. Finite-element solution of maxwell's equations with helmholtz forms. J. Opt. Soc. Am. A, 11(4):1434–1444, Apr 1994.

[40] U. Hohenester. Nano and Quantum Optics. Springer, Switzerland, 2020.

[41] E. Petryayeva and U. J. Krull. Localized surface plasmon resonance: Nanostructures, bioassays and biosensing—a review. Analytica Chimica Acta, 706(1):8–24, November 2011.

[42] P. Nordlander, C. Oubre, E. Prodan, K. Li, and M. I. Stockman. Plasmon hybridization in nanoparticle dimers. Nano Letters, 4(5):899–903, 2004.

[43] K. M. McPeak, S. V. Jayanti, S. J. P. Kress, S. Meyer, S. Iotti, A. Rossinelli, and D. J. Norris. Plasmonic films can easily be better: Rules and recipes. ACS Photonics, 2(3):326–333, 2015. PMID: 25950012.

[44] T. Okamoto. Near-Field Spectral Analysis of Metallic Beads. Springer Berlin Heidelberg, Berlin, Heidelberg, 2001.

[45] P. B. Johnson and R. W. Christy. Optical constants of the noble metals. Phys. Rev. B, 6:4370–4379, Dec 1972.

[46] D. Paria, C. Zhang, and I. Barman. Towards rational design and optimization of near-field enhancement and spectral tunability of hybrid core-shell plasmonic nanoprobes. Scientific Reports, 9(1), November 2019.

[47] F. Li, J. Shen, C. Guan, Y. Xie, Z. Wang, S. Lin, J. Chen, and J. Zhu. Exploring near-field sensing efficiency of complementary plasmonic metasurfaces for immunodetection of tumor markers. Biosensors and Bioelectronics, 203:114038, 2022.

[48] C. F. Guo, T. Sun, F. Cao, Q. Liu, and Z. Ren. Metallic nanostructures for light trapping in energy-harvesting devices. Light: Science & Applications, 3(4):e161–e161, April 2014.

[49] A. P. Amalathas and M. Alkaisi. Nanostructures for light trapping in thin film solar cells. Micromachines, 10(9):619, September 2019.

[50] B. Bläsi, M. Hanser, K. Jäger, and O. Höhn. Light trapping gratings for solar cells: an analytical period optimization approach. Optics Express, 30(14):24762, June 2022.

[51] C. F. Bohren and D. R. Huffman. Absorption and Scattering of Light by Small Particles. Wiley, April 1998.

[52] G. Mie. Beiträge zur optik trüber medien, speziell kolloidaler metallösungen. Annalen der Physik, 330(3):377–445, 1908.

[53] M. I. Mishchenko, L. D. Travis, and A. A. Lacis. Scattering, Absorption, and Emission of Light by Small Particles. Cambridge University Press, Cambridge, 2002.

[54] C. Narváez-Muñoz, M. R. Hashemi, Ryzhakov. P. B., J. Pons-Prats, and H. Owen. Enriched finite element approach for modeling discontinuous electric field in multi-material problems. Finite Elements in Analysis and Design, 225:104007, November 2023.

[55] Y. L Xu. Electromagnetic scattering by an aggregate of spheres. Applied Optics, 34(21):4573, July 1995.

[56] Y. L Xu. Efficient evaluation of vector translation coefficients in multiparticle light-scattering theories. Journal of Computational Physics, 139(1):137–165, January 1998.

[57] O. R. Cruzan. Translational addition theorems for spherical vector wave functions. Quarterly of Applied Mathematics, 20(1):33–40, 1962.

[58] S. Stein. Addition theorems for spherical wave functions. Quarterly of Applied Mathematics, 19(1):15–24, 1961.

[59] J. F. Marchiando. On calculating the reflectance and transmittance of light for a simple thick grating structure. Journal of Modern Optics, 43(12):2493–2501, December 1996.

[60] P. P. Ewald. Die berechnung optischer und elektrostatischer gitterpotentiale. Annalen der Physik, 369(3):253–287, 1921.

[61] D Beutel, A. Groner, C. Rockstuhl, and I. Fernandez-Corbaton. Efficient simulation of biperiodic, layered structures based on the t-matrix method. Journal of the Optical Society of America B, 38(6):1782, May 2021.

[62] D. Wolf, P. Keblinski, S. R. Phillpot, and J. Eggebrecht. Exact method for the simulation of coulombic systems by spherically truncated, pairwise r-1 summation. The Journal of Chemical Physics, 110(17):8254–8282, May 1999.

[63] S. Stenberg and B. Stenqvist. An exact ewald summation method in theory and practice. The Journal of Physical Chemistry A, 124(19):3943–3946, April 2020.

[64] C. R. Simovski. Material parameters of metamaterials (a review). Optics and Spectroscopy, 107(5):726–753, November 2009.

[65] W. L. Mochan, G. P. Ortiz, and B. S. Mendoza. Efficient homogenization procedure for the calculation of optical properties of 3d nanostructured composites. Optics Express, 18(21):22119, October 2010.

[66] K. Mnasri, A. Khrabustovskyi, C. Stohrer, M. Plum, and C. Rockstuhl. Beyond local effective material properties for metamaterials. Phys. Rev. B, 97:075439, Feb 2018.

[67] B. Zerulla, R. Venkitakrishnan, D. Beutel, M. Krstić, C. Holzer, C. Rockstuhl, and I. Fernandez-Corbaton. A t-matrix based approach to homogenize artificial materials. Advanced Optical Materials, 11(3):Art.–Nr.: 2201564, 2022. 43.32.02; LK 01.

[68] N. Stefanou, V. Yannopapas, and A. Modinos. Heterostructures of photonic crystals: frequency bands and transmission coefficients. Computer Physics Communications, 113(1):49–77, September 1998.

[69] E. Cobanera, A. Alase, G. Ortiz, and L. Viola. Generalization of bloch's theorem for arbitrary boundary conditions: Interfaces and topological surface band structure. Physical Review B, 98(24), December 2018.

[70] C. Menzel, C. Rockstuhl, T. Paul, F. Lederer, and T. Pertsch. Retrieving effective parameters for metamaterials at oblique incidence. Phys. Rev. B, 77:195328, May 2008.

[71] C. Menzel, T. Paul, C. Rockstuhl, T. Pertsch, S. Tretyakov, and F. Lederer. Validity of effective material parameters for optical fishnet metamaterials. Phys. Rev. B, 81:035320, Jan 2010.

[72] T. G. Mackay and A. Lakhtakia. The Transfer-Matrix Method in Electromagnetics and Optics. Morgan & Claypool Publishers, 2020.

[73] N. Perdana, C. Holzer, and C. Rockstuhl. Multiscale modeling of broadband perfect absorbers based on gold metallic molecules. ACS Omega, 7(23):19337–19346, 2022. 43.32.02; LK 01.

[74] N. Perdana, J. Drewes, F. Pohl, A. Vahl, T. Strunskus, M. Elbahri, C. Rockstuhl, and F. Faupel. A thin-film broadband perfect absorber based on plasmonic copper nanoparticles. Micro and Nano Engineering, 16:Art.–Nr.: 100154, 2022. 43.32.02; LK 01.

[75] J. Drewes, N. Perdana, K. Rogall, T. Hartig, M. Elis, U. Schürmann, F. Pohl, M. Abdelaziz, T. Strunskus, L. Kienle, M. Elbahri, F. Faupel, C. Rockstuhl, and A. Vahl. Co-sputtering of a thin film broadband absorber based on self-organized plasmonic cu nanoparticles. Particle & Particle Systems Characterization, September 2023.

[76] B. Brady, V. Steenhof, B. Nickel, A. M. Blackburn, M. Vehse, and A. G. Brolo. Plasmonic light-trapping concept for nanoabsorber photovoltaics. ACS Applied Energy Materials, 2(3):2255–2262, February 2019.

[77] S. Morawiec and I. Crupi. Light trapping by plasmonic nanoparticles. In Solar Cells and Light Management, pages 277–313. Elsevier, 2020.

[78] Y. Gutiérrez, D. Ortiz, J. Saiz, F. González, H. Everitt, and F. Moreno. The UV plasmonic behavior of distorted rhodium nanocubes. Nanomaterials, 7(12):425, December 2017.

[79] N. Fukuoka and K. Tanabe. Lightning-rod effect of plasmonic field enhancement on hydrogen-absorbing transition metals. Nanomaterials, 9(9):1235, August 2019.

[80] M. A. Kats, D. Sharma, J. Lin, P. Genevet, R. Blanchard, Z. Yang, M. M. Qazilbash, D. N. Basov, S. Ramanathan, and F. Capasso. Ultra-thin perfect absorber employing a tunable phase change material. Applied Physics Letters, 101(22), November 2012.

[81] F. Furche. On the density matrix based approach to time-dependent density functional response theory. The Journal of Chemical Physics, 114(14):5982–5992, April 2001.

[82] M. Kehry, Y. J. Franzke, C. Holzer, and W. Klopper. Quasirelativistic two-component core excitations and polarisabilities from a damped-response formulation of the bethe–salpeter equation. Molecular Physics, 118(21-22):e1755064, May 2020.

[83] I. Fernandez-Corbaton, D. Beutel, C. Rockstuhl, A. Pausch, and W. Klopper. Computation of electromagnetic properties of molecular ensembles. ChemPhysChem, 21(9):878–887, April 2020.

[84] M. K. Hedayati, M. Javaherirahim, B. Mozooni, R. Abdelaziz, A. Tavassolizadeh, V. S. K. Chakravadhanula, V. Zaporojtchenko, T. Strunkus, F. Faupel, and M. Elbahri. Design of a perfect black absorber at visible frequencies using plasmonic metamaterials. Advanced Materials, 23(45):5410–5414, October 2011.

[85] M. Hedayati, F. Faupel, and M. Elbahri. Review of plasmonic nanocomposite metamaterial absorber. Materials, 7(2):1221–1248, February 2014.

[86] M. K. Hedayati, A. U. Zillohu, T. Strunskus, F. Faupel, and M. Elbahri. Plasmonic tunable metamaterial absorber as ultraviolet protection film. Applied Physics Letters, 104(4), January 2014.

[87] I. Fabijanić, V. Janicki, J. Ferré-Borrull, M. Bubaš, V. Blažek Bregović, L. F. Marsal, and J. Sancho-Parramon. Plasmonic nanoparticles and island films for solar energy harvesting: A comparative study of cu, al, ag and au performance. Coatings, 9(6):382, 2019.

[88] P. Colomban. The use of metal nanoparticles to produce yellow, red and iridescent colour, from bronze age to present times in lustre pottery and glass: Solid state chemistry, spectroscopy and nanostructure. Journal of Nano Research, 8:109–132, September 2009.

[89] J. Aromaa, M. Kekkonen, M. Mousapour, A. Jokilaakso, and M. Lundström. The oxidation of copper in air at temperatures up to 100 °c. Corrosion and Materials Degradation, 2(4):625–640, October 2021.

[90] M. Scardamaglia, V. Boix, G. D'Acunto, C. Struzzi, N. Reckinger, X. Chen, A. Shivayogimath, T. Booth, and J. Knudsen. Comparative study of copper oxidation protection with graphene and hexagonal boron nitride. Carbon, 171:610–617, January 2021.

[91] P. Banerjee, S. Sengupta, M. Murmu, and N. C. Murmu. Copper oxide as a corrosion inhibitor. In Inorganic Anticorrosive Materials, pages 211–229. Elsevier, 2022.

[92] A. Vahl, J. Strobel, W. Reichstein, O. Polonskyi, T. Strunskus, L Kienle, and F. Faupel. Single target sputter deposition of alloy nanoparticles with adjustable composition via a gas aggregation cluster source. Nanotechnology, 28(17):175703, April 2017.

[93] R. Boidin, T. Halenkovič, V. Nazabal, L. Beneš, and P. Němec. Pulsed laser deposited alumina thin films. Ceramics International, 42(1):1177–1182, January 2016.

[94] C.A. Gueymard, D. Myers, and K. Emery. Proposed reference irradiance spectra for solar energy systems testing. Solar Energy, 73(6):443–467, December 2002.

[95] E. Bellos and C. Tzivanidis. A realistic approach of the maximum work extraction from solar thermal collectors. Applied System Innovation, 1(1):6, January 2018.

[96] E. Bellos. Progress in beam-down solar concentrating systems. Progress in Energy and Combustion Science, 97:101085, July 2023.

[97] J. J. Wu. Simulation of rough surfaces with FFT. Tribology International, 33(1):47–58, January 2000.

[98] J.U. Andersen, E. Bonderup, and K. Hansen. Thermionic emission from clusters. J. Phys. B: At. Mol. Opt. Phys., 35(5):R1–R30, 2002.

[99] W. S. M. Werner, K. Glantschnig, and C. Ambrosch-Draxl. Optical constants and inelastic electron-scattering data for 17 elemental metals. Journal of Physical and Chemical Reference Data, 38(4):1013–1092, December 2009.

[100] J. Su, J. Zhang, Y. Liu, M. Jiang, and L. Zhou. Parameter-dependent oxidation of physically sputtered cu and the related fabrication of cu-based semiconductor films with metallic resistivity. Science China Materials, 59(2):144–150, February 2016.

[101] D. Tahir and S. Tougaard. Electronic and optical properties of cu, cuo, and cu_20 studied by electron spectroscopy. Journal of Physics: Condensed Matter, 24(17):175002, April 2012.

[102] H. Liang, H. Ren, Y. Guo, and Y. Fang. Shape-engineered silver nanocones for refractive index plasmonic nanosensors. Optics Letters, 44(15):3713, July 2019.

[103] N. Perdana, A. A. Iskandar, and M. O. Tjia. Size and shape effects on the field enhancement induced at a silver triangular tip. Journal of Physics: Conference Series, 1057:012008, July 2018.

[104] T. Rother and S. C. Hawkins. Notes on rayleigh's hypothesis and the extended boundary condition method. The Journal of the Acoustical Society of America, 149(4):2179–2188, April 2021.

[105] A. G. Lamprianidis, C. Rockstuhl, and I. Fernandez-Corbaton. Transcending the rayleigh hypothesis with multipolar sources distributed across the topological skeleton of a scatterer. Journal of Quantitative Spectroscopy and Radiative Transfer, 296:108455, February 2023.

[106] H. Wang, L. Xiang, W. Wei, J. An, J He, C Gong, and Y. Hou. Efficient and lightweight electromagnetic wave absorber derived from metal organic framework-encapsulated cobalt nanoparticles. ACS Applied Materials & Interfaces, 9(48):42102–42110, November 2017.

[107] F. Qin, T. Zhao, R. Jiang, N. Jiang, Q. Ruan, J. Wang, L. Sun, C. Yan, and H. Lin. Thickness control produces gold nanoplates with their plasmon in the visible and near-infrared regions. Adv. Opt. Mater., 4(1):76–85, 2016.

[108] N. K. Pathak, P. Parthasarathi, P. S. Kumar, and R. P. Sharma. Tuning of the surface plasmon resonance of aluminum nanoshell near-infrared regimes. Physical Chemistry Chemical Physics, 21(18):9441–9449, 2019.

[109] H. Jiang and J. Sabarinathan. Near infrared surface plasmon resonance of gold nanoring based plasmonic crystals for sensor applications. In 2009 9th IEEE Conference on Nanotechnology (IEEE-NANO), pages 777–780, 2009.

[110] M. Kanehara, H. Koike, T. Yoshinaga, and T. Teranishi. Indium tin oxide nanoparticles with compositionally tunable surface plasmon resonance frequencies in the near-ir region. J. Am. Chem. Soc., 131(49):17736–7, nov 2009.

[111] M. S. Mahmud, D. Rosenmann, D. A. Czaplewski, J. Gao, and X. Yang. Chiral plasmonic metasurface absorbers in the mid-infrared wavelength range. Optics Letters, 45(19):5372, September 2020.

[112] Y. Lian, Y. Li, Y. Lou, Z. Liu, C. Jiang, Z. Hu, and J. Wang. Adjustable trifunctional mid-infrared metamaterial absorber based on phase transition material VO2. Nanomaterials, 13(12):1829, June 2023.

[113] F. Yang, R. Li, S. Tan, J. Dong, and S. Jiang. Visible-mid infrared ultra-broadband and wide-angle metamaterial perfect absorber based on cermet films with nano-cone structure. Nanophotonics, 12(13):2451–2460, March 2023.

Acknowledgement

First of all, I would have my biggest thank my supervisor Prof. Carsten Rockstuhl for giving me the opportunity to do my PhD on a topic that is very interesting to me. He gave me everything related to my PhD study, from very basic optical physics to things that I could not understand, but were very interesting. He also guided me on how a proper scientist should act. But most importantly, it was his mental encouragement and kindness to me that was invaluable in completing this PhD.

Next, I would like to give a special acknowledgement to my colleagues in Prof. Franz Faupel's research group at the University of Kiel in helping me to provide everything related to the experiments to support the simulation results in this thesis. I had a very good time working with you all during our collaboration.

Then, to all my colleagues in Prof. Carsten Rockstuhl's research group. I would like to thank you for working together and sharing your experiences. I was really lucky to be in this group, I felt a deep sense of kinship. I wish you all the best for the future to all of you!

Last and not least, to my beloved parents. They have always supported me in happy times as well as in dark times during my PhD studies.

Selbstsätndigkeitserklärung

Eidesstattliche Versicherung gemäß §13 Absatz 2 Ziffer 3 der Promotionsordnung des Karlsruher Instituts für Technologie (KIT) für die KIT-Fakultät für Physik:

1. Bei der eingereichten Dissertation zu dem Thema Broadband Thin Film Absorber Based on Plasmonic Nanoparticles handelt es sich um meine eigenständig erbrachte Leistung.
2. Ich habe nur die angegebenen Quellen und Hilfsmittel benutzt und mich keiner unzulässigen Hilfe Dritter bedient. Insbesondere habe ich wörtlich oder sinngemäß ausanderen Werken übernommene Inhalte als solche kenntlich gemacht.
3. Die Arbeit oder Teile davon habe ich wie folgt/ bislang nicht[1] an einer Hochschule des In-oder Auslands als Bestandteil einer Prüfungs- oder Qualifikationsleistung vorgelegt.
   Titel der Arbeit: Broadband Thin Film Absorber Based on Plasmonic Nanoparticles
   Hochschule und Jahr: KIT-Fakultät für Physik 2023
   Art der Prüfungs- oder Qualifikationsleistung: Dissertation
4. Die Richtigkeit der vorstehenden Erklärungen bestätige ich.
5. Die Bedeutung der eidesstattlichen Versicherung und die strafrechtlichen Folgeneiner unrichtigen oder unvollständigen eidesstattlichen Versicherung sind mir bekannt.

Ich versichere an Eides statt, dass ich nach bestem Wissen die reine Wahrheit erklärt und nichts verschwiegen habe.

Ort und Datum

Unterschrift

---

[1] Nicht Zutreffendes streichen. Bei Bejahung sind anzugeben: der Titel der andernorts vorgelegten Arbeit, die Hochschule, das Jahr der Vorlage und die Art der Prüfungs- oder Qualifikationsleistung.